

# SUPPORTING INFORMATION

## Elucidating the effects of LiF on lithium metal anodes

Mun Sek Kim,<sup>1,2,3,#</sup> Jingyang Wang,<sup>1,4,5,#</sup> Wenbo Zhang,<sup>1,#</sup> Philaphon Sayavong,<sup>6</sup> Zewen Zhang,<sup>1</sup> Solomon T. Oyakhire,<sup>2</sup> Sanzeeda Baig Shuchi,<sup>2</sup> Sang Cheol Kim,<sup>1</sup> Yi Cui,<sup>1</sup> Yuelang Chen,<sup>2,6</sup> Zhiao Yu,<sup>2,6</sup> Huaxin Gong,<sup>2</sup> Rong Xu,<sup>1</sup> Junyoung Lee,<sup>1</sup> Il Rok Choi<sup>1,2</sup>, Jun Ho Lee,<sup>1</sup> Kristin A. Persson,<sup>7,8</sup> Jian Qin,<sup>2</sup> Zhenan Bao<sup>2,\*</sup> and Yi Cui<sup>1,9,10,\*</sup>

<sup>1</sup>Department of Materials Science and Engineering, Stanford University, Stanford, CA 94305, USA.

<sup>2</sup>Department of Chemical Engineering, Stanford University, Stanford, CA 94305, USA.

<sup>3</sup>School of Mechanical and Aerospace Engineering, Nanyang Technological University, Singapore 639798, Singapore.

<sup>4</sup>Materials Sciences Division, Lawrence Berkeley Laboratory, Berkeley, CA 94720, USA.

<sup>5</sup>Key Laboratory of Theoretical & Computational Photochemistry of Ministry of Education, College of Chemistry, Beijing Normal University, Beijing 100875, China.

<sup>6</sup>Department of Chemistry, Stanford University, Stanford, CA 94305, USA.

<sup>7</sup>Department of Materials Science and Engineering, University of California, Berkeley, CA 94720, USA

<sup>8</sup>Energy Technologies Area, Lawrence Berkeley Laboratory, Berkeley, CA 94720, USA.

<sup>9</sup>Stanford Institute for Materials and Energy Sciences, SLAC National Accelerator Laboratory, Menlo Park, CA 94025, USA.

<sup>10</sup>Department of Energy Science and Engineering, Stanford University, Stanford, CA 94305, USA

#These authors contributed equally: Mun Sek Kim, Jingyang Wang, and Wenbo Zhang.

\*e-mail: Yi Cui (corresponding author) [yicui@stanford.edu](mailto:yicui@stanford.edu) and Zhenan Bao [zbao@stanford.edu](mailto:zbao@stanford.edu)

# EXPERIMENTAL SECTION

## Materials

The coin cell assembly and electrolyte preparations were conducted in an Ar gas-filled glovebox with an O<sub>2</sub> concentration below 0.2 ppm and H<sub>2</sub>O concentration under 0.01 ppm. All the materials were stored inside of the glovebox. 1 M LiPF<sub>6</sub> in EC:DEC (1:1 v/v) was purchased from Sigma Aldrich. The reference electrolyte (RE) was prepared by mixing 1 M LiPF<sub>6</sub> in EC:DEC (1:1 v/v) with 10 vol% FEC (Sigma-Aldrich). LiF and Li<sub>2</sub>O suspensions were purchased from Nanoshel. LiF SE was prepared by suspending 15 wt% (indicated otherwise) of LiF in RE. All the electrolytes were freshly prepared right before fabricating coin cells. To make 2032-type coin cells (one 1 mm spacer and spring), high-purity Li foil (500 μm, 99.9% from Alfa Aesar, 11 mm in diameter), Cu foil from Pred Materials, an 11 μm polyethylene separator from W-Scope, and LiNi<sub>0.8</sub>Mn<sub>0.1</sub>Co<sub>0.1</sub> (NMC811) from Targray were used.

## Cryo-TEM

Lacey-carbon Cu TEM grids (3 mm in diameter) served as the working electrode for Li<sup>0</sup> electrodeposition in Li<sup>0</sup>|lacey-carbon Cu TEM grid cells. Li<sup>0</sup> was electrodeposited galvanostatically in amounts of 0.1 mAh cm<sup>-2</sup> at 1 mA cm<sup>-2</sup> or cycled ten times under 1 mAh cm<sup>-2</sup> and 1 mA cm<sup>-2</sup>. Please note that the capacity of 0.1 mAh cm<sup>-2</sup> was used to obtain beam-transparent Li<sup>0</sup> electrodeposits on the lacey-carbon Cu TEM grid. Post-electrodeposition, the coin cells were taken apart within an Ar-filled glovebox. These electrodeposited TEM grids were then cleaned with 30 μL of DEC and dried before a rapid freezing process using liquid nitrogen. Immediately after, the sample was quickly submerged in liquid nitrogen, ensuring minimal exposure to the ambient environment before cryogenic treatment. For cryo-TEM analysis, the sample, still submerged in liquid nitrogen, was placed into the Gatan side-entry cryo-transfer holder (model 626) and introduced into the TEM column. This holder features a unique cryo-shutter to eliminate the risks of air exposure and ice formation on the sample. Within the TEM column, temperatures were consistently held at roughly -178 °C. The cryo-TEM studies employed ThermoFisher Titan 80-300 environmental scanning transmission electron microscope, with an accelerating voltage of 300 kV. This microscope was outfitted with an image-forming lens aberration corrector, aligned before each analysis. Captured cryo-TEM images used Gatan one-view. These images were recorded at an electron dose rate of about 300 e<sup>-</sup> Å<sup>-2</sup> s<sup>-1</sup>, capturing a sequence of 5 frames at 0.1 s per frame for every image. All FFT indexing measurements were divided by the correction factor of 0.91 to compensate for a calibration offset.

## Cryo-STEM

Cryo-STEM studies were performed using a ThermoFisher Titan 80-300 environmental scanning transmission electron microscope, set to an accelerating voltage of 300 kV. The microscope was enhanced with an aberration corrector for the image-forming lens, which was adjusted prior to each sample evaluation.

### **Cryo-STEM EELS**

Characterization using cryo-STEM EELS was conducted with the following parameters: a C2 aperture size of 50 mm, probe current set at 75 pA, camera length at 48 mm, and a pixel dwell duration of 100 ms. The STEM EELS spectra were captured using the high-resolution Gatan imaging filter (GIF Quantum 966) in Dual EELS mode, with a dispersion set at 0.25 eV/channel. For mapping, a two-window approach was employed; the pre-edge window was adjusted to a power-law background while the post-edge window covered the 20-40 eV range on the core-loss signal.

### **SEM and EDXS**

Before performing microscopy, electrodeposited Li<sup>0</sup> on Cu (approximately 11 mm in diameter) with RE and LiF SE from Li<sup>0</sup>|Cu cells (Plating capacity and current density of 1 mAh cm<sup>-2</sup> and 1 mA cm<sup>-2</sup>) were washed with 60 μL of pure DEC solvent inside the glovebox. The sealed samples were transferred to Scanning Electron Microscopy (SEM) chamber for analysis. The SEM was conducted using an Apreo S LoVac from Thermo Fisher Scientific. Images were captured at a voltage of 5 kV and a beam current of 50 pA, with the electron signal being collected through the Everhart-Thornley Detector. The same conditions were used to take images of LiF and Li<sub>2</sub>O suspensions, which were placed onto double-sided carbon tape (Oxford Instruments). For the energy dispersive X-ray spectroscopy (EDXS), data were gathered using a Bunker XFlash 6-60 detector, operating at 10 kV and a beam current of 800 pA.

### **XRD**

The crystallographic structures of LiF were analyzed using X-ray diffraction (XRD) on a PANalytical Empyrean equipped with a Cu(Kα) X-ray source. The LiF suspensions were positioned on a glass slide and sealed with Kapton tape (Amazon). Subsequently, diffraction patterns were recorded ranging from 10° to 70°, with a step increment of 0.01.

### **XPS**

XPS scans were carried out using PHI Versaprobe I, III, and IV equipped with a monochromatized Al Kα X-ray source. Throughout the measurements, the XPS chamber maintained a pressure of approximately 10<sup>-7</sup> Pa. Li<sup>0</sup>|Li<sup>0</sup> and Li<sup>0</sup>|Cu cells (cycling condition was ten complete cycles of Li<sup>0</sup> plating and stripping at 1 mAh cm<sup>-2</sup> and 1 mA cm<sup>-2</sup>) with RE and LiF SE were cleaned with 60 μL of DEC inside an Ar-filled glovebox to wash away the residual salts. To avoid exposure to air, a vacuum transfer vessel was employed to move the samples directly from the glovebox to the instrument's vacuum transfer chamber. The high-resolution spectra were then adjusted using the C 1s peak set at 284.6 eV. The XPS scans were analyzed using MultiPak software.

### **Zeta potential**

Zeta potential measurements were performed on a Brookhaven Nanobrook Omni instrument at Stanford Nano Shared Facilities with the phase analysis light scattering (PALS) mode. A tightly sealed glass cuvette containing 15 wt% LiF in EC:DEC (1:1 v/v) was sonicated for 2 minutes and placed to the instrument. Then, five measurements were made to obtain the average zeta potential of LiF. The conductance of specified solvent systems was measured *via* Brookhaven Nanobrook Omni instrument.

## DFT simulations

Density functional theory (DFT) calculations were conducted with the GPAW package<sup>1,2</sup>. The electronic exchange-correlation effects were described using the Perdew-Burke-Ernzerhof (PBE) functional under the generalized gradient approximation (GGA)<sup>3</sup>. The electronic wave function was expanded in the plane-wave basis set using the projector augmented wave (PAW) method<sup>4,5</sup>. For all the slab models used in this work, the vacuum was chosen to be greater than 1.4 nm in order to minimize artificial electrostatic interaction due to periodic boundary conditions. The energy cutoff was set to be 500 eV; the k-point grid was set to be Gamma point,  $7 \times 7 \times 7$ ,  $2 \times 2 \times 1$  and  $3 \times 3 \times 1$  for the molecules, bulk, surface slabs, and grain boundary slabs, respectively. The stoichiometries of the slabs have been checked to be consistent with the chemical formula; specifically, the net charge is neutral for all the systems simulated. For all the DFT calculations of surface slabs with adsorbates and asymmetric interface slabs, the artificial dipole is eliminated *via* a dipole correction<sup>6</sup>. The energies have been converged to below 0.02 eV/atom with respect to energy cutoff, cell size, vacuum thickness, and slab thickness. The surface adsorption energies were calculated *via* structural optimization, while the activation energies were calculated *via* the nudged elastic band (NEB) method<sup>7,8</sup>. The force convergence criterion is 0.01 eV Å<sup>-1</sup> for geometry optimization, and 0.05 eV Å<sup>-1</sup> for NEB calculations. For each slab, the slab center was placed at the center of the supercell before adding the adsorbate. During structure optimization and NEB calculations of surface slabs, the atoms in the lower half of the slab were constrained to be fixed in position. During structure optimization and NEB calculations of grain boundary slabs, rigid-body constraints were imposed on the outermost two layers of both ends of the slab. The surface energies were calculated with the following expression:  $E_{\text{surf}} = (E_{\text{slab}} - m \cdot E_{\text{bulk}}) / 2A$ , where  $E_{\text{slab}}$  and  $E_{\text{bulk}}$  denote the total energy of the slab supercell and the bulk unit cell respectively,  $m$  denotes the number of copies of bulk unit cell in the slab supercell, and  $A$  denotes the cross-sectional surface area of the slab. The binding energies were calculated with the following expression:  $E_{\text{bind}} = E_{\text{tot}} - E_{\text{slab}} - E_{\text{adsorbate}}$ , where  $E_{\text{tot}}$ ,  $E_{\text{slab}}$  and  $E_{\text{adsorbate}}$  represent the total energy of the surface slab plus adsorbate system, the energy of the surface slab supercell, and the energy of the adsorbate, respectively. The surface energies and adsorption energies were checked to have reached convergence below a threshold of 0.05 eV/Å<sup>2</sup> and 0.05 eV, respectively, with respect to slab thickness, vacuum size, and k-point density. The LiF / Li<sub>2</sub>O grain boundary was constructed by interfacing LiF (200) and Li<sub>2</sub>O (111) slabs. The LiF / LiF (210) Σ3 grain boundary was constructed by interface two LiF (210) slabs in the opposite z-directions. The grain boundary models were subsequently relaxed to their optimal structures.

## MD simulations

Molecular Dynamics simulations of the suspension electrolyte systems were conducted with the Large-scale Atomic/Molecular Massively Parallel Simulator (LAMMPS) package<sup>9</sup>. The intramolecular interatomic interactions were modeled using the OPLS-AA force field<sup>10</sup>, with the fitting parameters for EC, DEC, FEC,  $\text{PF}_6^-$  and  $\text{Li}^+$  taken from previous work<sup>11</sup>. Long-range potential (Lennard-Jones, Coulomb) used a real-space cutoff of 1.2 nm, while the reciprocal-space part of the Coulomb potential was calculated using the smooth particle-mesh Ewald method<sup>12</sup>. All the systems simulated in this work contain 610 EC molecules, 456 DEC molecules, 164 FEC molecules, and 120  $\text{LiPF}_6$  molecules. The interface models contain a LiF slab of various orientations and surface structures as described in the main text. The equilibrated slab thicknesses for the (200), (220)-Octo, and (111)-Octo were approximately 1.3 nm, 1.6 nm, and 1.6 nm, respectively; such thicknesses reduce artificial interactions of electrolytes on the opposite sides of the slabs. The partial charges of Li and F atoms in the LiF slabs were set to 0.7 and  $-0.7$ , respectively, to account for charge screening effects in the solution environment. The structures were initialized randomly using the Packmol package<sup>13</sup>. The simulation protocol for the bulk system consists of energy minimization, a 1 ns equilibration at  $T = 350$  K in the canonical (NVT) ensemble, a 1 ns equilibration at 350 K in the isothermal-isobaric (NPT) ensemble, a 2 ns quenching from 350 K to 300 K in the NPT ensemble, a 3 ns equilibration at 350 K in the NPT ensemble, and a production run of 20 ns in the NVT ensemble. The simulation protocol for the interface systems consists of 5 ns of equilibration under the temperature  $T = 300$  K in the isothermal-isobaric (NPT) ensemble, followed by a 30 ns production run at  $T = 300$  K in the canonical (NVT) ensemble during which the slab atoms are fixed in position. The NPT runs are conducted at a pressure of 1 atm, with a degree of freedom only along the z-direction. A Nose-Hoover thermostat and barostat are used to regulate the temperature and pressure, respectively, with the corresponding damping time  $\tau = 0.2$  ps and 1 ps. The time step is chosen to be 1 fs. Data analysis is carried out using the final 10 ns (20 ns) production-run simulation for bulk (interface) systems. Average coordination analysis is carried out with the MDAnalysis code<sup>14</sup>. In molecular dynamics simulations, as the surface slabs do not have dipole moments either naturally (for LiF (200)) or due to surface reconstructions (for LiF (220)-Octo and LiF (111)-Octo), imposing dipole correction was unnecessary. Structure visualization was carried out with Ovito<sup>15</sup>.

## QCM measurements

QCM measurements of LiF in RE and LiF SE were performed using a QCM200 instrument (Stanford Research Systems). LiF suspension particles adhered to the organic solvent-proof adhesive (3M) that was placed onto the QCM sensor. Considering the possibility of LiF particle detachment, we gently blew dry air over the LiF-attached QCM sample holder to remove loosely attached LiF particulates prior to the measurement, ensuring that only firmly adhered LiF remained. The sensor of AT-cut quartz crystal coated with copper (Phillip Technologies) was used. Once the QCM sensor was calibrated and stabilized, the mass change measurements were recorded after injecting RE and LiF SE.

### **Electrolyte solvation energy**

The electrolyte solvation energies of RE and LiF SE were measured by using a Biologic VMP3 and an H-cell. This cell comprised a control electrolyte (1M lithium bis(fluorosulfonyl)imide (LiFSI) in DEC), a salt bridge (1M LiFSI in dimethoxyethane/dioxolane 1:1 v/v), and test electrolytes (RE and 30 wt% LiF SE) with Li metal immersed in both the control and test electrolytes. The electrolyte solvation energies of RE and LiF SE were measured for 3 seconds to determine average values. Details on the apparatus setup are available in the provided reference<sup>16</sup>.

### **<sup>7</sup>Li NMR**

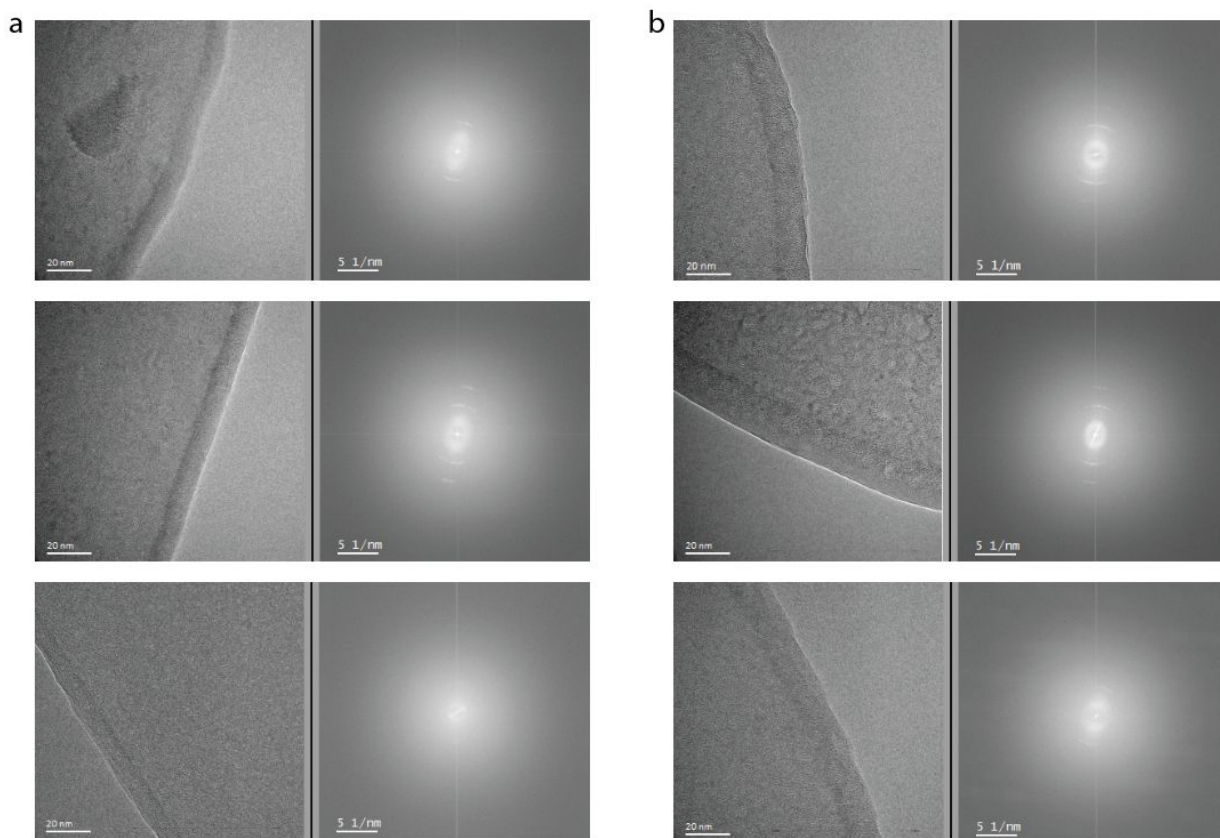
For 1D <sup>7</sup>Li NMR experiments, an NMR tube featuring a coaxial insert was used. The external tube was filled with freshly made RE and (1~20 wt%) LiF SE, while the inner tube held deuterated solutions serving as external references. The <sup>7</sup>Li NMR measurements were conducted on a Varian Inova 500 MHz NMR spectrometer, and chemical shifts were aligned with 1 M LiCl in D<sub>2</sub>O at 0 ppm.

### **Electrochemical measurements.**

For electrochemical tests, Li<sup>0</sup>|Li<sup>0</sup>, Li<sup>0</sup>|Cu, and Cu|LiNi<sub>0.8</sub>Mn<sub>0.1</sub>Co<sub>0.1</sub> cells with 30 μL of specified electrolytes were used. Using Biologics VMP3, electrochemical impedance spectroscopy measurements were taken over a frequency range from 7 MHz to 100 mHz to evaluate the interfacial impedances of Li<sup>0</sup>|Li<sup>0</sup> and Li<sup>0</sup>|Cu cells (three identical cell types for each condition) with RE and LiF SE. Measurements for Li<sup>0</sup>|Cu and Cu|Li<sub>1</sub>Ni<sub>0.8</sub>Co<sub>0.1</sub>Mn<sub>0.1</sub> cells were carried out using Arbin and Land devices. For the CE and nucleation overpotential measurements from Li<sup>0</sup>|Cu cells with RE and LiF SE, the current density of 1 mA cm<sup>-2</sup> was used with a cut-off voltage of 1 V vs. Li<sup>+</sup>/Li to cycle. For the CE measurement, one activation cycle was done by plating and stripping 5 mAh cm<sup>-2</sup> amount of Li<sup>0</sup>. After the activation cycle, 5 mAh cm<sup>-2</sup> Li<sup>0</sup> was deposited onto Cu, then nine cycles of 1 mAh cm<sup>-2</sup> Li<sup>0</sup> were stripped and plated. In the last step, the remaining Li<sup>0</sup> was fully stripped to calculate CE<sup>17</sup>. The nucleation overpotential was calculated by subtracting the mass transfer-controlled potential from the tip potential in the first Li<sup>0</sup> plating step of the activation cycle<sup>11,18-20</sup>. Three identical Li<sup>0</sup>|Cu cells were measured with each of RE and LiF SE to obtain average CE and Li nucleation overpotential. For the Cu|NMC811 cells with RE and LiF SE, charging and discharging current densities of 0.4 mA cm<sup>-2</sup> and 0.8 mA cm<sup>-2</sup> were used to cycle the cells between 3 V to 4.2 V vs. Li<sup>+</sup>/Li, and constant voltage charging was applied at 4.3 V vs. Li<sup>+</sup>/Li with a cut-off current value of 0.04 mA cm<sup>-2</sup>. Under these specified conditions, the areal capacity of the NMC811 cathode was about 4.5 mAh cm<sup>-2</sup>.

# SUPPORTING NOTES

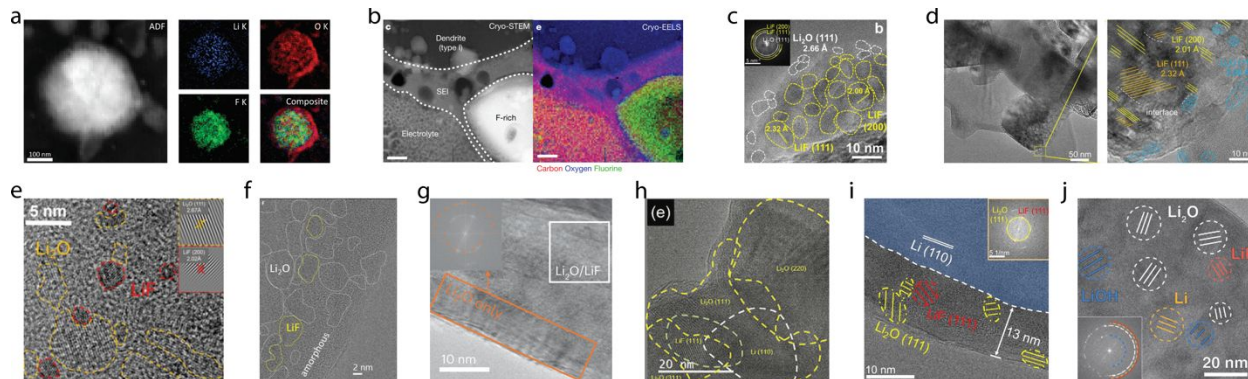
## Note S1 | Lack of LiF presence within compact-SEI



**Note S1 Figure 1.** (a) Cryo-HRTEM image of the compact-SEI on electrodeposited Li<sup>0</sup> (left) and corresponding FFT (right) with RE. (b) Cryo-HRTEM image of the compact-SEI on electrodeposited Li<sup>0</sup> (left) and corresponding FFT (right) with LiF SE. All the FFT images show Li<sub>2</sub>O {111} or/and {220} diffraction patterns.

Although we have shown the representative cryo-HRTEM and corresponding FFT images for RE and LiF SE in **Figure 1b-e**, we note that multiple samples and imaging locations were carefully analyzed to ensure that the absence of LiF diffraction is not due to detection-limit artifacts (**Note S1 Figure 1**). Across all datasets we examined, only Li<sub>2</sub>O reflections were consistently observed, while LiF diffraction remained undetected within the compact-SEI. Importantly, this observation is not unique to our work. Several prior cryo-TEM studies have reported a similar absence of LiF within the compact-SEIs on Li<sup>0</sup> anodes<sup>21-29</sup>. In our earlier work<sup>24</sup>, atomic-resolution cryo-TEM imaging of SEIs formed with 1 M LiPF<sub>6</sub> in EC:DEC (1:1 v/v) and with 10 vol% FEC (RE) showed no detectable LiF lattice, which pointed to raising questions about the role and spatial arrangement of LiF. To further probe this, a prior cryo-STEM EELS study chemically mapped LiF distributions across SEIs derived from various electrolytes<sup>22,23</sup>, in which the major claim was made that LiF was not distributed within the compact-SEI but was instead sporadically arranged as the indirect-SEI<sup>22</sup>, which is in line with other studies<sup>23,26-28,30</sup>.

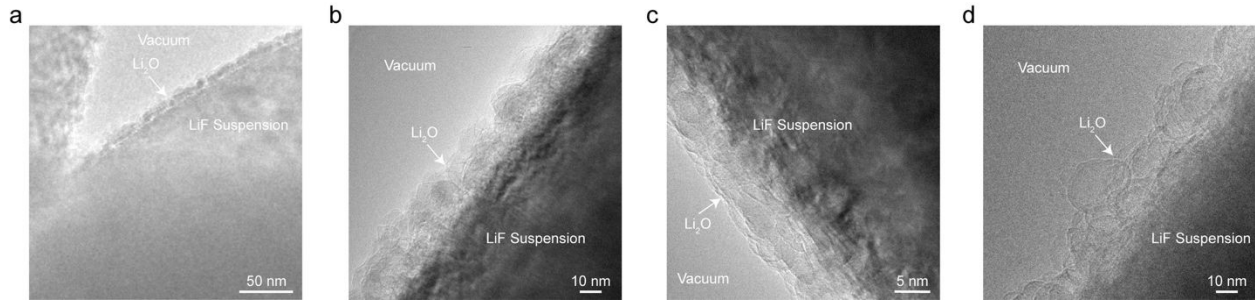
## Note S2 | Li<sub>2</sub>O passivated LiF and coexistence of LiF/Li<sub>2</sub>O in lithium SEIs



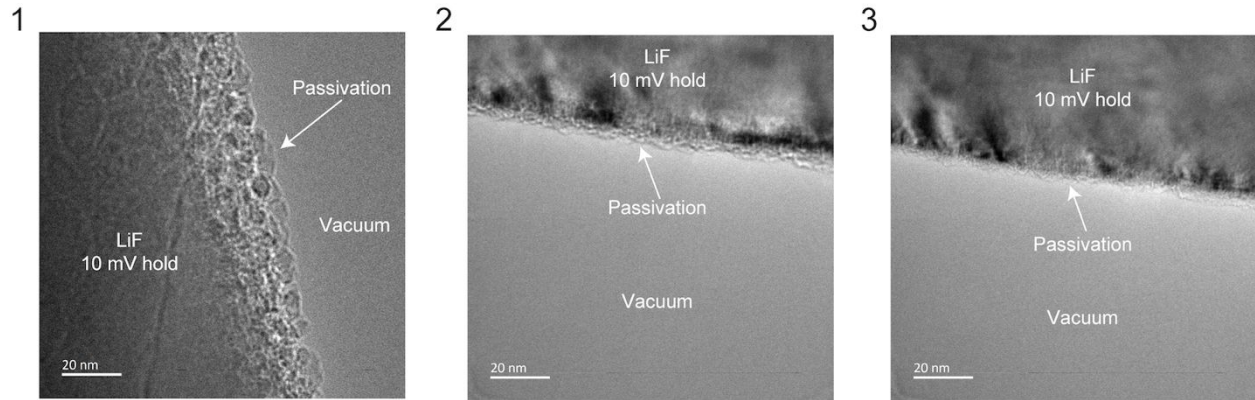
**Note S2 Figure 1.** Cryo-TEM images showing LiF and Li<sub>2</sub>O. Reproduced with permission from Ref.<sup>22</sup> for (a). Copyright 2020 American Chemical Society. Reproduced with permission from Ref.<sup>23</sup> for (b). Copyright 2018 Springer Nature. Reproduced with permission from Ref.<sup>29</sup> for (c). Copyright 2023 Springer Nature. Reproduced with permission from Ref.<sup>25</sup> for (d). Copyright 2021 Wiley-VCH. Reproduced with permission from Ref.<sup>31</sup> for (e). Copyright 2022 American Chemical Society. Reproduced with permission from Ref.<sup>32</sup> for (f). Copyright 2021 Cell Press. Reproduced with permission from Ref.<sup>33</sup> for (g). Copyright 2024 Springer Nature. Reproduced with permission from Ref.<sup>34</sup> for (h). Copyright 2022 Wiley-VCH. Reproduced with permission from Ref.<sup>35</sup> for (i). Copyright 2024 Wiley-VCH. Reproduced with permission from Ref.<sup>36</sup> for (j). Copyright 2022 American Association for the Advancement of Science.

Given that LiF is renowned for its chemical and electrochemical inertness<sup>37</sup>, the observation of Li<sub>2</sub>O passivated LiF in **Figure 1f** was unanticipated. However, other studies have shown such Li<sub>2</sub>O passivation on the surfaces of LiF<sup>22,23,25,29</sup>, where this phenomenon has been overlooked and underdiscussed in previous studies. For instance, it was found that Li<sub>2</sub>O was formed on the surface of LiF due to the reaction of partially extracted Li<sup>+</sup> from LiF with the oxygen in the solvents and lithium difluoro(oxalate)borate (LiDFOB) salt<sup>25</sup>. This suggests that LiF is reactive towards electrolyte solvents and DFOB anion in the electrolyte, which is questionable since LiF is redox stable and an insulating material, and our electrolyte formulation (RE and LiF SE) was LiDFOB-free. Another study posited that the oxalate group in LiDFOB can function as a capping agent for LiF<sup>26</sup>, implying a favored interaction between the oxygenated group in the DFOB anion and LiF. However, the passivation layer on LiF and such interactions were undiscussed. Furthermore, the existence of core@shell LiF@Li<sub>2</sub>O nanostructure, positioned as the indirect-SEI, was observed<sup>22</sup>, but the primary assertion was intended to recognize LiF as the indirect-SEI component, not to clarify the process of Li<sub>2</sub>O formation on LiF. Moreover, a distinct oxygen mapping (Li<sub>2</sub>O) was probed at the surface of LiF, probed by cryo-STEM EELS<sup>23</sup>, but a discussion on this particular observation was absent in the study. Additionally, despite the coexistence of LiF in the vicinity of or directly interfaced with Li<sub>2</sub>O (LiF/Li<sub>2</sub>O) has been observed within the SEIs on Li<sup>0</sup> anodes<sup>31–36</sup>, the tendency of LiF to interface with Li<sub>2</sub>O was not discussed in these studies. Because such Li<sub>2</sub>O passivation or LiF/Li<sub>2</sub>O interfaces were not subject to in-situ (LiF formed by the decomposition of electrolyte species) or ex-situ (suspended LiF in electrolytes that underwent electrochemical cycling) formed LiF, the capability of LiF to form LiF/Li<sub>2</sub>O interface can be a unique characteristic of LiF (unrecognized feature of LiF to date), which Li<sub>2</sub>O passivated LiF<sup>22,23,25,29</sup> (**Figure 1f**) and LiF/Li<sub>2</sub>O interface within the SEI<sup>31–36</sup> collectively support this claim (**Note S2 Figure 1**).

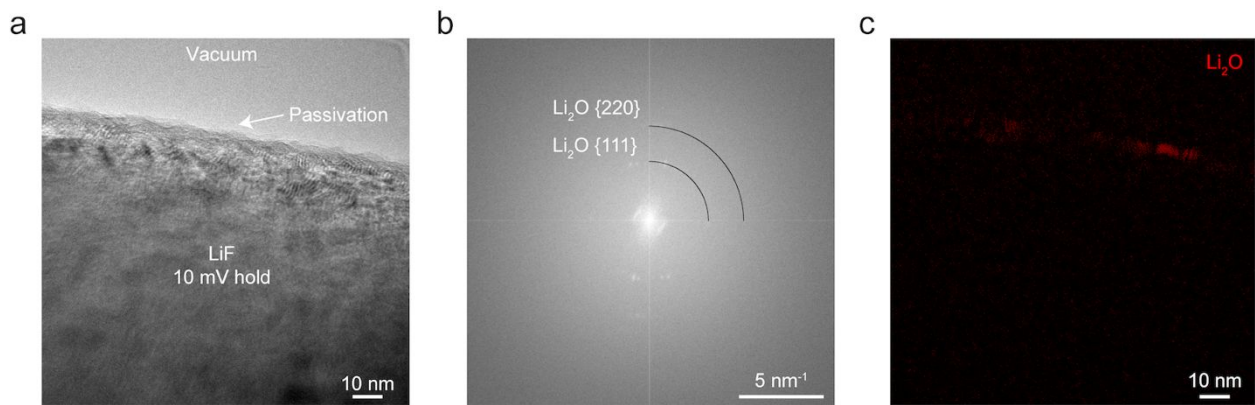
### Note S3 | $\text{Li}_2\text{O}$ passivation mechanism for LiF



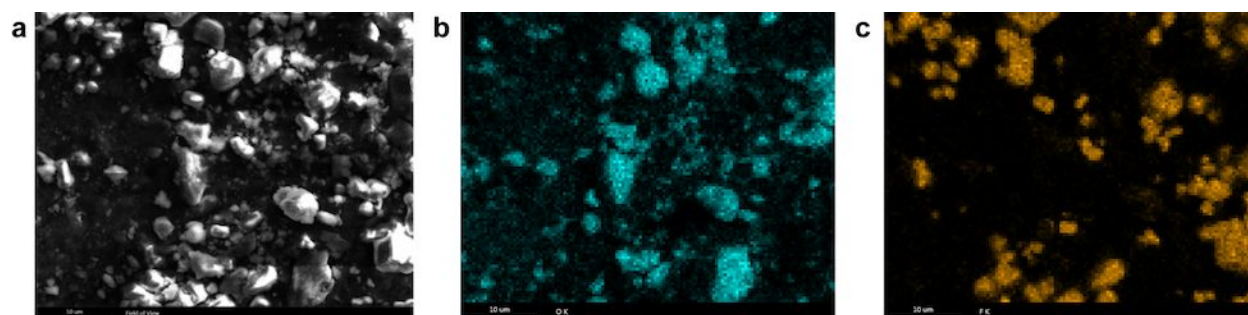
**Note S3 Figure 1.** Cryo-TEM images showing LiF and  $\text{Li}_2\text{O}$ . (a) High magnification cryo-TEM image of (Figure 1a). (b) Cryo-HRTEM image of (a). (c) Cryo-HRTEM image of 10 mV hold LiF suspension. (d) Cryo-TEM image of LiF after physically mixing LiF with  $\text{Li}_2\text{O}$  (7.5 wt% each) in EC:DEC (1:1 v/v) for three days.



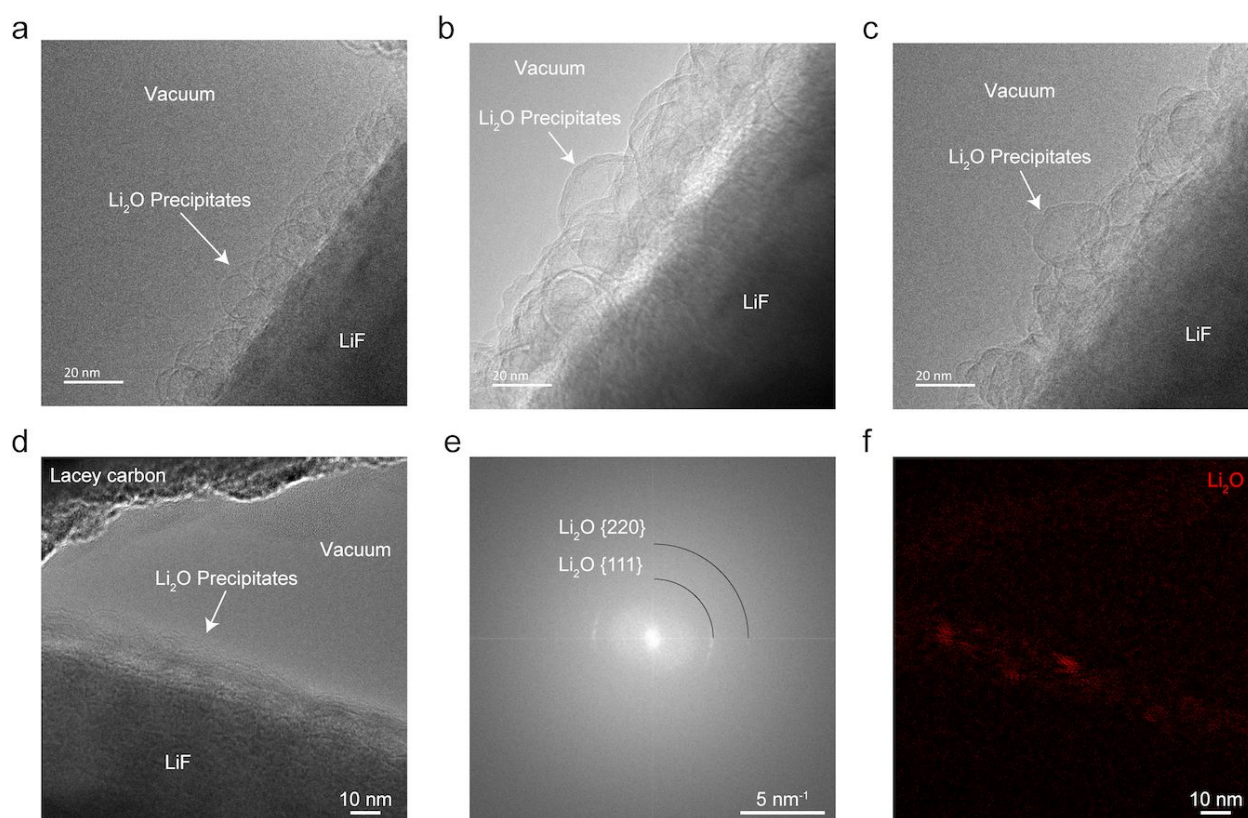
**Note S3 Figure 2.** 10 mV hold of LiF suspension. Three cryo-HRTEM images of LiF suspension after 10 mV vs.  $\text{Li}^+/\text{Li}$  hold for 1 hour from lacey-carbon Cu TEM grid| $\text{Li}^0$  cell with LiF SE. The passivation layer on LiF is indicated by the arrows in images 1 to 3.



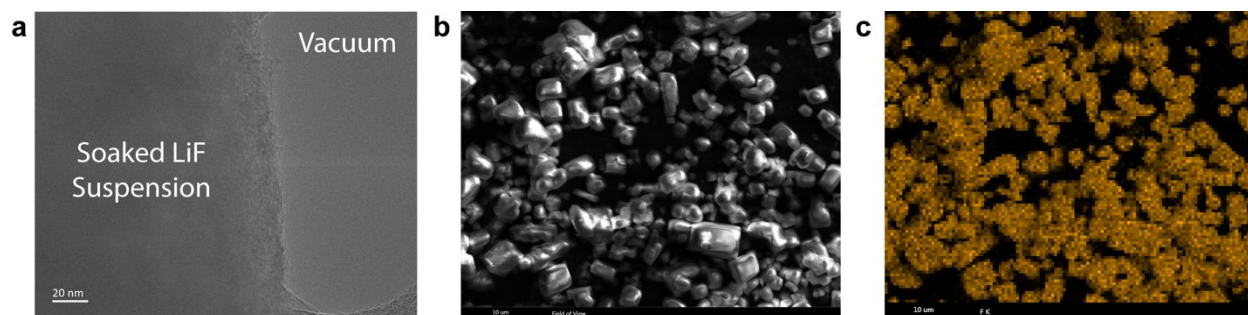
**Note S3 Figure 3.** Analysis of the passivation on 10 mV hold of LiF suspension. (a) Cryo-HRTEM images of LiF after 10 mV vs.  $\text{Li}^+/\text{Li}$  hold for 1 hour from lacey-carbon Cu TEM grid| $\text{Li}^0$  cell with LiF SE. The passivation layer on LiF is indicated by the arrow. (b) FFT of (a), showing  $\text{Li}_2\text{O}$  {111} and {220} diffraction patterns. (c) Inverse FFT of (b), depicting  $\text{Li}_2\text{O}$  {111} in red.



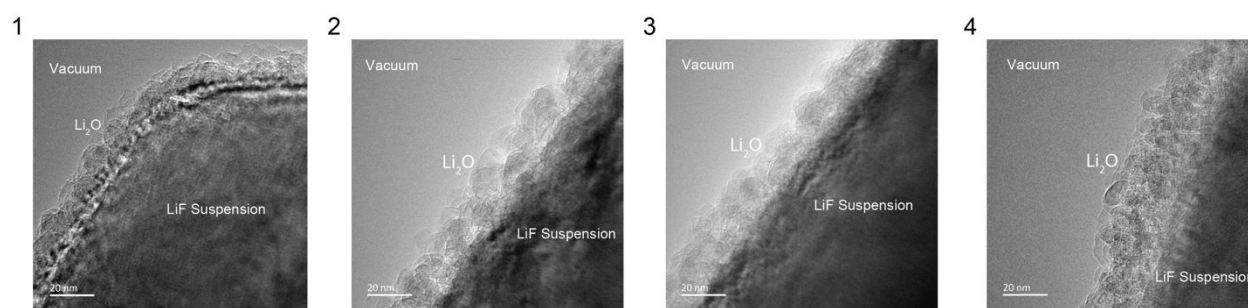
**Note S3 Figure 4.** SEM image of LiF/Li<sub>2</sub>O suspension mixture and corresponding energy-dispersive X-ray spectroscopy (EDXS) elemental mapping of Oxygen and Fluorine. (a) Scanning electron microscopy (SEM) image of LiF and Li<sub>2</sub>O suspension (7.5 wt% each) used in EC:DEC (1:1 v/v) solvents for the Li<sub>2</sub>O precipitation experiment. (b) EDXS O mapping of (a). (c) EDXS F mapping of (a). The scale bar is 10 μm.



**Note S3 Figure 5.** Analysis of Li<sub>2</sub>O precipitation on LiF surfaces. (a-d) Cryo-HRTEM images of LiF immersed with LiF/Li<sub>2</sub>O suspension mixture (7.5 wt% each) in EC:DEC (1:1 v/v) solvents for three days. (e) FFT of (d), showing Li<sub>2</sub>O {111} and {220} diffraction patterns. (f) Inverse FFT of (e), depicting Li<sub>2</sub>O {111} in red.



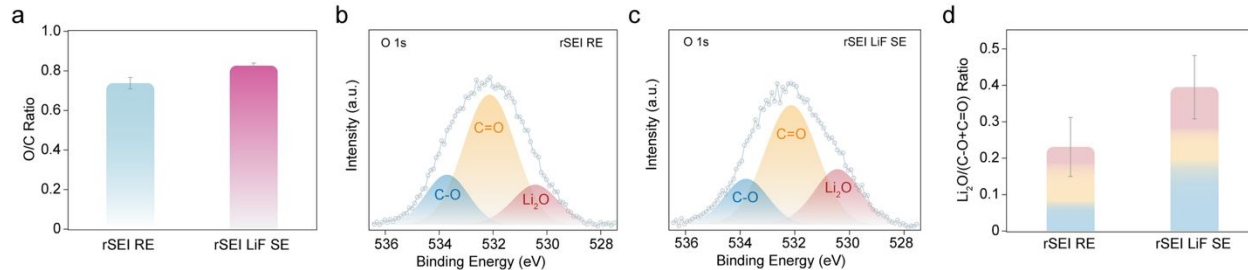
**Note S3 Figure 6.** Cryo-HRTEM and SEM images of soaked LiF suspension and corresponding EDXS elemental mapping of Fluorine. (a) Cryo-HRTEM image of dried LiF suspension that was soaked in EC:DEC (1:1 v/v) solvents for three days. (b) SEM image of identical LiF suspension in (a). The scale bar is 10  $\mu\text{m}$ . (c) EDXS F mapping of (b). The scale bar is 10  $\mu\text{m}$ .



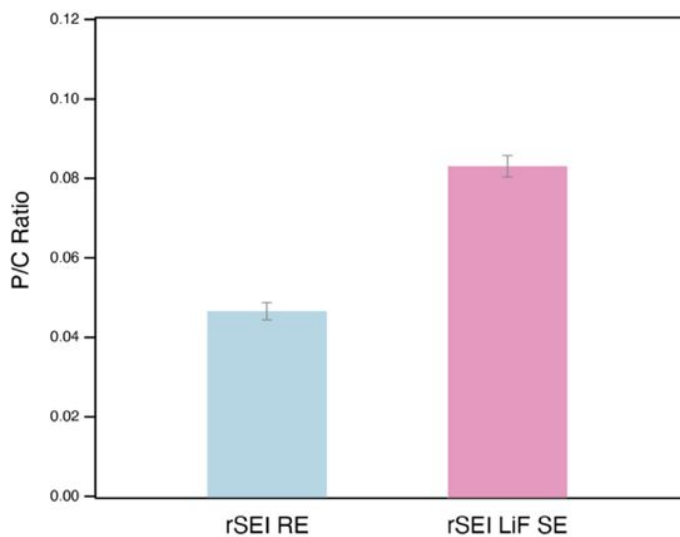
**Note S3 Figure 7.** Cryo-HRTEM images of the LiF suspension in LiF SE after cycling. The cryo-HRTEM images of the LiF suspension were taken after ten complete cycles of  $\text{Li}^0$  plating/stripping at the current density and capacity of 1  $\text{mA cm}^{-2}$  and 1  $\text{mAh cm}^{-2}$  in the lacey-carbon Cu TEM grid| $\text{Li}^0$  cells with LiF SE.

To understand the  $\text{Li}_2\text{O}$  passivation mechanism observed in **Figure 1a-d** and **Note S3 Figure 1a,b**, two experimental conditions were considered: (1) a potential hold at 10 mV vs.  $\text{Li}^+/\text{Li}$  in a lacey carbon-coated Cu TEM grid| $\text{Li}^0$  cell with LiF SE for 1 hour and (2) physically mixing LiF and  $\text{Li}_2\text{O}$  suspensions (7.5 wt% each) in EC:DEC (1:1 v/v) solvent. These conditions allow us to streamline the  $\text{Li}_2\text{O}$  formation pathway to potentially cause the surface passivation of LiF by relying on (1) the electrochemical reduction of the electrolyte species or (2) the physical precipitation of  $\text{Li}_2\text{O}$ . In the former case, the LiF suspension in LiF SE maintained at 10 mV vs.  $\text{Li}^+/\text{Li}$  (10 mV hold LiF suspension) developed a thin passivation layer (**Note S3 Figure 1c** and **Note S3 Figure 2**). The cryo-HRTEM, FFT diffraction, and inverse FFT analyses (**Note S3 Figure 3**) confirmed that the passivation layer formed on 10 mV hold LiF suspension was composed of  $\text{Li}_2\text{O}$ , indicating that  $\text{Li}_2\text{O}$  generated by the electrolyte reduction contributed to surface passivation of LiF, consistent with observations in **Figure 1f-i** and **Figure 2a-d**. However, given that LiF is an insulating compound<sup>37,38</sup>, it is not straightforward to envision redox reactions occurring at the surfaces of LiF. Considering the partial solubility of  $\text{Li}_2\text{O}$  in electrolytes<sup>39-41</sup>, a feasible process for  $\text{Li}_2\text{O}$  passivating LiF surfaces can involve physical precipitation. To directly test this, the latter case is considered, where LiF and  $\text{Li}_2\text{O}$  suspensions (**Note S3 Figure 4**) were physically mixed in EC:DEC (1:1 v/v) solvent for three days, allowing for spontaneous  $\text{Li}_2\text{O}$  dissolution and precipitation to occur. Based on the analysis of the precipitation experiment, vividly clear  $\text{Li}_2\text{O}$  precipitates were observed on LiF surfaces (**Note S3 Figure 1d** and **Note S3 Figure 5**). To ensure that  $\text{Li}_2\text{O}$  precipitation did not result from reactions between LiF and the solvent, just LiF (without  $\text{Li}_2\text{O}$ ) was soaked in EC:DEC solvent for three days. The cryo-TEM and SEM/EDXS analysis of this soaked LiF (**Note S3 Figure 6**) showed no deposits forming on its surfaces. These combined results elucidate that  $\text{Li}_2\text{O}$  passivation on LiF surfaces occurs *via* physical precipitation. Upon closely observing the morphology of  $\text{Li}_2\text{O}$  passivation layers in **Note S3 Figure 1** and **Note S3 Figure 7**,  $\text{Li}_2\text{O}$  exhibits a nanoscale granular particle-like morphology, further supporting the precipitation mechanism.

## Note S4 | Relative $\text{Li}_2\text{O}$ content in rSEI RE and rSEI LiF SE



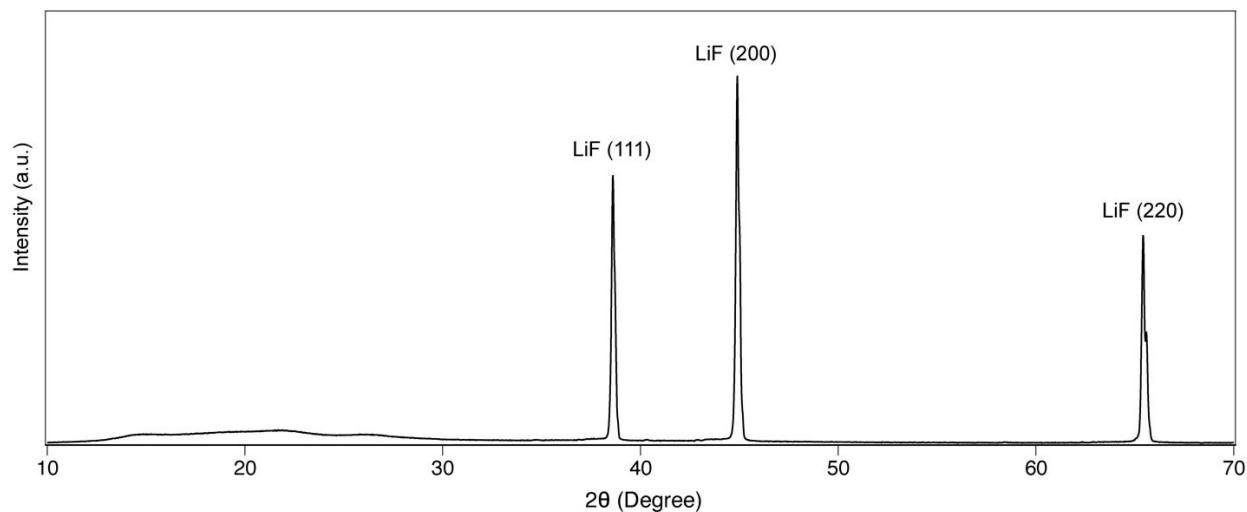
**Note S4 Figure 1.** XPS analysis on rSEI RE and rSEI LiF SE. (a) XPS elemental O/C ratio of rSEI RE ( $0.74 \pm 0.03$ ) and rSEI LiF SE ( $0.83 \pm 0.01$ ). (b-c) Representative high-resolution O 1s XPS spectra of rSEI RE (b) and rSEI LiF SE (c). The deconvolution peaks include C-O, C=O, and  $\text{Li}_2\text{O}$ . (d) Relative ratio of  $\text{Li}_2\text{O}$  to C-O and C=O in rSEI ( $\text{Li}_2\text{O}/\text{C-O}+\text{C=O}$ ) for RE ( $0.231 \pm 0.081$ ) and LiF SE ( $0.395 \pm 0.087$ ). Different colours on each bar plot represent the averaged fraction amount of C-O (blue), C=O (yellow), and  $\text{Li}_2\text{O}$  (red).



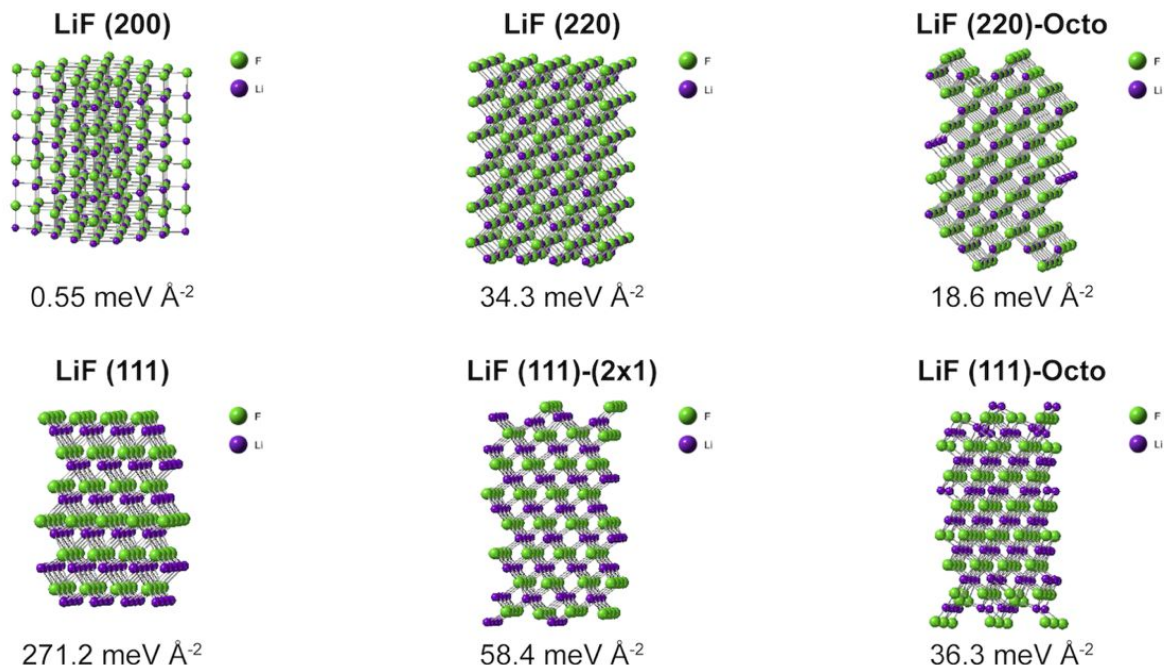
**Note S4 Figure 2.** XPS elemental P/C ratio of rSEI RE and rSEI LiF SE. The average and standard errors are  $0.04689 \pm 0.00211$  for rSEI RE and  $0.08342 \pm 0.00271$  for rSEI LiF SE.

To further corroborate LiF's effect on Li<sub>2</sub>O enrichment, XPS analysis was conducted (**Note S4 Figure 1**) to compare the relative presence of Li<sub>2</sub>O in the rSEIs formed with RE (rSEI RE) and LiF SE (rSEI LiF SE). In **Note S4 Figure 1a**, rSEI LiF SE resulted in a higher O/C ratio ( $0.83 \pm 0.01$ ) than rSEI RE ( $0.74 \pm 0.03$ ). This ratio was analyzed to assess the relative proportions of organic (C-O and C=O species) and Li<sub>2</sub>O in the rSEIs. A comparison of O 1s spectra between rSEI RE (**Note S4 Figure 1b**) and rSEI LiF SE (**Note S4 Figure 1c**) revealed a higher relative presence of Li<sub>2</sub>O and C-O species in rSEI LiF SE, both of which are desirable SEI components for Li<sup>0</sup> anodes<sup>11,18</sup>. To observe a relative content of Li<sub>2</sub>O in the rSEIs, the ratio of Li<sub>2</sub>O over combined organic SEI species (C-O and C=O), notated as Li<sub>2</sub>O/(C-O + C=O), was calculated (**Note S4 Figure 1d**) by integrating the deconvoluted peaks from **Note S4 Figure 1b** and **Note S4 Figure 1c**. The relative Li<sub>2</sub>O content in rSEI LiF SE ( $0.395 \pm 0.087$ ) was higher than that in rSEI RE ( $0.231 \pm 0.081$ ), supporting the observed effect of LiF in enriching Li<sub>2</sub>O (**Figure 1b-e**). To understand the role of LiF in the Li<sub>2</sub>O enrichment, the P/C ratio (reflecting anion-to-solvent decomposition ratio) was measured for rSEI RE and rSEI LiF SE (**Note S4 Figure 2**), as it was found that Li<sub>2</sub>O predominantly forms from the reduction of PF<sub>6</sub> anion's intermediates with solvents, rather than from pure solvent reduction<sup>29,30,42</sup>. The P/C ratio was higher for rSEI LiF SE, demonstrating that LiF enhanced anion decomposition, which can promote Li<sub>2</sub>O formation within the SEI. On a side note, we have collected high-resolution F 1s spectra *via* XPS, which exhibited an enhanced LiF signal for LiF SE compared to RE. However, it is technically challenging to quantify the relative amount of in-situ formed LiF within the SEI because residual LiF suspension particles are often embedded in the Li<sup>0</sup> electrodeposits (**Figure S12b**). This makes it difficult to physically separate in-situ formed LiF from residual LiF suspension particulates, thereby complicating the deconvolution of F 1s signals and limiting the utility of depth-profiling for quantitative analysis.

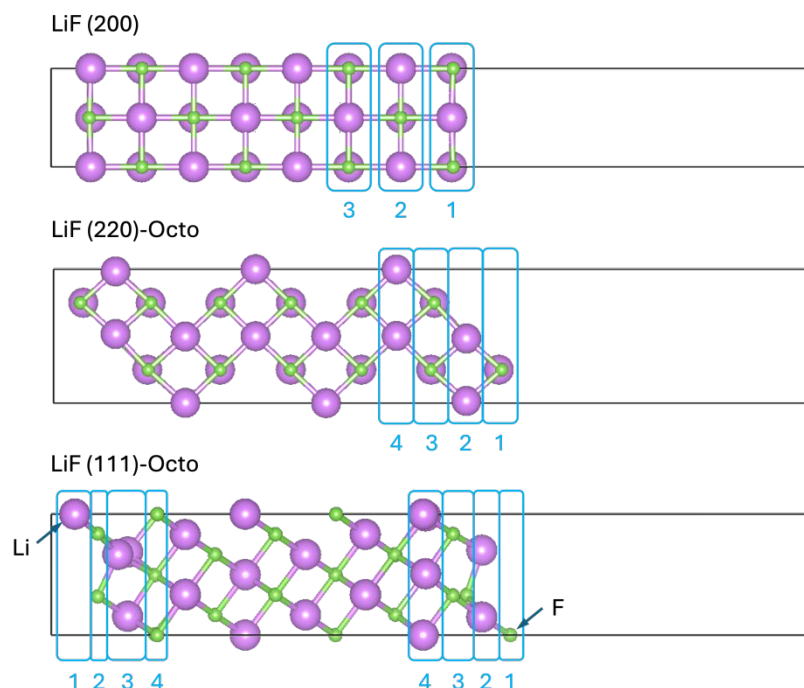
## Note S5 | Determining the right structures of LiF for DFT analysis



**Note S5 Figure 1.** XRD profile of LiF suspension. The observed structures of LiF were (111), (200), and (220).



**Note S5 Figure 2.** Molecular structure and corresponding formation energy of LiF. The experimentally relevant structures of LiF are illustrated with the corresponding formation (surface) energies. The LiF (200), LiF (220), and LiF (111) are the pristine LiF structures. The octopolar reconstructed LiF structures of LiF (200) and LiF (111) are denoted as LiF (200)-Octo and LiF (111)-(2x1)/LiF (111)-Octo, respectively.



Layer no.	LiF (200)	LiF (220)-Octo	LiF (111)-Octo-F	LiF (111)-Octo-Li
1	Li: 0.90 F: -0.90	Li: 0.90 F: -0.90	F: -0.90	Li: 0.90
2	Li: 0.90 F: -0.90	Li: 0.89 F: -0.90	Li: 0.89	F: -0.89
3	Li: 0.90 F: -0.90	Li: 0.88 F: -0.89	F: -0.89	Li: 0.89
4		Li: 0.89 F: -0.89	Li: 0.89	Li: 0.90

**Note S5 Figure 3.** Schematics illustrating the layer numbers of LiF (200), LiF (220)-Octo, LiF (111)-Octo-F, and LiF (111)-Octo-Li in the DFT Bader charge calculations. The Bader partial charge values are summarized in the table.

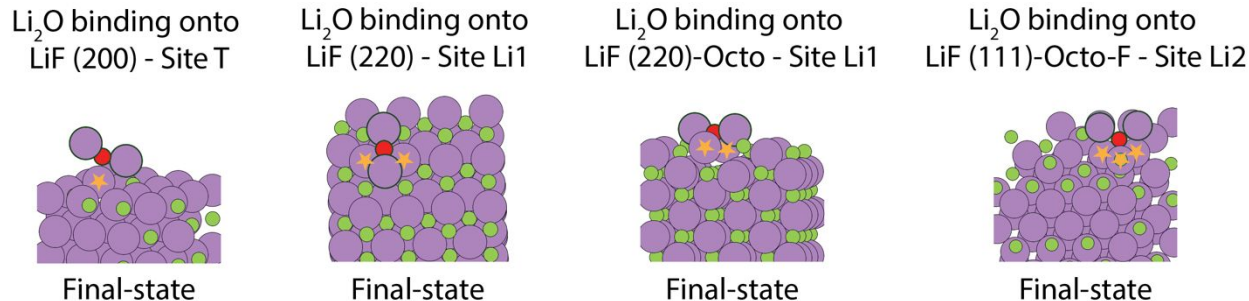
In the DFT analysis, establishing stable and empirically relevant LiF structures is crucial to bridge simulation outputs with the experimental results. Therefore, it is essential to select experimentally verified structures of LiF, namely LiF (200), LiF (220), and LiF (111) (**Note S5 Figure 1**), to accurately simulate and correlate the simulation outputs with experimental results. As a rule of thumb, the lowest formation energy of a specific LiF structure must be obtained first due to stability concerns<sup>43</sup>. This implies that LiF (200), LiF (220), and LiF (111) structures can be used in the simulation only if they demonstrate relatively low formation energies. For instance, the calculated surface energies of pristine LiF (200), LiF (220), and LiF (111) were 0.55 meV Å<sup>-2</sup>, 34.3 meV Å<sup>-2</sup>, and 271.2 meV Å<sup>-2</sup>, respectively (**Note S5 Figure 2**). It is evident that the formation energy of LiF (111) was abnormally high (271.2 meV Å<sup>-2</sup>), due to the diverging electrostatic energy of periodic dipole moments induced by the asymmetric polar surfaces of the pristine LiF (111). This suggests that using the pristine LiF (111) in simulations can lead to unreliable results. To illustrate this point, the binding energy of Li adatom onto LiF (111) was calculated to be -8.65

eV (not shown here), which is an unrealistic value that can potentially lead to misinterpretation of experimental results.

To ensure an accurate correlation between the simulation outputs and the experimental results, we performed a surface reconstruction of LiF structures based on a comprehensive literature survey to minimize the formation energy of LiF<sup>44,45</sup>. We found that octopolar reconstruction was thermodynamically favored for both LiF (220) and LiF (111) structures, in which LiF (220)-Octo, LiF (111)-Octo, and LiF (111)-(2x1) reconstructions were determined to be energetically stable. To entirely cover the possible structures of LiF, the formation energies of both pristine and reconstructed LiF structures were computed (**Note S5 Figure 2**): 0.55 meV Å<sup>-2</sup> for LiF (200), 34.3 meV Å<sup>-2</sup> for LiF (220), 18.6 meV Å<sup>-2</sup> for LiF (220)-Octo, 58.4 meV Å<sup>-2</sup> for LiF (111)-(2x1), and 36.3 meV Å<sup>-2</sup> for LiF (111)-Octo. The most stable (those with the lowest formation energy) LiF structures in the family of LiF (200), LiF (220), and LiF (111) were LiF (200), LiF (220)-Octo, and LiF (111)-Octo, respectively. Consequently, we selected LiF (200), LiF (220)-Octo, and LiF (111)-Octo structures for our simulations to establish a reliable connection between the simulation results and experimental findings. Since LiF (111) structures comprise fluorine and lithium-terminated surfaces, we examined both surfaces to gain a better understanding of the termination characteristics for LiF (111)-Octo. The fluorine and lithium-terminated surfaces of LiF (111)-Octo are indicated by LiF (111)-Octo-F and LiF (111)-Octo-Li. Because the pristine LiF (220) had a relatively stable structure among the others (**Note S5 Figure 2**), but less stable than LiF (220)-Octo, both LiF (220) along LiF (220)-Octo were analyzed in the DFT analysis. Overall, the DFT analysis was conducted with LiF (200), LiF (220), LiF (220)-Octo, LiF (111)-Octo-F, and LiF (111)-Octo-Li surfaces, which include all experimentally relevant structures of LiF that are reliable for conducting simulations.

We note that in classical MD simulations (discussed later), charge scaling is a standard practice to account for the dielectric screening in the solution environment. A typical scaling factor is 0.7-0.8 of the partial charge values in vacuum<sup>46</sup>. The calculated Bader partial charges of the outermost atoms in LiF (200), LiF (220)-Octo, and LiF (111)-Octo are listed in **Note S5 Figure 3**. Based on the calculated values, it is evident that ±0.7 is a reasonable value for Li (+) and F (-).

### Note S6 | The binding affinity of Li<sub>2</sub>O for LiF surfaces



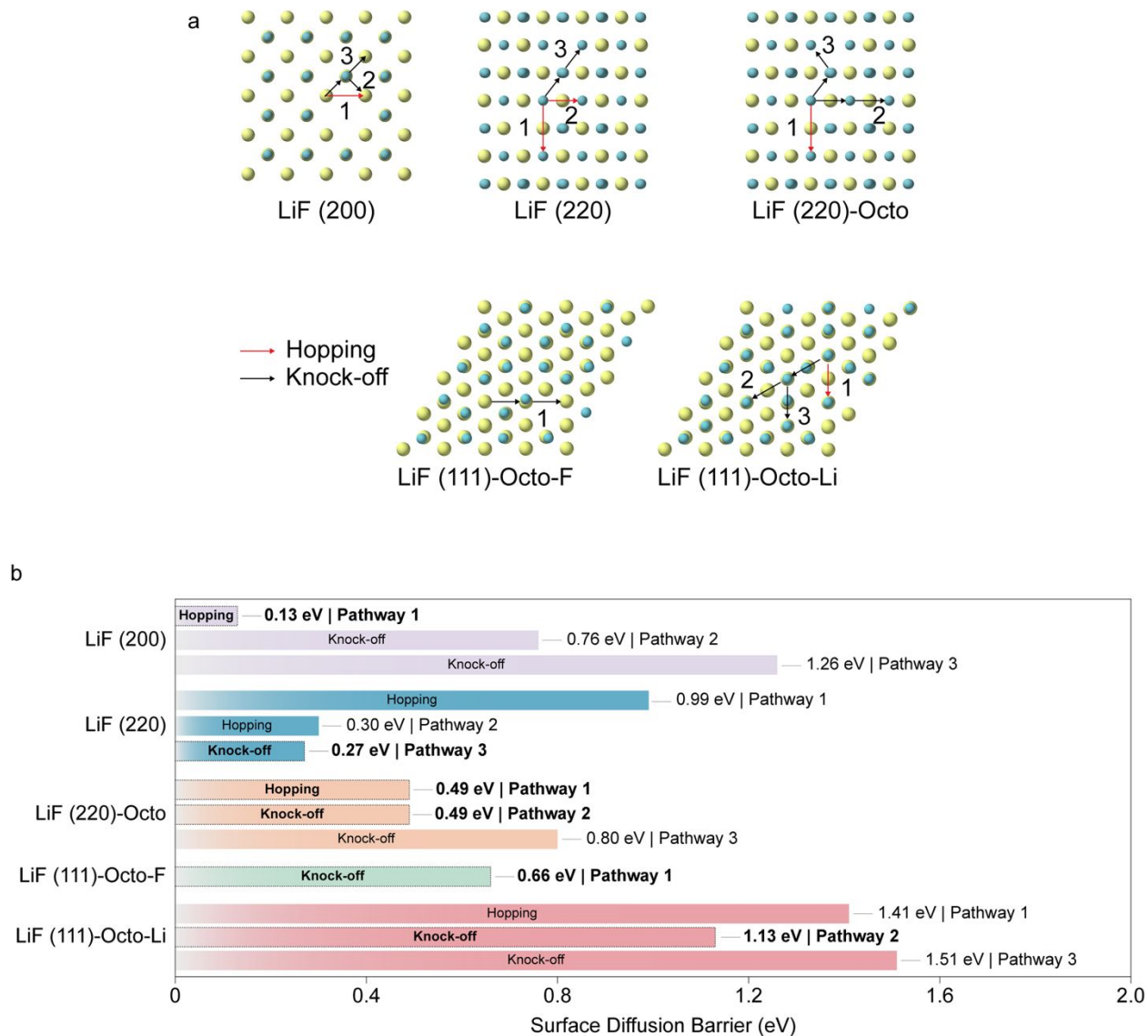
**Note S6 Figure 1.** Li<sub>2</sub>O binding configuration on LiF surfaces. The schematic illustrates the binding interaction between the oxygen atom in Li<sub>2</sub>O and Li atom on the specified LiF surface that exhibits the lowest binding energy in **Figure 3b**. The Li<sub>2</sub>O molecule is marked with the bordered circle, and the binding Li atom interacting with the oxygen in Li<sub>2</sub>O is indicated by the filled orange star. The color coding for Li, F, and O is purple, green, and red, respectively.

Analyzing the binding energies of Li<sub>2</sub>O on LiF surfaces offers detailed insights into the process of Li<sub>2</sub>O passivation and precipitation on the surfaces of LiF (**Figure 1f-i** and **Figure 2a-d**). To systematically analyze the interaction between Li<sub>2</sub>O and LiF, the binding energies of Li<sub>2</sub>O and LiF molecules on Li<sub>2</sub>O and LiF surfaces were calculated (**Figure 3b**). The calculated binding energies of Li<sub>2</sub>O and LiF for the Li<sub>2</sub>O (111) surface at T and H sites were -2.98 eV (T site), -3.03 eV (H site) for Li<sub>2</sub>O and -2.32 eV (H site), -2.51 eV (T site) for LiF. This means that, in the presence of both Li<sub>2</sub>O and LiF molecules, Li<sub>2</sub>O prefers to bind with its surface (preferred self-binding) instead of LiF. For LiF surfaces, the most favorable self-binding energies, equivalent to the epitaxial adsorption binding energy of LiF for each surface structure of LiF, were -2.06 eV (T site on LiF (200)), -2.66 eV (Li1 site on LiF (220)), -3.45 eV (Li1 site on LiF (220)-Octo), -2.90 eV (F4 site on LiF (111)-Octo-F), and -3.11 eV (F2 site on LiF (111)-Octo-Li). For Li<sub>2</sub>O binding to LiF surfaces, the most favorable binding energies were -2.67 eV (T site on LiF (200)), -4.90 eV (Li1 site on LiF (220)), -3.53 eV (Li1,2 sites on LiF (220)-Octo), -4.78 eV (Li2 site on LiF (111)-Octo-F), and -4.31 eV (Li4 site on LiF (111)-Octo-Li). These binding energies indicate that Li<sub>2</sub>O adsorption onto the surfaces of LiF is thermodynamically favorable compared to the self-binding of LiF, as all the binding energies of Li<sub>2</sub>O were more negative than that of LiF for LiF surfaces (**Figure 3b**). Given that both Li<sub>2</sub>O and LiF molecules and surfaces are present in operating battery cells, all the binding energies in **Figure 3b** were comprehensively compared to determine the general preference of Li<sub>2</sub>O binding to LiF surfaces. By comparing the values across the surfaces of Li<sub>2</sub>O and LiF, the corresponding binding energies show that Li<sub>2</sub>O prefers to bind with LiF surfaces over its surface, while LiF favors binding with itself, except for the LiF (200) surface. For the LiF (200) surface, the calculated binding energies of Li<sub>2</sub>O at H and T sites on LiF (200) were -2.53 eV and -2.67 eV, which were more positive than Li<sub>2</sub>O on Li<sub>2</sub>O (111) but more negative than LiF on Li<sub>2</sub>O (111). Such binding characteristics for the LiF (200) surface indicate that while LiF (200) is the least favorable surface for Li<sub>2</sub>O binding, Li<sub>2</sub>O binding is still favored for LiF (200), as evidenced by the more positive binding energies of LiF on Li<sub>2</sub>O (111).

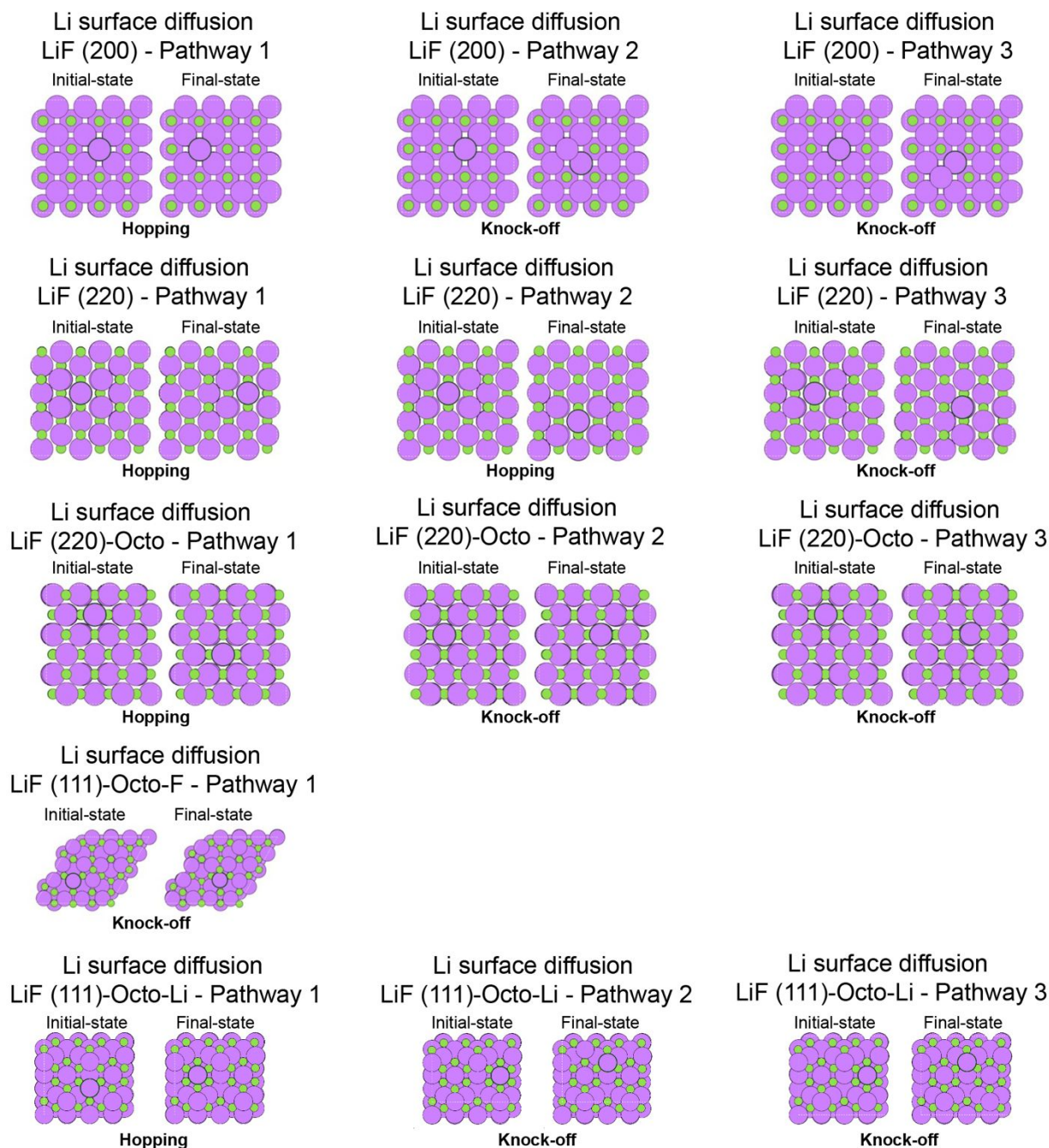
Additionally, the relatively weak binding affinity of Li<sub>2</sub>O for the LiF (200) surface, compared to other surfaces, arises from the minimal binding interactions between Li<sub>2</sub>O and LiF (200), as shown

in **Note S6 Figure 1**. Analyzing the  $\text{Li}_2\text{O}$  binding to each LiF surface type with the highest binding affinity revealed that the LiF (200) surface has the fewest interacting Li atoms with the oxygen in  $\text{Li}_2\text{O}$ . Specifically, the number of interacting Li atoms on the LiF surface with the oxygen in  $\text{Li}_2\text{O}$  is one for LiF (200), two for LiF (220) and LiF (220)-Octo, and three for LiF (111)-Octo. This trend suggests that the lower binding energy, therefore the higher binding affinity, of  $\text{Li}_2\text{O}$  is positively correlated with the number of interacting Li atoms on the LiF surface, with LiF (200), having the fewest interactions, exhibiting the lowest  $\text{Li}_2\text{O}$  binding affinity. Since only the LiF (200) surface exhibited relatively weak interaction with  $\text{Li}_2\text{O}$  among the five LiF surface types, it is found that  $\text{Li}_2\text{O}$  binding on LiF surfaces is generally a thermodynamically favored process.

### Note S7 | Surface diffusion barrier of LiF

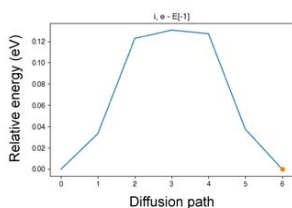


**Note S7 Figure 1.** Surface diffusion barriers for LiF surfaces. (a) Surface structures of LiF (200), LiF (220), LiF (220)-Octo, LiF (111)-Octo-F, and LiF (111)-Octo-Li describing surface diffusion pathways for Li. The hopping and knock-off diffusions are indicated by the red and black arrows. The numbers on each LiF surface denote the paths of surface diffusion. (b) Li surface diffusion barriers of LiF surfaces based on the pathways depicted in (a). The lowest diffusion barriers are outlined by the dashed stroke for each LiF surface.

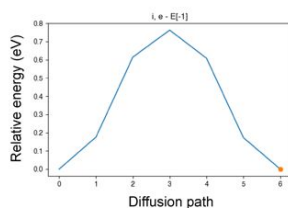


**Note S7 Figure 2.** Li surface diffusion onto LiF surfaces. The images illustrate Li surface diffusion for the specified pathways on LiF surfaces. The initial and final diffusion states, as well as the surface diffusion mechanism of Li are shown for each LiF structure.

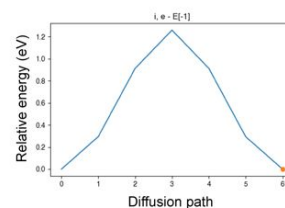
Li surface diffusion  
LiF (200) - Pathway 1



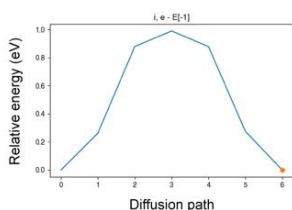
Li surface diffusion  
LiF (200) - Pathway 2



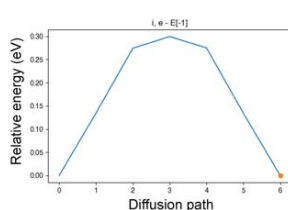
Li surface diffusion  
LiF (200) - Pathway 3



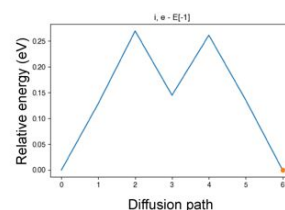
Li surface diffusion  
LiF (220) - Pathway 1



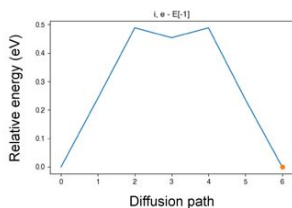
Li surface diffusion  
LiF (220) - Pathway 2



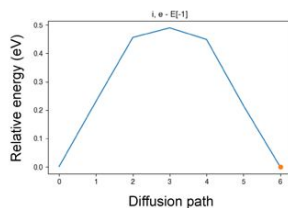
Li surface diffusion  
LiF (220) - Pathway 3



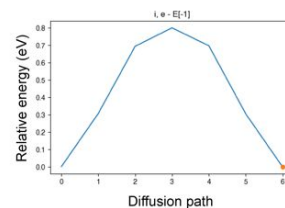
Li surface diffusion  
LiF (220)-Octo - Pathway 1



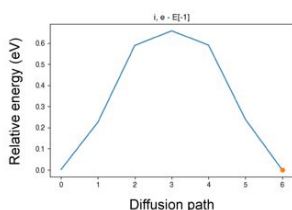
Li surface diffusion  
LiF (220)-Octo - Pathway 2



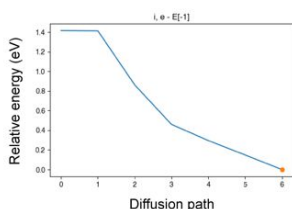
Li surface diffusion  
LiF (220)-Octo - Pathway 3



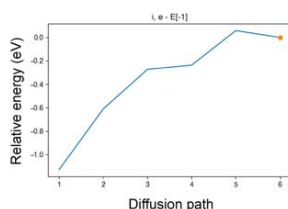
Li surface diffusion  
LiF (111)-Octo-F - Pathway 1



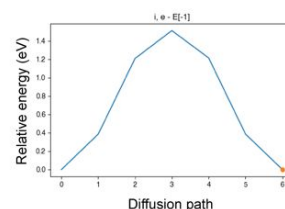
Li surface diffusion  
LiF (111)-Octo-Li - Pathway 1



Li surface diffusion  
LiF (111)-Octo-Li - Pathway 2



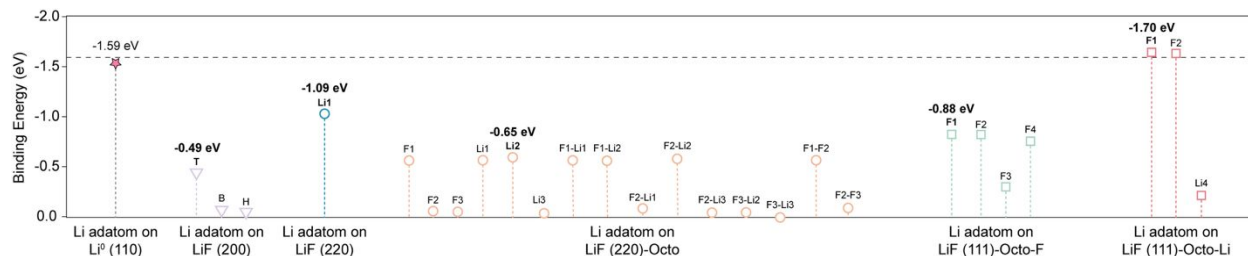
Li surface diffusion  
LiF (111)-Octo-Li - Pathway 3



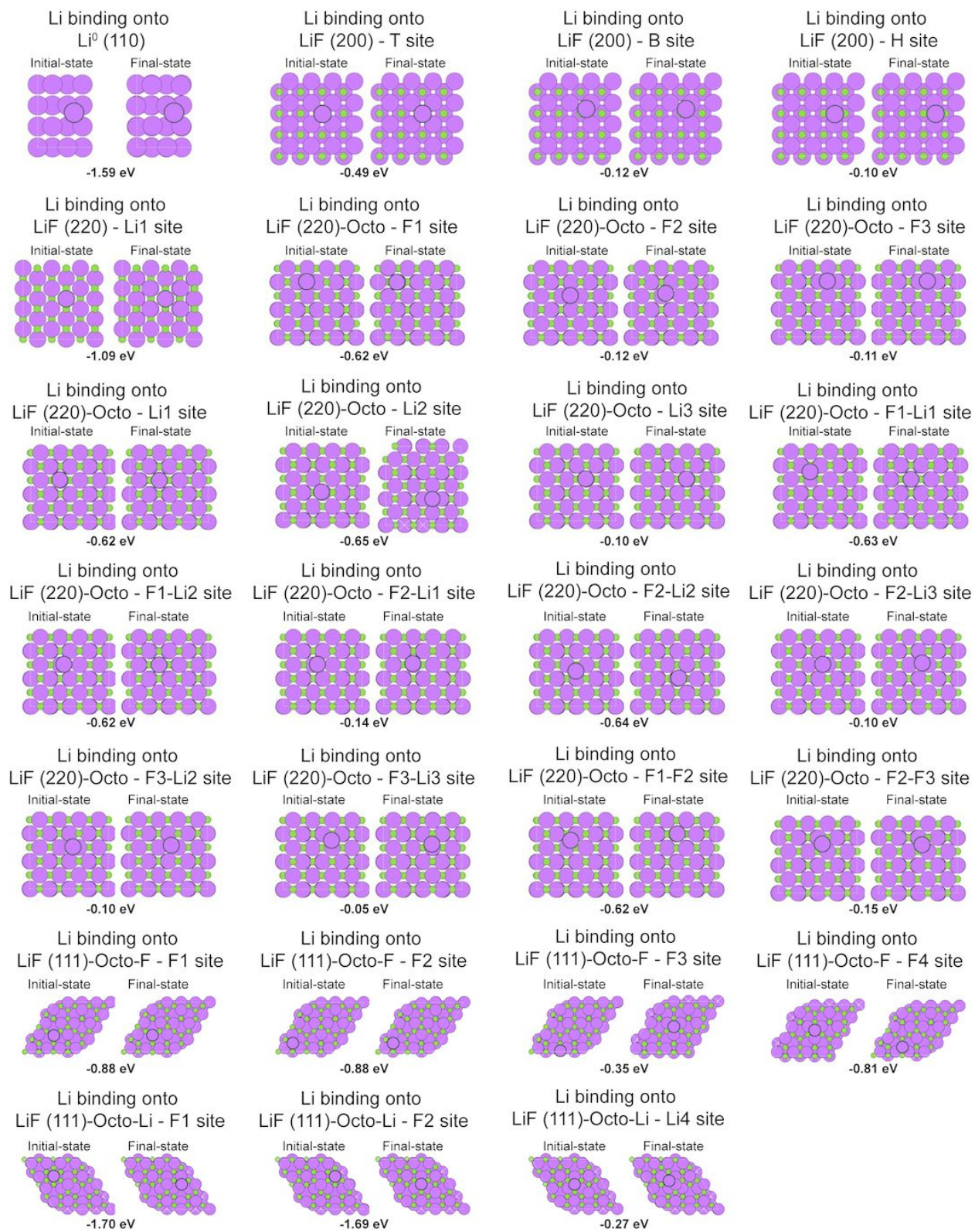
**Note S7 Figure 3.** The relative energy profiles for Li surface diffusion barrier of LiF. The relative energy profiles of the specified Li surface diffusion pathway on the specific LiF surfaces retrieved from DFT analysis. The surface diffusion barrier was calculated by taking the magnitude between the highest and lowest relative energy values. The y-axis and x-axis represent relative energy in eV and diffusion path.

Despite the lack of LiF presence in the compact-SEI<sup>21-29</sup> (**Figure 1b-e**) and observation of LiF/Li<sub>2</sub>O indirect-SEI<sup>22,23,25,29</sup> (**Figure 2e-k**), the role of LiF in SEIs has centered on its ability to facilitate Li diffusion across LiF surfaces<sup>47-49</sup>. To investigate this, we analyzed surface diffusion barriers for a range of experimentally observed LiF surfaces, as previous studies have examined a limited selection<sup>37,50</sup>. Based on the surface structures of LiF, Li surface diffusion pathways *via* hopping and knock-off mechanisms are illustrated in **Note S7 Figure 1a** and **Note S7 Figure 2**, with corresponding relative energy curves shown in **Note S7 Figure 3**. After examining the surface diffusion pathways and mechanisms, the most energetically favorable surface diffusion barrier, pathway, and diffusion type were determined as 0.13 eV|Pathway 1|Hopping for LiF (200), 0.27 eV|Pathway 3|Knock-off for LiF (220), 0.49 eV|Pathway 1,2|Hopping/Knock-off for LiF (220)-Octo, 0.66 eV|Pathway 1|Knock-off for LiF (111)-Octo-F, and 1.13 eV|Pathway 2|Knock-off for LiF (111)-Octo-Li (**Note S7 Figure 1b**). Although surface diffusion is generally more favorable than bulk diffusion for LiF<sup>37</sup>, the surface diffusion barriers vary considerably, from 0.13 to 1.13 eV, depending on the LiF surface structure. As summarized in **Note S7 Figure 1b**, besides LiF (200), most LiF surfaces exhibit relatively high surface diffusion barriers<sup>50</sup>, demonstrating that the role of LiF in promoting Li surface diffusion is valid to some extent but might not be broadly applicable across LiF surfaces.

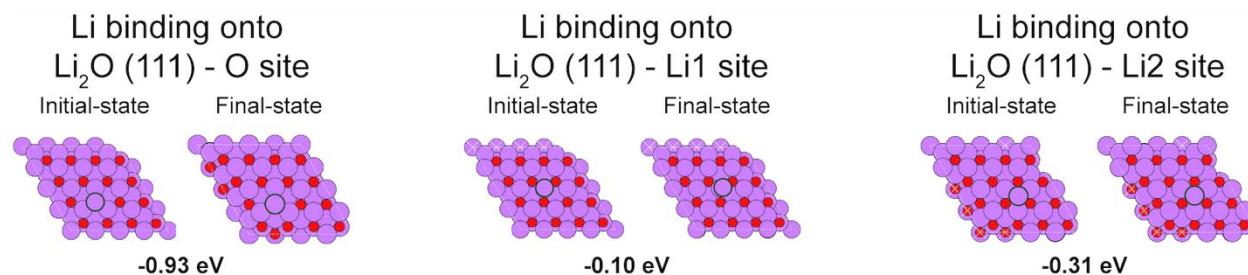
## Note S8 | Understanding lithiophobicity of LiF



**Note S8 Figure 1.** Binding energies of Li adatom onto Li<sup>0</sup> (110), LiF (200), LiF (220)-Octo, LiF (111)-Octo-F, and LiF (111)-Octo-Li surfaces. Li adatom on Li<sup>0</sup> (110) serves as the reference value, which is indicated by the dashed grey line and filled red star. Top (T), bridge (B), hollow (H), Li1~4, F1~4, F1~3-Li1~3, and F1,2-F2,3 (refer to **Note S8 Figure 2**) are the Li binding sites on the specified surfaces of LiF. The most favourable Li adatom binding site and corresponding binding energy for each LiF surface are highlighted in bold text.



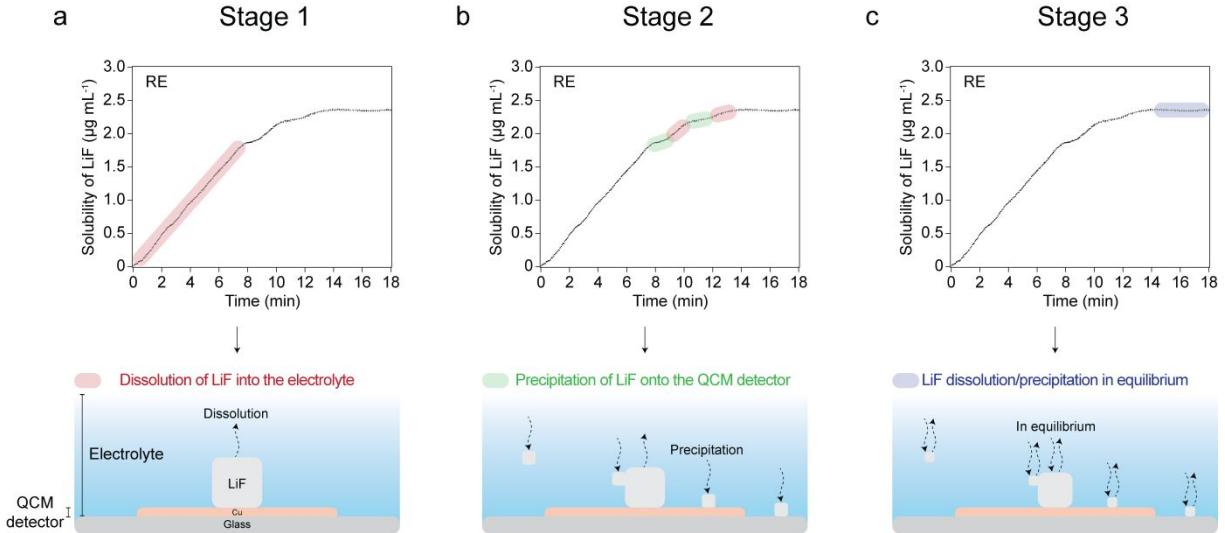
**Note S8 Figure 2.** Li adatom binding sites for LiF. The images illustrate Li adatom binding to the specified sites on LiF surfaces. The initial and final binding states of Li adatom are shown for each binding site and structure of LiF, including the binding energies.



**Note S8 Figure 3.** Li adatom binding on O (Oxygen), Li1, and Li2 sites for the  $\text{Li}_2\text{O}$  (111) surface. The images illustrate Li adatom binding to the specified sites on the  $\text{Li}_2\text{O}$  (111) surfaces. The initial and final binding states of Li adatom are shown for each binding site and structure of  $\text{Li}_2\text{O}$ , including the binding energies. The most favourable binding site and energy for  $\text{Li}_2\text{O}$  are O site and -0.93 eV, respectively.

Although the distribution of LiF/ $\text{Li}_2\text{O}$  indirect-SEI (**Figure 2e**), the interfacing mechanism of LiF with  $\text{Li}_2\text{O}$  (**Figure 2a-d**, **Figure 3a,b**, and **Note S3**), and the benefit of LiF/ $\text{Li}_2\text{O}$  interface (**Figure 3d**) have been examined, the lack of LiF presence within the compact-SEI (**Figure 1b-e**) remains a puzzling phenomenon. To further investigate this, Li adatom binding energies on LiF surfaces were calculated (**Note S8 Figure 1**). The Li binding energy of  $\text{Li}^0$  (110), which is a typical  $\text{Li}^0$  structure<sup>19,51</sup>, was used as the baseline to assess Li binding affinity for LiF surfaces. Calculations were conducted across 26 unique binding sites on LiF surfaces, covering all potential Li adatom binding sites. The initial and final configurations for these binding sites are depicted in **Note S8 Figure 2**. Of the 26 sites examined in **Note S8 Figure 1**, only F1 (-1.70 eV) and F2 (-1.69 eV) sites on the LiF (111)-Octo-Li surface exhibited binding energies comparable to the baseline (-1.59 eV), where the remaining 24 sites showed significantly weaker binding affinities (more positive binding energies). After summarizing Li binding energies on LiF surfaces, the most negative binding energies for each LiF surface were determined as -0.49 eV for LiF (200), -1.09 eV for LiF (220), -0.65 eV for LiF (220)-Octo, -0.88 eV for LiF (111)-Octo-F, and -1.70 eV for LiF (111)-Octo-Li. This trend confirms that LiF surfaces generally exhibit weak binding with Li, aligning with lithiophobic characteristics (high interfacial energies and weak interaction with Li) of LiF<sup>52-54</sup>. The weak Li binding affinity on LiF surfaces suggests that the electrodeposition of  $\text{Li}^0$  along the surfaces of LiF is not thermodynamically favored, helping to explain why LiF is typically located in the outer regions of SEIs<sup>31,32,36</sup> and manifests as indirect-SEIs<sup>22,26-28</sup> for  $\text{Li}^0$  anodes. Although the lithiophobicity of LiF supports its unfavored placement to  $\text{Li}^0$  surface or inner regions of the compact-SEI, lithiophobicity alone cannot fully account for the distribution characteristic in the SEI. For instance,  $\text{Li}_2\text{O}$  is dominantly observed in the compact-SEI (**Figure 1b-e**), despite its relatively low Li binding affinity of -0.93 eV (**Note S8 Figure 3**). Given that LiF is more soluble than  $\text{Li}_2\text{O}$ <sup>40,41</sup>, the solubility of LiF in the electrolyte can play a more significant role in affecting its spatial distribution within the SEI.

## Note S9 | Solubility of LiF in the electrolyte



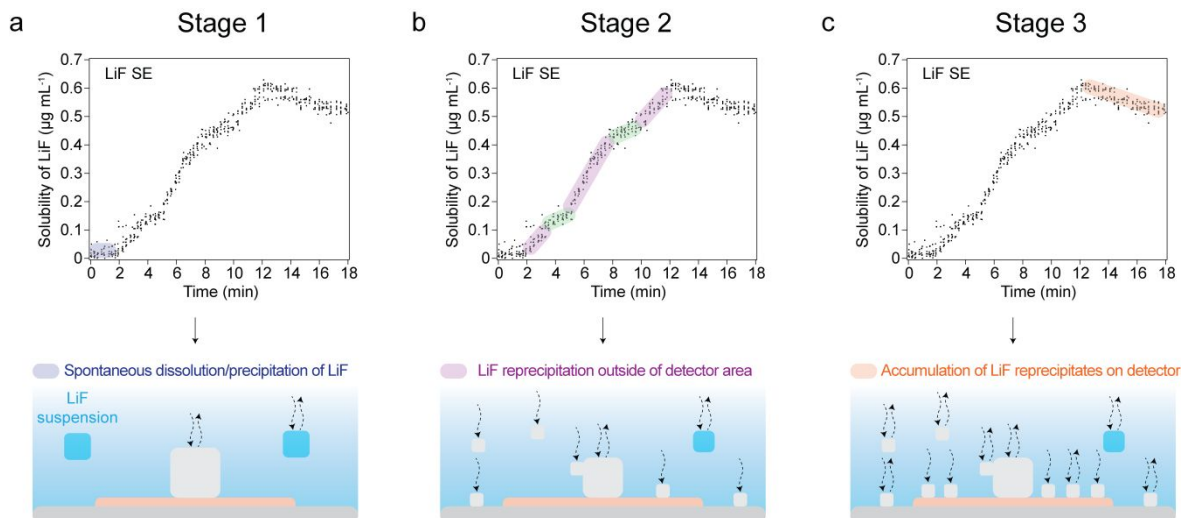
**Note S9 Figure 1.** Solubility profile of LiF in RE measured by the QCM. The dissolution behaviour of LiF in RE is represented by three distinct stages. (a), In Stage 1, LiF dissolves continuously into the electrolyte, highlighted by the red region in the profile. (b), During Stage 2, dissolved LiF begins to precipitate onto the QCM detector and outside of the QCM detector area, highlighted by the green regions in the profile. The regions highlighted in red indicate the suppressed dissolution of LiF on the QCM detector, a result of LiF reaching saturation in RE. (c), In Stage 3, LiF dissolution and precipitation are at equilibrium, highlighted by the blue region in the profile. Schematic illustrations corresponding to each stage provide a dynamic representation of LiF's dissolution and precipitation process in RE during the QCM measurement.

With a sensitivity range from  $\text{ng cm}^{-2}$  to  $\mu\text{g cm}^{-2}$ , QCM offers the necessary resolution<sup>55</sup> for tracking LiF dissolution dynamics in the electrolyte. For the measurement, LiF (identical to the suspension used in LiF SE) was first placed on the QCM detector to calibrate and stabilize the sensor. The electrolyte was then injected into QCM sensor holder, and the resulting mass change of LiF on the QCM detector was recorded over time to measure its dissolution/precipitation behavior in RE and LiF SE at room temperature (**Figure 3e**). In **Figure 3f**, the solubility of LiF on the QCM detector in RE was plotted by recording the mass change of LiF (measured in  $\mu\text{g mL}^{-1}$  on the y-axis) versus the electrolyte exposure time (in minutes on the x-axis). Note that an increase in the solubility of LiF curve corresponds to a decrease in the mass of LiF on the QCM detector over time.

The solubility profile in **Figure 3f** illustrates three stages of LiF dissolution process (**Note S9 Figure 1**). In Stage 1 (highlighted in red in **Note S9 Figure 1a**), continuous dissolution of LiF in RE occurs over approximately the first 8 minutes. During Stage 2, from around 8 to 14 minutes, the dissolution rate of LiF slows down as LiF nears saturation. Under this reduction in rate, the profile curves in Stage 2 show inflection points (highlighted in red and green in **Note S9 Figure 1b**), indicating shifts in the LiF dissolution rates and suggesting a dynamic process of concurrent dissolution/precipitation. The following scenarios can explain these varying dissolution rates in a saturated environment: (1) dissolved LiF precipitating onto LiF on the QCM detector, (2) dissolved

LiF precipitating onto the detector area, or (3) dissolved LiF precipitating outside the detector area. Because QCM can only measure the mass changes at the detector surface, scenario (3) can be ruled out. However, scenarios (1) and (2) would result in a reduced apparent dissolution rate, as spontaneous LiF precipitation in these cases would add mass back to the detector (or equivalent to suppressed LiF dissolution), assuming the dissolution rate remains higher than the precipitation rate. This assumption is valid as the continuous net decrease in LiF mass on the detector is observed during Stage 2. For simplicity, scenarios (1) and (2) are collectively referred to as “precipitation of LiF onto the QCM detector,” which is represented by the green regions in **Note S9 Figure 1b**. Meanwhile, regions in red in **Note S9 Figure 1b** indicate the reduced dissolution rate as LiF approaches saturation. After Stage 2, beyond the 14-minute mark, the dissolution/precipitation of LiF on the QCM detector stabilizes, reaching an equilibrium point. This stabilization is highlighted in blue in Stage 3 (**Note S9 Figure 1c**). Based on this analysis, the solubility of LiF in RE was approximately  $2.4 \mu\text{g mL}^{-1}$ , which equates to a concentration of 0.093 mM. This solubility was determined at the point where the dissolution levelled off at a plateau of around 14 minutes (indicated by the dashed red line in **Figure 3f**).

## Note S10 | LiF dissolution behavior in the LiF-saturated electrolyte



**Note S10 Figure 1.** Solubility profile of LiF in LiF SE measured by the QCM. The dissolution behaviour of LiF in LiF SE (a condition in which the electrolyte is already saturated by LiF) is represented by three distinct stages. (a), In Stage 1, LiF on the QCM detector is at equilibrium (in a cyclic process of spontaneous dissolution and precipitation of LiF) as the electrolyte is already saturated by LiF, highlighted by the blue region in the profile. (b), During Stage 2, while the spontaneous dissolution and reprecipitation of LiF on the QCM detector continue in LiF SE, LiF on the QCM detector tends to dissolve away and primarily precipitates outside the QCM detector area, as indicated by the purple regions in the profile. The regions marked in green signify the spontaneous reprecipitation of LiF onto the QCM detector. (c), In Stage 3, following the spontaneous dissolution of LiF on the QCM detector and its reprecipitation outside the QCM detector area in Stage 2, LiF reprecipitates accumulate on the QCM detector, as indicated by the orange region in the profile. Schematic illustrations corresponding to each stage provide a dynamic representation of the spontaneous dissolution and reprecipitation processes of LiF in LiF SE during the QCM measurement.

Further investigation into the dissolution/precipitation behavior of LiF in a saturated environment can provide valuable insights into its stability and arrangement characteristics in the SEI. To explore this, spontaneous dissolution-reprecipitation dynamics of LiF in LiF-saturated electrolyte (LiF SE) were examined using QCM at room temperature (**Figure 3g**). In this analysis, fluctuations in the solubility curve of LiF reflect corresponding changes in the mass of LiF on the QCM detector over time. The following cases explain the various mass changes under the dynamic equilibrium in LiF SE: (1) LiF on the QCM detector spontaneously dissolves and subsequently reprecipitates outside the detector area, leading to a net mass decrease of LiF on the QCM detector; (2) LiF on the QCM detector spontaneously dissolves and simultaneously reprecipitates back to the detector area, resulting in minimal net mass change of LiF on the QCM detector; and (3) LiF on the QCM detector and in LiF SE accumulating the reprecipitates onto the detector area, causing a net mass increase of LiF on the QCM detector. Considering these three cases, **Note S10 Figure 1** illustrates three stages of spontaneous dissolution-reprecipitation of LiF. In Stage 1, marked by the blue region in **Note S10 Figure 1a**, LiF maintains its dynamic equilibrium for approximately

2 minutes. In Stage 2 (**Note S10 Figure 1b**), which lasts from roughly 2 to 12 minutes, the mass of LiF on the QCM detector decreases, corresponding to case (1) (the purple regions in Stage 2), with intervals of slower rates, corresponding to case (2) (the green regions in Stage 2). This behavior arises due to a dynamic equilibrium of LiF dissolution-reprecipitation at its saturation, demonstrating that LiF dissolves (migrates away from its original position) and reprecipitates (deposits elsewhere). Such a process resembles Ostwald ripening, wherein smaller particles dissolve and redeposit onto larger particles to minimize overall surface energy. Given the variation in LiF particle sizes (**Figure S2**), the dynamic equilibrium of dissolution-reprecipitation rates may differ for individual LiF particles, with smaller particles dissolving more readily and redepositing onto larger ones (Ostwald ripening). Since the LiF suspension in LiF SE was pre-exposed to the electrolyte, the rate of spontaneous dissolution-reprecipitation can be higher for fresh LiF on the QCM detector (which had no prior electrolyte exposure) than for LiF in LiF SE (already equilibrated in the electrolyte), which contributes to the mass decrease of LiF on the QCM detector in Stage 2. In Stage 3, beyond the 12-minute mark, the mass of LiF on the QCM detector increases, corresponding to case (3) (the orange region in Stage 3), where the accumulation of reprecipitated LiF on QCM detector is detected (**Note S10 Figure 1c**). This analysis highlights that LiF can undergo spontaneous dissolution-reprecipitation at saturation (**Figure 3g**). Additionally, by comparing the slopes of the solubility curves in **Figure 3f** and **Figure 3g**, it is evident that saturating LiF in the electrolyte suppresses LiF dissolution rate. However, it is important to note that, despite this suppression, spontaneous dissolution-reprecipitation of LiF occurs in its saturated state.

### Note S11 | Relative solubility of LiF and Li<sub>2</sub>O in the electrolyte

Measurement at 25 °C	Conductance of 15 wt% LiF in EC:DEC (1:1 v/v) (μS)	Conductance of 15 wt% Li <sub>2</sub> O in EC:DEC (1:1 v/v) (μS)
1	23	9
2	23	11
3	23	11
4	24	11
5	24	11
Average	23.4	10.6
Standard Error	0.24	0.40
<b>Results</b>	<b>23.4 ± 0.24</b>	<b>10.6 ± 0.40</b>

**Note S11 Table 1.** Conductance values of 15 wt% LiF in EC:DEC (1:1 v/v) and 15 wt% Li<sub>2</sub>O in EC:DEC (1:1 v/v).

As SEIs are essentially the insoluble byproducts of decomposed electrolyte species with Li<sup>30,37,38,56</sup>, the solubility of LiF can influence its distribution within SEI. Regarding the driving force behind the dissolution of inorganic SEI species, Harris and coworkers have demonstrated that the solubility of lithium salts in EC and DMC follows the trend: LiF > (LiCO<sub>2</sub>)<sub>2</sub> > Li<sub>2</sub>CO<sub>3</sub> > Li<sub>2</sub>O, which aligns with their respective lattice energies<sup>40,41</sup>. This solubility trend can be indirectly validated by the frequent observation of Li<sub>2</sub>O and Li<sub>2</sub>CO<sub>3</sub>, but not as much for LiF, within the compact-SEIs (derived from liquid electrolytes) on Li<sup>0</sup> anodes<sup>57</sup>, where LiF is more profoundly observed, including Li<sub>2</sub>O and Li<sub>2</sub>CO<sub>3</sub>, in SEIs when using solid electrolytes<sup>58-61</sup> and at a low temperature<sup>29</sup>, in which such observations indicate the solubility of LiF in the electrolyte can impact its distribution.

Moreover, it is reported that the solubility of LiF varies considerably based on factors such as particle size, salts, and solvents<sup>25,62,63</sup>. The ability of a solvent to dissolve LiF is not determined solely by physicochemical properties but is also driven by entropy-related factors<sup>63</sup>. Although it is difficult to fully identify a universal driving force for the dissolution of inorganic SEI species, the electrolyte conductance can provide valuable insights supporting the dissolution of LiF and Li<sub>2</sub>O in the electrolyte solvents and to determine a relative solubility between LiF and Li<sub>2</sub>O. In **Note S11 Table 1**, the conductance of solutions containing 15 wt% LiF in EC:DEC (1:1 v/v) and 15 wt% Li<sub>2</sub>O in EC:DEC (1:1 v/v) was measured. The measured conductance values were 23.4 ± 0.24 μS and 10.6 ± 0.40 μS, respectively. Since conductance is related to the presence of free ions in solution, the trend observed in **Note S11 Table 1** provides the relative solubility of LiF and Li<sub>2</sub>O. The conductance of LiF in EC:DEC solvent system suggests that LiF can dissolve into the solvent, although the low conductance value reflects its limited solubility, but non-negligible, in the solvent. It should also be noted that the conductance of the blank EC:DEC solvent was beyond the detection limit of the instrument, indicating extremely low conductance for blank EC:DEC solvents. For Li<sub>2</sub>O in EC:DEC, the conductance was lower than that for LiF, signifying that Li<sub>2</sub>O is less soluble, though still able to dissolve to some extent. This confirms that Li<sub>2</sub>O can dissolve in the solvent but to a lesser degree compared to LiF. To summarize, the conductance measurements in **Note S11 Table 1** demonstrate that both LiF and Li<sub>2</sub>O are capable of dissolving into the solvent, with LiF showing a relatively higher solubility than Li<sub>2</sub>O.

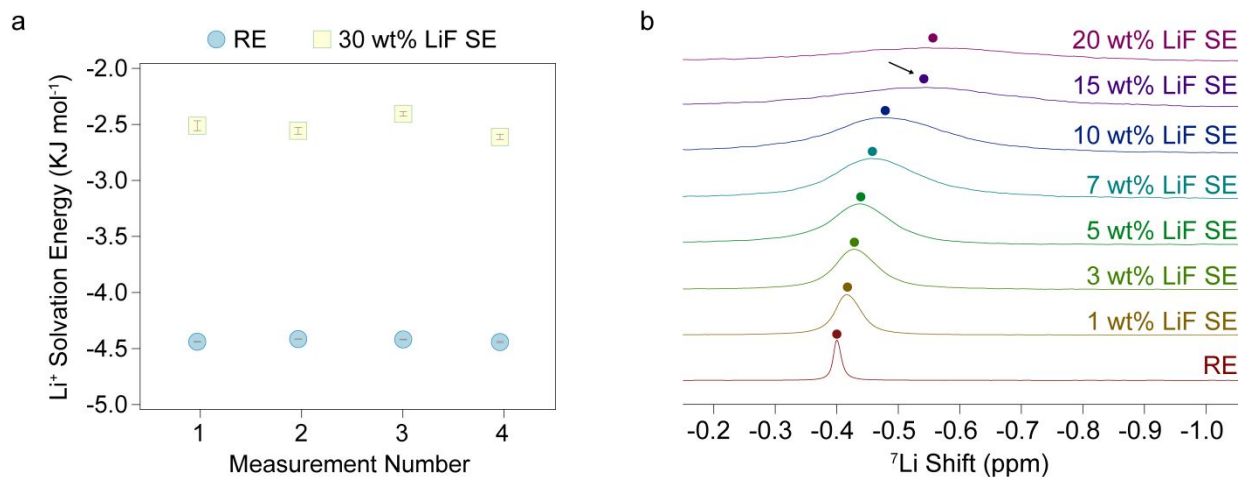
## Note S12 | Number density profile analysis

The number density profiles along the z-direction can be used to explore the molecular interactions of electrolyte species with LiF surfaces, as they represent the directional distributions for the average number of distinct electrolyte entities within the electrolyte volume. **Figure 4a** illustrates the number density profiles of RE. The electrolyte entities are presented as  $O_{EC}$  for EC solvent,  $O_{DEC}$  for DEC solvent,  $O_{FEC}$  for FEC solvent,  $F_{PF_6}$  for  $PF_6^-$  anion, and  $Li^+$  for cation. The number densities of each electrolyte species along the z-axis stay almost constant in **Figure 4a**, with the descending order of EC, DEC,  $PF_6^-$ , FEC, and then  $Li^+$  in the number densities. These profiles indicate that the electrolyte compounds are homogeneously mixed within RE, and the system is at equilibrium. As we introduce the LiF slabs, namely LiF (200), LiF (220)-Octo, and LiF (111)-Octo, in RE, some of the number density profiles tend to spike near LiF surfaces (**Figure 4b-d**). This behavior in the number density profiles close to LiF surfaces enables us to probe the surface interactions of electrolyte species with LiF. For example, **Figure 4b** shows that DEC and  $Li^+$  interact strongly with LiF (200), as they both exhibited a sharp increase in the number density in the vicinity of the LiF (220) surface. The following summarizes the interaction trends observed for specific LiF structures (from strong to weak): DEC,  $Li^+$ , then  $PF_6^-$  for LiF (200) (**Figure 4b**) & DEC, EC,  $Li^+$ , then  $PF_6^-$  for LiF (220)-Octo (**Figure 4c**) & DEC, EC, FEC,  $Li^+$ , then  $PF_6^-$  for LiF (111)-Octo-F (**Figure 4d**) & DEC, EC,  $Li^+$ ,  $PF_6^-$ , then FEC for LiF (111)-Octo-Li (**Figure 4d**). Importantly, we observed that the peak heights vary significantly with the specific surface textures of LiF. For instance, the solvents are more strongly attracted to the Li-terminated surface of LiF (111)-Octo compared to the F-terminated surface of the same slab. In general, we found that the solvents (especially DEC and EC) and  $Li^+$  tend to interact strongly at the surfaces of LiF in all cases.

### Note S13 | Surface adsorption of electrolyte species to LiF surfaces

The molecular interaction trends achieved from the number density profile analysis (**Figure 4a-d** and **Note S12**) are validated further by plotting the z-coordinate trajectories of electrolyte entities with respect to the simulation time (**Figure 4e-f**). The trajectories were plotted using colored dots to represent individual units present in the electrolyte. For example, one specific colored dot of  $O_{EC}$  (**Figure 4e**) represents one specific oxygen atom of EC molecule in RE within the simulation space. In this way, we can observe how each species in RE evolves during the course of MD simulations by simply tracking the colored dots. The trajectory profiles of  $O_{EC}$ ,  $O_{DEC}$ ,  $O_{FEC}$ ,  $P_{PF6^-}$ , and  $Li^+$  for RE exhibit homogeneous mixing behavior (**Figure S8a**). On the other hand, the line profiles of  $O_{DEC}$  and  $Li^+$  trajectories were observed near the surface of LiF (200) (**Figure 4e**). These line profiles, thus, indicate the surface adsorption of  $O_{DEC}$  and  $Li^+$  onto LiF (200) as these adsorbed units tend to stay at their adsorbed location throughout the simulation. This further means that  $O_{DEC}$  and  $Li^+$  were preferably interacting with the LiF (200) surface. In summary, linear profiles near LiF (200) (**Figure 4e**), LiF (220)-Octo (**Figure 4f**), LiF (111)-Octo-F (**Figure 4g**), and LiF (111)-Octo-Li (**Figure 4g**) were observed for  $O_{DEC}$  &  $Li^+$ ,  $O_{DEC}$  &  $O_{EC}$  &  $Li^+$ ,  $O_{DEC}$  &  $O_{EC}$  &  $O_{FEC}$  &  $Li^+$  &  $P_{PF6^-}$ , and  $O_{DEC}$  &  $O_{EC}$  &  $Li^+$  &  $P_{PF6^-}$  &  $O_{FEC}$ , respectively, which are in agreement with the trend observed from the number density profiles (**Figure 4a-d**). By analyzing the line profiles in the z-coordinate trajectory plots (**Figure 4h-j**), we are able to visually show that the electrolyte species (which were favorably interacting with LiF surfaces) were directly adsorbed onto the surfaces of LiF.

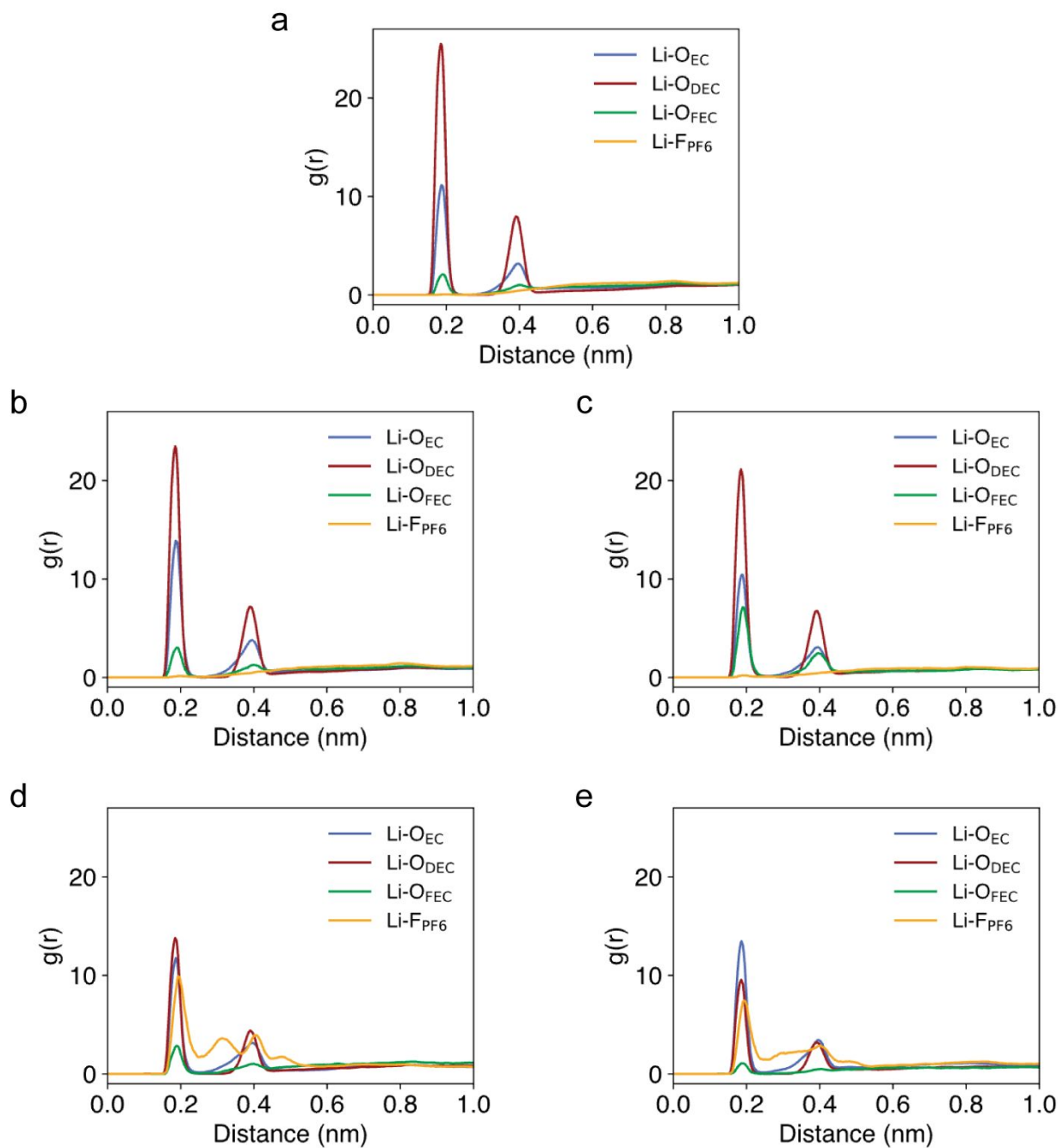
### Note S14 | Weakly solvating environment induced by LiF



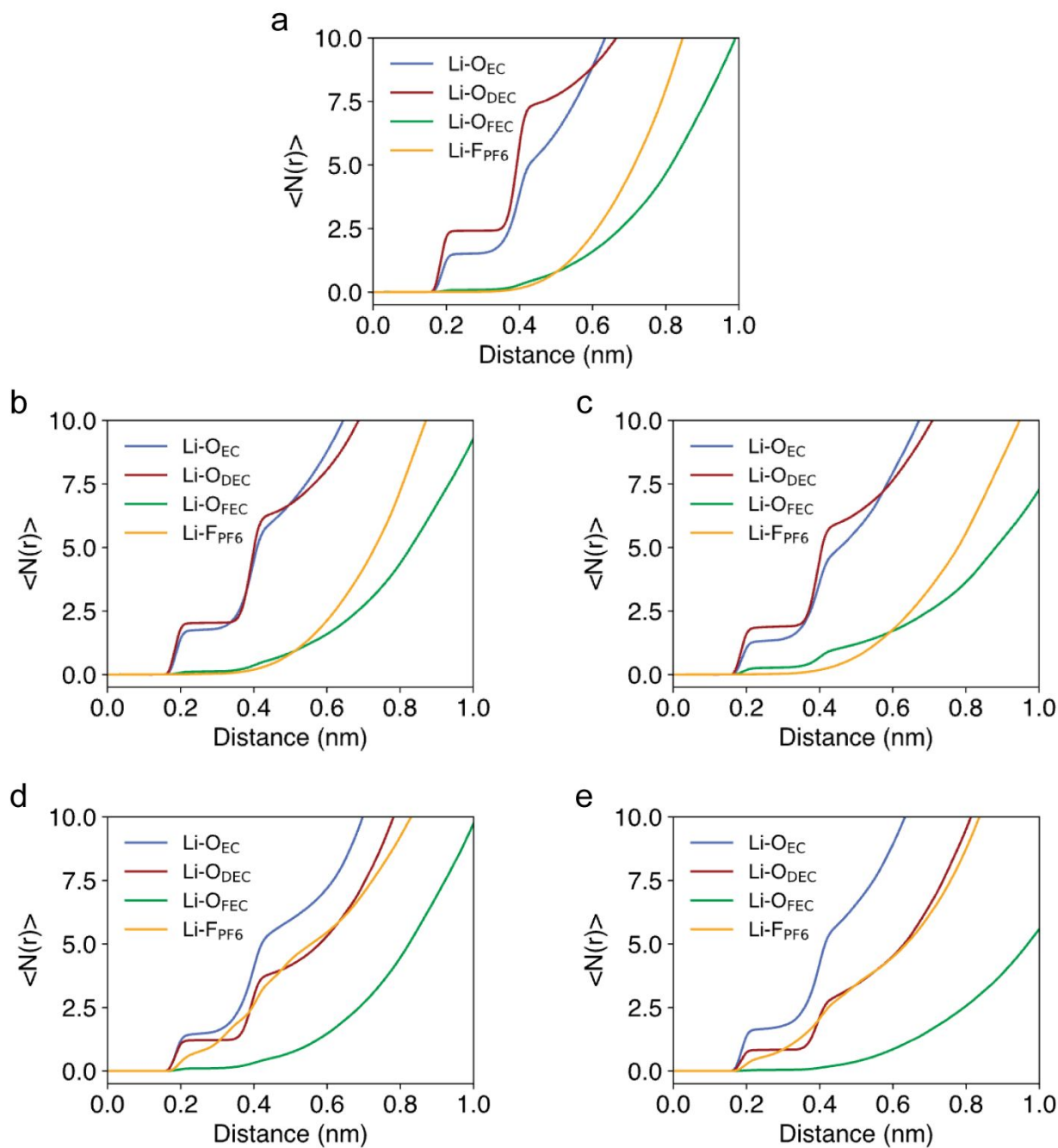
**Note S14 Figure 1.** (a) Electrolyte solvation energies of RE and 30 wt% LiF SE. (b) <sup>7</sup>Li NMR spectra of RE and 1~20 wt% LiF SE. The arrow indicates optimized LiF content in LiF SE.

LiF in EC:DEC (1:1 v/v)	Zeta potential (mV)
Measurement 1	39.81
Measurement 2	59.04
Measurement 3	39.84
Measurement 4	38.61
Measurement 5	40.69
Mean	43.60
Std	7.75
Error	3.47

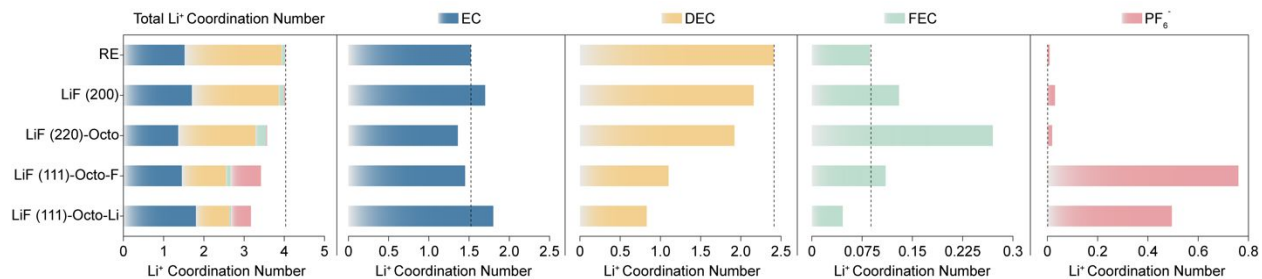
**Note S14 Table 1.** Five zeta potential measurements of LiF suspension in EC:DEC (1:1 v/v) solvent.



**Note S14 Figure 2.** RDFs of solvated  $\text{Li}^+$ . (a,b,c,d,e) The RDF profiles of  $\text{O}_{\text{EC}}$ ,  $\text{O}_{\text{DEC}}$ ,  $\text{O}_{\text{FEC}}$ , and  $\text{F}_{\text{PF6}^-}$  for RE (a), LiF (200) (b), LiF (220)-Octo (c), LiF (111)-Octo-F (d), LiF (111)-Octo-Li (e). The  $g(r)$  represents the radial distribution function, and the distance indicates the radial distance centered at the solvated  $\text{Li}^+$  in RE. For LiF surfaces, the radial distance was centered at the solvated  $\text{Li}^+$  near LiF surfaces within 1 nm away from the slab.



**Note S14 Figure 3.** CDF of solvated  $\text{Li}^+$ . (a,b,c,d,e) The CDF profiles of  $\text{O}_{\text{EC}}$ ,  $\text{O}_{\text{DEC}}$ ,  $\text{O}_{\text{FEC}}$ , and  $\text{F}_{\text{PF6}^-}$  for RE (a), LiF (200) (b), LiF (220)-Octo (c), LiF (111)-Octo-F (d), LiF (111)-Octo-Li (e). The  $\langle N(r) \rangle$  represents the cumulative distribution function, and the distance indicates the radial distance centred at solvated  $\text{Li}^+$  for RE. For LiF surfaces, the radial distance was centered at the solvated  $\text{Li}^+$  near LiF surfaces within 1 nm away from the slab.



**Note S14 Figure 4.**  $\text{Li}^+$  coordination number and solvation composition analysis. Total  $\text{Li}^+$  coordination numbers are plotted for RE, near the surfaces of LiF (200), LiF (220)-Octo, LiF (111)-Octo-F, and LiF (111)-Octo-Li. For each of the electrolyte species (EC, DEC, FEC, and  $\text{PF}_6^-$ ),  $\text{Li}^+$  coordination to the specified species is plotted for RE and LiF surfaces. The dotted vertical grey lines represent the  $\text{Li}^+$  coordination number of RE, serving as a reference value. The different colours in the total  $\text{Li}^+$  coordination number represent the fraction of distinct electrolyte species coordination of blue (EC), yellow (DEC), green (FEC), and red ( $\text{PF}_6^-$ ).

To empirically observe the surface interactions of LiF with electrolyte species in RE, namely its impact on the electrolyte solvation environment<sup>11,18</sup>, the solvation energies (**Note S14 Figure 1a**) and  $^7\text{Li}$  NMR (**Note S14 Figure 1b**) were measured for 30 wt% LiF SE and RE. In the solvation energy measurement, the high LiF content in LiF SE was deliberately chosen to effectively capture the relative solvation energy trend affected by LiF. In **Note S14 Figure 1a**, the solvation energies of 30 wt% LiF SE and RE were  $-2.52 \text{ KJ mol}^{-1}$  and  $-4.43 \text{ KJ mol}^{-1}$ , respectively, showing that LiF shifts the  $\text{Li}^+$  solvation environment of RE towards a more positive solvation energy. This means that LiF can reduce  $\text{Li}^+$ -solvent coordination and/or enhance anion coordination with  $\text{Li}^+$ , creating a weakly solvating environment<sup>11,16,18</sup>.

To cross-validate the solvation change and fine-tune LiF loading in LiF SE,  $^7\text{Li}$  NMR peaks were assessed for RE and 1 ~ 20 wt% LiF SE (**Note S14 Figure 1b**). Observing NMR peak shifts allows for a straightforward verification of the solvation environment change caused by LiF in RE<sup>11,18</sup>. This is because  $^7\text{Li}$  NMR measures the magnetic response of electron density around the solvated  $\text{Li}^+$  nuclei, in which the electron density fluctuates based on coordination numbers and types<sup>64</sup>. Rising LiF content in RE caused an upfield peak shift, reflecting an increase in the electron density of solvated  $\text{Li}^+$  and the modified solvation environment of RE. The peak shift trend points to 15 wt % as the optimal LiF content (rationalizing 15 wt % LiF used in this study), given the marginal peak shifts beyond 15 wt % LiF content. Although the broadening of the  $^7\text{Li}$  NMR peak occurred due to the magnetic disturbances from suspended LiF particles in RE, the symmetry of peak shapes confirmed true peak position shifts with various LiF contents. From NMR analysis, the upfield peak shifts suggest three possible cases for the influence of LiF on the solvation environment: (1) LiF promotes  $\text{Li}^+$  interaction with anion, (2) LiF surfaces interact directly with  $\text{Li}^+$ , and/or (3) LiF increases  $\text{Li}^+$ -solvent coordination. Given the weakly solvating environment of LiF SE (**Note S14 Figure 1a**), case (3) can be excluded, with cases (1) and (2) subject to further MD simulation analysis. Additionally, the zeta potential of LiF in EC:DEC (1:1 v/v) was measured to empirically determine the interaction of LiF with solvents and dispersity (**Note S14 Table 1**). Zeta potential is generally regarded as an important parameter for determining the stability of suspensions<sup>65</sup>. A high zeta potential, a magnitude larger than  $\pm 30 \text{ mV}$ <sup>66</sup>, typically results in greater repulsion among particles, leading to better dispersion and stability of the suspension system. Conversely, low or

zero zeta potential can lead to particle aggregation. The zeta potential of LiF was  $43.60 \pm 3.47$  mV (**Note S14 Table 1**), indicating a stable suspension<sup>66</sup>, which implies that LiF tends to interact favorably with solvent molecules. Accordingly, these analyses provide strong evidence that LiF interacts with electrolyte species, actively modifying the solvation environment through surface interactions of LiF with the electrolyte species.

Moreover, the MD simulations were conducted for RE and LiF SE (containing LiF (200), LiF (220)-Octo, and LiF (111)-Octo surfaces) to interrogate molecular interactions between the surfaces of LiF and the electrolyte species in RE. To construct reliable models for MD simulations, the exact composition of RE was implemented, where the structures of LiF (200), LiF (220)-Octo, and LiF (111)-Octo were constructed to assimilate LiF SE in MD simulations (**Figure S7**). The most important considerations in choosing LiF structures for MD simulation were rationally guided by the stability and empirical verification of the LiF structures (**Note S5**). The electrolyte species near the surfaces of LiF were systematically analyzed in the MD simulation to generate RDFs for RE (**Note S14 Figure 2a**), LiF (200) (**Note S14 Figure 2b**), LiF (220)-Octo (**Note S14 Figure 2c**), LiF (111)-Octo-F (**Note S14 Figure 2d**), LiF (111)-Octo-Li (**Note S14 Figure 2e**). Based on the profiles of coordinated species with  $\text{Li}^+$  ( $\text{Li-O}_{\text{EC}}$ ,  $\text{Li-O}_{\text{DEC}}$ ,  $\text{Li-O}_{\text{FEC}}$ , and  $\text{Li-F}_{\text{PF}_6}$ ) in RDFs, the approximate distance of the first  $\text{Li}^+$  solvation shell was determined by identifying the point where the first peak curve dissipates, in which 0.3 nm was chosen to be the right distance cut-off for the first solvation shell for RE, LiF (200), LiF (220)-Octo, LiF (111)-Octo-F, and LiF (111)-Octo-Li. Then, CDFs of RE (**Note S14 Figure 3a**), LiF (200) (**Note S14 Figure 3b**), LiF (220)-Octo (**Note S14 Figure 3c**), LiF (111)-Octo-F (**Note S14 Figure 3d**), LiF (111)-Octo-Li (**Note S14 Figure 3e**) were plotted to calculate the  $\text{Li}^+$  solvation composition close to the surfaces of LiF with the cut-off distance of 0.3 nm.

After performing statistical analysis, the total coordination number and compositions of the first  $\text{Li}^+$  solvation shell for RE, LiF (200), LiF (220)-Octo, LiF (111)-Octo-F, and LiF (111)-Octo-Li were obtained (**Note S14 Figure 4**). The total coordination number of solvated  $\text{Li}^+$  in all LiF structures was found to have decreased compared to RE (refer to the leftmost graph in **Note S14 Figure 4**). This directly confirms a weakly solvating environment of solvated  $\text{Li}^+$  induced by LiF in the electrolyte, which agrees with the solvation energy experiment in **Note S14 Figure 1a**. Furthermore, the solvated  $\text{Li}^+$  in RE and near LiF surfaces was primarily coordinated with EC (coordination number ranging from 1.4 to 1.7) and DEC (coordination number ranging from 0.8 to 2.5), whereas the FEC coordination was negligible ( $< 0.3$ ). The low coordination number for FEC is anticipated as FEC constitutes only 10 vol% of the total electrolyte species. Also, the higher coordination number of DEC compared to EC, despite EC being more polar, in the  $\text{Li}^+$  solvation shell results from the higher binding energy of DEC with  $\text{Li}^+$  than that of EC<sup>67</sup>. For  $\text{PF}_6^-$  coordination, there was a noticeable increase in the anion coordination number in the  $\text{Li}^+$  solvation shell for LiF (111)-Octo (increasing approximately from 0.1 to 0.7). The increase in the anion coordination to  $\text{Li}^+$  results in the upfield peak shift in  $^7\text{Li}$  NMR (**Note S14 Figure 1b**) as the anion holds a negative charge in the solvation shell<sup>11</sup>. Also, DEC coordination in the  $\text{Li}^+$  solvation shell was substantially decreased for LiF when compared to RE, displaying a more pronounced difference in comparison to the trend observed for EC coordination number. These findings corroborate (1) the weakly solvating environment of LiF SE in **Note S14 Figure 1a** (due to the decrease in the total  $\text{Li}^+$  coordination number) and (2) the upfield peak shift in  $^7\text{Li}$  NMR in **Note S14 Figure 1b** (due to the increase in  $\text{Li}^+$ - $\text{PF}_6^-$  coordination).

### Note S15 | CE and Li nucleation overpotential analysis

The CE measurements<sup>17</sup> were performed to assess the electrochemical performances of Li<sup>0</sup> electrode with RE and LiF SE. From Li<sup>0</sup>|Cu half cells, the CE measurement protocol involves four stages: (1) one activation cycle of plating and stripping 5 mAh cm<sup>-2</sup> amount of Li<sup>0</sup> at 1 mA cm<sup>-2</sup>, (2) subsequently plating 5 mAh cm<sup>-2</sup> amount of Li<sup>0</sup> at 1 mA cm<sup>-2</sup>, (3) partially stripping and redepositing 1 mAh cm<sup>-2</sup> amount of Li<sup>0</sup> at 1 mA cm<sup>-2</sup> for 9 cycles, and (4) fully stripping remainder of electrodeposited Li<sup>0</sup> on Cu at 1 mA cm<sup>-2</sup>. The current density of 1 mA cm<sup>-2</sup> was selected to be consistent with the sample preparation conditions outlined in **Figure 1** and **Figure 2**. Using this protocol, CE represents the percentage of active Li<sup>0</sup> that is successfully retrieved after undergoing multiple cycles of Li plating and stripping processes. The decrease in CE is typically caused by two main factors: forming electrically disconnected Li<sup>0</sup> (often referred to as “dead Li”) and consuming active Li<sup>0</sup> by side-reacting with electrolyte species to form SEIs on Li<sup>0</sup> electrodeposits<sup>68</sup>. Given that RE and LiF SE employ identical liquid electrolyte chemistry, the difference in the CE values primarily results from the presence of LiF in RE.

In **Figure S11**, the CE of LiF SE (97.30 % ± 0.21 %) was about 4 % higher than that of RE (93.35 % ± 2.15 %), demonstrating LiF enhanced the electrochemical reversibility of Li<sup>0</sup> electrode. Generally, the key factors influencing CE are closely associated with the topography of Li<sup>0</sup> electrodeposits and the characteristics of SEIs<sup>69</sup>, in which low surface area Li<sup>0</sup> electrodeposition and inorganic-rich interphases are much desired for Li<sup>0</sup> anodes. While LiF contributed to the improvement in CE, the overall CE value remained relatively limited due to the SEI composition being primarily influenced by the carbonate-based electrolyte chemistry of RE. From the CE measurement, Li nucleation overpotential was calculated from the activation cycle at which the Li<sup>0</sup> is first deposited on Cu in Li<sup>0</sup>|Cu cells<sup>11,18</sup>. A low Li nucleation overpotential is often preferred for achieving compact Li<sup>0</sup> electrodeposition morphologies<sup>19,20,70–72</sup> that often positively correlate with CE<sup>11,18</sup>. Observing Li nucleation overpotential values, thus, became a convenient approach to predicting the topology of Li<sup>0</sup> electrodeposits. Intriguingly, it was found that LiF SE (77.53 mV ± 4.79 mV vs. Li<sup>+</sup>/Li) did not change the nucleation overpotential relative to that of RE (76.57 mV ± 1.12 mV vs. Li<sup>+</sup>/Li). This result was surprising as improved CE is frequently coupled with a reduction in the nucleation overpotential. As anticipated, the Li<sup>0</sup> electrodeposition morphology with RE and LiF SE was comparable to each other (**Figure S12**). This result leads to an important hypothesis that LiF tends to play a part after involving electrochemical cycles of Li<sup>0</sup> plating and stripping in the cells. Because Li<sub>2</sub>O can only be formed by the electrolyte decomposition<sup>30</sup> (meaning Li<sub>2</sub>O is absent prior to electrochemical cycling), LiF exhibits a weak impact on the early stage of Li<sup>0</sup> plating process, as the SEI species must be generated and saturated first to construct stable SEI precipitates onto the Li<sup>0</sup> electrodeposits. Since the electrodeposited Li<sup>0</sup> with LiF SE showed Li<sub>2</sub>O-rich and enhanced distribution of Li<sub>2</sub>O across the SEI than that with RE (**Figure 1b-e** and **Note S4**), the effect of LiF on the electrochemical cycling characteristics should be more pronounced in the subsequent cycles or after the completion of the first Li<sup>0</sup> plating phase. This claim is further supported by the increased first cycle and overall CE for LiF SE (**Figure S11b,c**). Together, these results support that LiF tends to play a role when Li<sub>2</sub>O is generated, in which the process necessitates electrochemical cycling to produce Li<sub>2</sub>O through the electrolyte decomposition<sup>30</sup>.

## Note S16 | Analysis of pristine Li<sup>0</sup> electrode with RE and LiF SE

The interphase characteristics of pristine (uncycled) Li<sup>0</sup> electrode were systematically investigated by electrochemical impedance spectroscopy and XPS (**Figure S13-15** and **Table S1-8**). The spontaneous formation of such interphases on Li<sup>0</sup> electrodes results from both chemical and electrochemical side reactions occurring at the Li<sup>0</sup>/electrolyte interface<sup>38</sup>. Due to the high reactivity of Li<sup>0</sup>, the chemical decompositions of electrolyte species should be initiated first, prior to the electrochemical decomposition. Upon electrolyte contact, Li<sup>0</sup> electrode undergoes a corrosion process that leads to the formation of chemically derived SEIs, which causes a gradual increase in the interfacial impedances of Li<sup>0</sup> over time<sup>27</sup>. This corrosion process of Li<sup>0</sup> is exacerbated by electrolyte penetration induced by the SEI swelling<sup>21</sup>. Considering the time-dependent ageing process of Li<sup>0</sup>, it has become critical to observe the temporal characteristics of the interphases formed with a specific electrolyte<sup>11,18</sup> on Li<sup>0</sup>. Leveraging this phenomenon allows for a succinct analysis of the interphase characteristics and chemical evolution occurring at the interface between pristine Li<sup>0</sup> and the electrolyte, which can be probed from Li<sup>0</sup>|Li<sup>0</sup> symmetric cells<sup>11,18</sup>.

The interfacial impedances of Li<sup>0</sup>|Li<sup>0</sup> cells containing RE and LiF SE were assessed before ( $t_{\text{rest}} = 0$  hr) and after ( $t_{\text{rest}} = 24$  hr) ageing the cells in an open circuit for a day (**Figure S13a-c** and **Figure S14**). Using this approach, we can anticipate a chemical evolution of the interphase influenced by LiF on the pristine Li<sup>0</sup> electrode. LiF SE ( $206.03 \Omega \pm 2.20 \Omega$  at  $t_{\text{rest}} = 0$  hr and  $424.47 \Omega \pm 3.64 \Omega$  at  $t_{\text{rest}} = 24$  hr) exhibited remarkably similar interfacial impedance trends to those of RE ( $199.64 \Omega \pm 3.73 \Omega$  at  $t_{\text{rest}} = 0$  hr and  $421.24 \Omega \pm 1.33 \Omega$  at  $t_{\text{rest}} = 24$  hr), demonstrating that LiF had a negligible impact on the chemical evolution of the interphase for pristine Li<sup>0</sup> electrodes (**Figure S13a**). To extrapolate chemical information, anion-to-solvent decomposition metrics of P/C (**Figure S13b**) and P/O (**Figure S13c**) ratios were measured on Li<sup>0</sup> electrodes with RE and LiF SE under the same conditions in **Figure S13a** *via* XPS (**Table S1-4**). The ratios of the P/C and P/O provide valuable insights into the relative decomposition ratio between the anion and solvents of RE and LiF SE. The reason behind this is that the anion exclusively contains element P, while the solvents consist of elements of C and O (See the inset of **Figure S13b**). Despite the P/C ratio of LiF SE being slightly higher than that of RE, the P/C ratio before and after the ageing of the symmetric cells was comparable to each other (**Figure S13b**). Likewise, the P/O ratio of LiF SE was comparable to that of RE, and the trend remained the same (**Figure S13c**). The marginal increase in P/C and P/O ratios (indicating enhanced anion decomposition) for LiF SE during the chemical aging of pristine Li<sup>0</sup> electrodes can be attributed to the modified solvation environment induced by LiF, in which LiF increases Li<sup>+</sup>-anion and reduces Li<sup>+</sup>-solvent coordination within the first solvation shell, thereby promoting anion decomposition while suppressing solvent decomposition (**Note S14**). With this solvation environment change induced by LiF, the trend in the lowest unoccupied molecular orbital energies (reflecting the reduction stability of electrolyte species<sup>73</sup>) for PF<sub>6</sub><sup>-</sup>, FEC, EC, and DEC (ranked from least (PF<sub>6</sub><sup>-</sup>) to most stable (DEC) in terms of reduction<sup>74</sup>) further supports the observed increase in anion and decrease in solvent decomposition on the pristine Li<sup>0</sup> electrode.

### Note S17 | Analysis of electrodeposited Li<sup>0</sup> with RE and LiF SE

The interphase characteristics of electrodeposited Li<sup>0</sup> were explored from Li<sup>0</sup>|Cu cells with RE and LiF SE. This analysis involved measuring the interfacial impedances before and after plating 1 mAh cm<sup>-2</sup> amount of Li<sup>0</sup> at 1 mA cm<sup>-2</sup> on Cu and subsequently ageing the electrodeposited Li<sup>0</sup> in an open circuit for 24 hours (**Figure S13d** and **Figure S15**). Interfacial impedances of pristine Li<sup>0</sup>|Cu cells ( $t_{\text{rest}} = 0$  hr Before Li<sup>0</sup> plating) with RE and LiF SE were first measured to cross-validate the Li<sup>0</sup> symmetric cell impedance values at  $t_{\text{rest}} = 0$  hr, shown in **Figure S13a**. Almost equivalent values were achieved in both Li<sup>0</sup>|Cu and Li<sup>0</sup>|Li<sup>0</sup> cells, confirming that the interfacial characteristic was consistent in the context of chemical evolution on the pristine Li<sup>0</sup> electrode. Since we claim that LiF starts to play a role with Li<sub>2</sub>O (after involving the electrochemical cycle), the interfacial impedances were probed from Li<sup>0</sup>|Cu cells right after ( $t_{\text{rest}} = 0$  hr) electrodepositing 1 mAh cm<sup>-2</sup> Li<sup>0</sup> on Cu at 1 mA cm<sup>-2</sup> with RE and LiF SE (**Figure S13d**). The corresponding interfacial impedances for electrodeposited Li<sup>0</sup> with RE and LiF SE were  $47.48 \Omega \pm 1.20 \Omega$  and  $36.53 \Omega \pm 0.31 \Omega$ , in which RE and LiF SE showed 73% and 83% decrease in the interfacial impedance, respectively. The decrease in the interfacial impedance values after the electrodeposition of Li<sup>0</sup> on Cu is attributed to the increased surface area of the electrodeposits as observed in **Figure S12**. However, the magnitude of the interfacial impedance change in RE and LiF SE was comparable to each other for  $t_{\text{rest}} = 0$  hr After Li<sup>0</sup> plating.

To further explore the effect of LiF in the interphase of electrodeposited Li<sup>0</sup>, the interfacial impedances of aged ( $t_{\text{rest}} = 24$  hr) electrodeposited Li<sup>0</sup> were measured for RE ( $71.07 \Omega \pm 1.08 \Omega$ ) and LiF SE ( $40.34 \Omega \pm 0.71 \Omega$ ). Notably, the increased interfacial impedance after ageing the electrodeposited Li<sup>0</sup> with LiF SE was significantly lower (10%), whereas RE exhibited 50% increase in the impedance after ageing. This signifies that LiF contributed to preserving the interphase chemistry of electrodeposited Li<sup>0</sup>. To identify further evidence, the P/C (**Figure S13e**) and P/O (**Figure S13f**) ratios were measured to closely examine the SEI maintenance of electrodeposited Li<sup>0</sup> with RE and LiF SE during the ageing process (**Table S5-8**). Crucially, by comparing the P/C and P/O ratios of RE and LiF SE before and after ageing, both ratios were well maintained for LiF SE upon ageing, whereas RE showed in noticeable decrease in the ratios, which is in line with the interfacial impedance analysis in **Figure S13d**. As we attribute the roles of LiF in enriching and distributing Li<sub>2</sub>O within the interphase of electrodeposited Li<sup>0</sup> (**Figure 1d,e** and **Note S4**), the improved interphase passivity afforded by LiF closely aligns with the Li<sub>2</sub>O-rich interphase characteristics, where Li<sub>2</sub>O is identified to exhibit excellent interphase passivity on Li<sup>0</sup> anode<sup>11</sup>. For RE, however, both P/C and P/O ratios were decreased substantially relative to those of LiF SE. The decreased P/C and P/O ratios signify that the interphase on electrodeposited Li<sup>0</sup> with RE continued to extend by the corrosion process driven by the electrolyte penetration through the SEI. Taken together, these electrochemical responses suggest that LiF begins to influence the interphase passivity of Li<sup>0</sup> after involving the electrochemical process (contingent upon forming Li<sub>2</sub>O), as evidenced by **Figure S13-15**. Based on the analysis, we discerned that LiF (1) helped to chemically stabilize the interphase formed on electrodeposited Li<sup>0</sup>, (2) inhibited corrosion of electrodeposited Li<sup>0</sup>, and (3) provided an effective passivating agent of Li<sub>2</sub>O across the interphase of electrodeposited Li<sup>0</sup>, in which the beneficial attributes of LiF are afforded by the Li<sub>2</sub>O-richer<sup>11,75,76</sup> and well-distributed LiF/Li<sub>2</sub>O indirect-SEI (**Figure 1d,e** and **Figure 2e-k**).

## Note S18 | Valuable insights

In an ending remark, our findings clarify the uncertainties surrounding the roles of LiF<sup>30,37</sup> (**Figure 1a**) and offer valuable insights that could aid in the development of electrolytes and interphases for Li<sup>0</sup> anodes. First, considering electrolyte chemistries, operating conditions, and additives that can inhibit the dissolution/precipitation of LiF, but not limited to LiF, would be of great interest to physicochemically stabilize SEIs on Li<sup>0</sup> anodes. Furthermore, advancing suspension electrolyte designs *via* optimizing suspension loading, nanostructures, dispersity, and others would be another important step forward in reinforcing SEIs. Second, conducting focused studies to explore the dissolution/precipitation behavior of SEI constituents in electrolytes could aid in deciphering the spatial distribution of individual SEI compounds within SEIs and the SEI stabilities on Li<sup>0</sup> anodes. We note that investigating the anode-cathode and/or anode-separator crosstalk, especially potential shuttling inorganic SEI species, would be an essential prospective study. Third, analyzing nanostructures and speciation of developed SEIs (rSEIs that are undergone several cycles of electrochemical reactions) in probing synergy among SEI species would be a crucial SEI study. Last, exploring electrolyte formulations that can promote optimal length scales and distribution of indirect-SEIs, such as LiF/Li<sub>2</sub>O, would be a path to consider for improving the overall passivity of Li<sup>0</sup> anodes.

## SUPPORTING FIGURES



**Figure S1.** Photographs of RE and LiF SE taken after resting the electrolytes for a day. LiF SE exhibits an opaque solution.

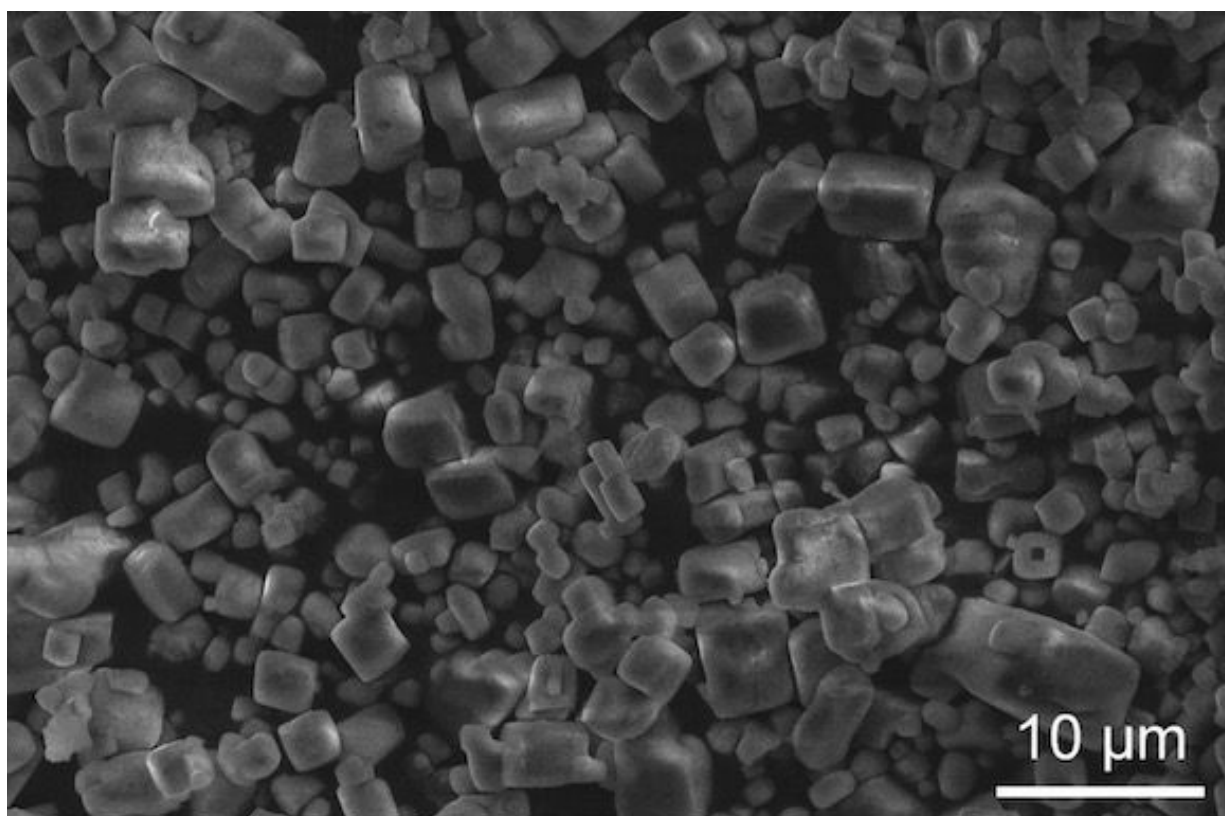


**Figure S2.** The SEM image of LiF suspension. Particle sizes of LiF range from 400 nm to 5 μm.

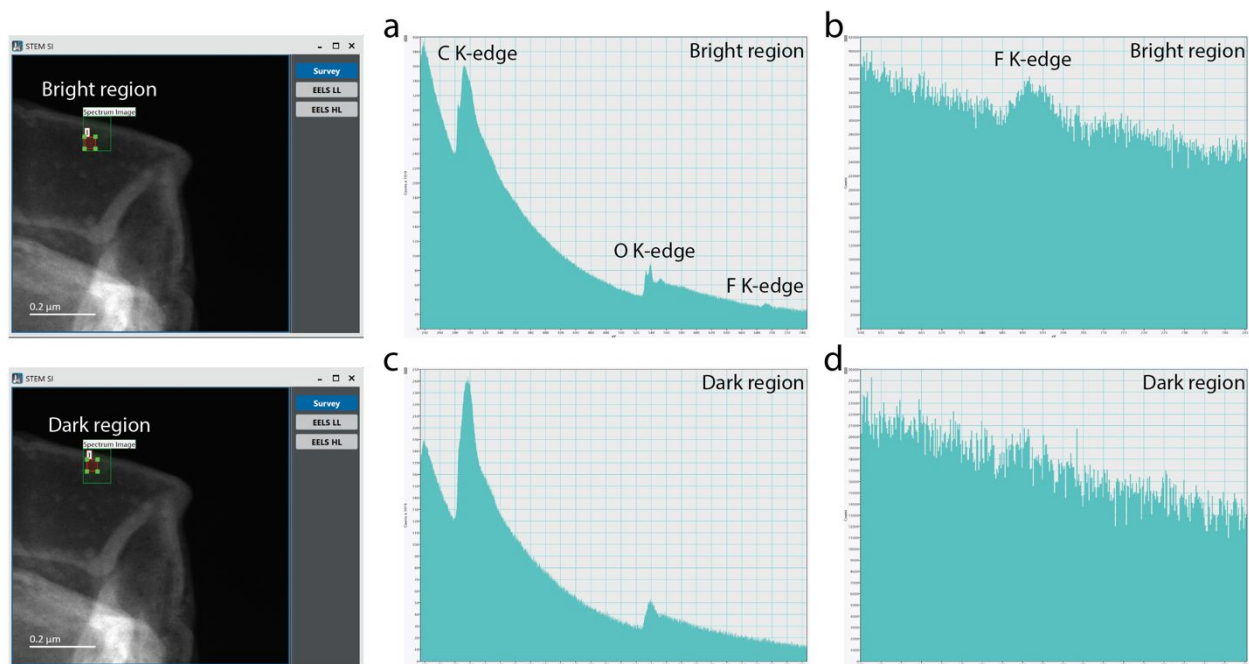


**Figure S3.** Cryo-STEM EELS data for the bright and dark regions in Figure 2m. (a) Cryo-STEM EELS signals for the bright region in Figure 2m. The y-axis ranges from 0 to  $400 \times 10^3$  counts, and the x-axis (eV) ranges from 240 to 750 eV. (b) the F K-edge fine structure for the bright region in Figure 2m. The y-axis ranges from 0 to 42000 counts, and the x-axis (eV) ranges from 650 to 750 eV. (c) Cryo-STEM EELS signals for the dark region in Figure 2m. The y-axis ranges from 0 to  $250 \times 10^3$  counts, and the x-axis (eV) ranges from 240 to 750 eV. (d) The F K-edge fine structure for the dark region in Figure 2m. The y-axis ranges from 0 to 26000 counts, and the x-axis (eV) ranges from 650 to 750 eV.



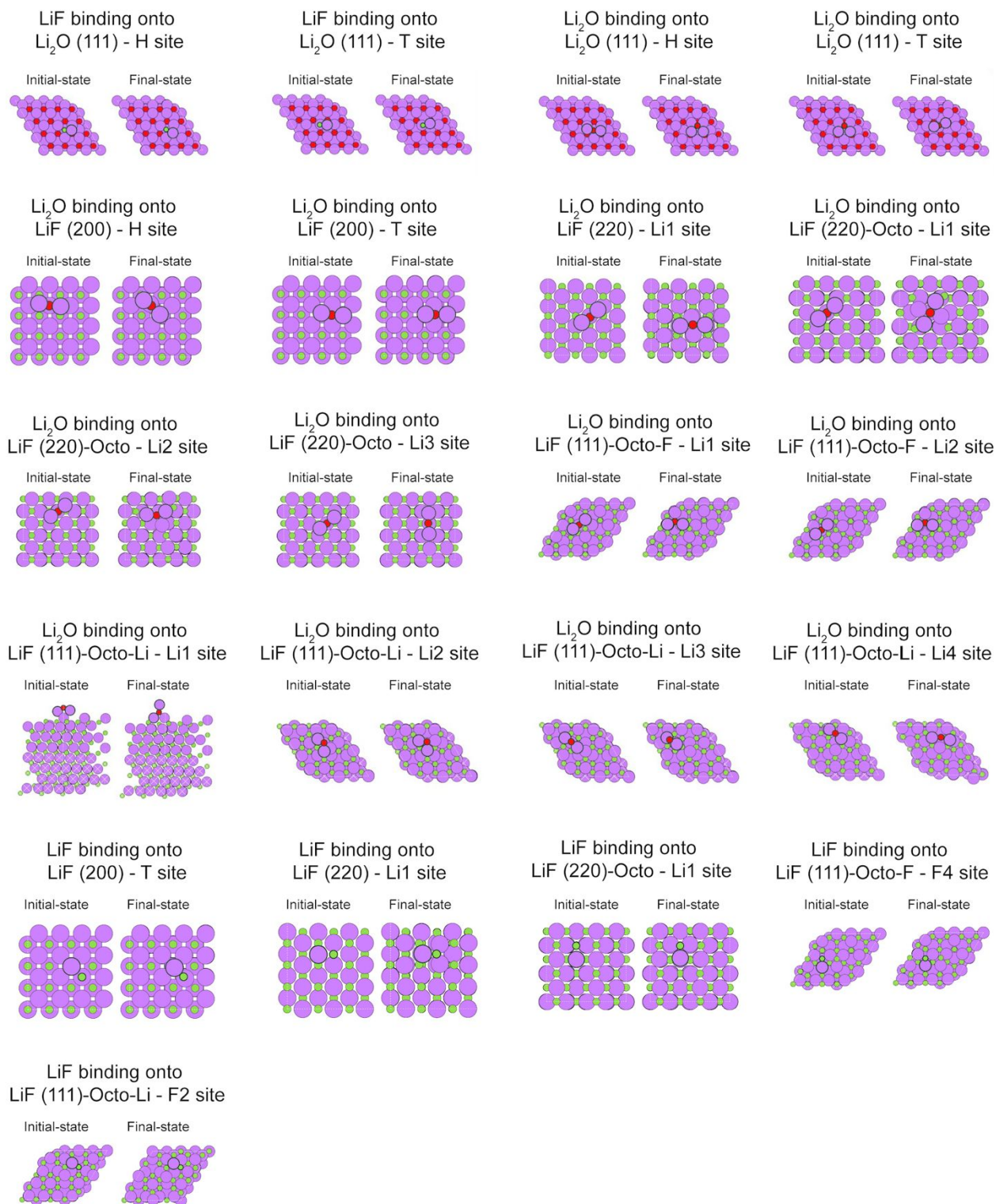


**Figure S5.** Molecular structures and binding sites for LiF and Li<sub>2</sub>O molecules binding onto the Li<sub>2</sub>O (111) and LiF surfaces. The images illustrate specific molecules, either LiF or Li<sub>2</sub>O (indicated by the black lined borders), binding onto the specified sites on the Li<sub>2</sub>O and LiF surfaces. The initial and final binding states of LiF and Li<sub>2</sub>O are shown for each binding site and structure. The colour codes for Li, O, and F are purple, red, and green, respectively.

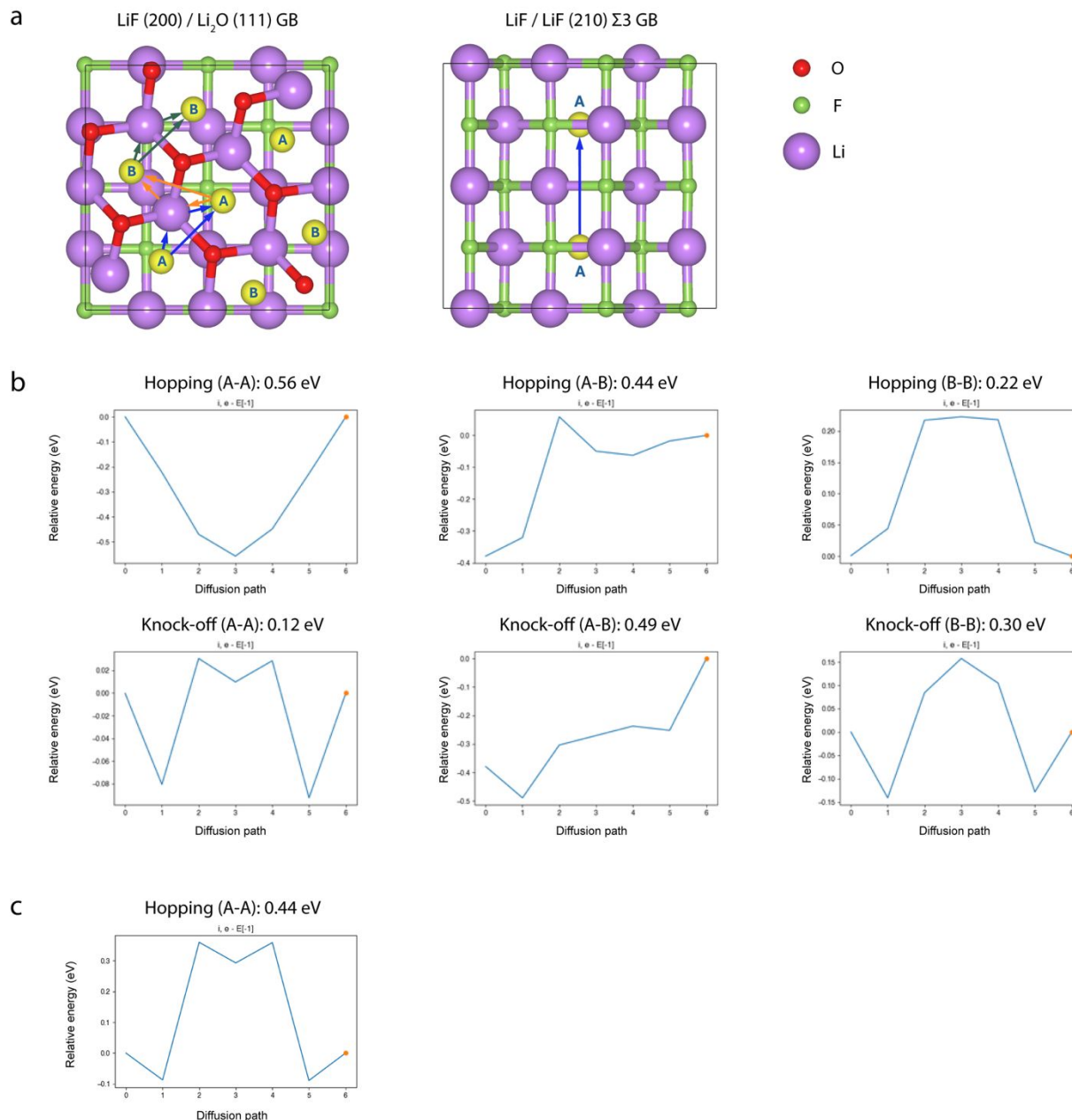


**Figure S6.** LiF/Li<sub>2</sub>O and LiF/LiF grain boundaries (GB) structures and activation energy profiles for Li diffusion. (a) Cross-section structures of a LiF (200) / Li<sub>2</sub>O (111) GB and a LiF / LiF (210) Σ3 GB near the grain centers. Red, green, and purple spheres denote O, F, and Li atoms, respectively; yellow spheres denote high symmetry sites inside the grain boundaries. Colored arrows represent the diffusion pathways (hopping and knock-off). (b) Energy profiles of Li diffusion through the LiF (200) / Li<sub>2</sub>O (111) GB in (a). (c) Energy profile of Li diffusion through the LiF (210) Σ3 GB in (a).

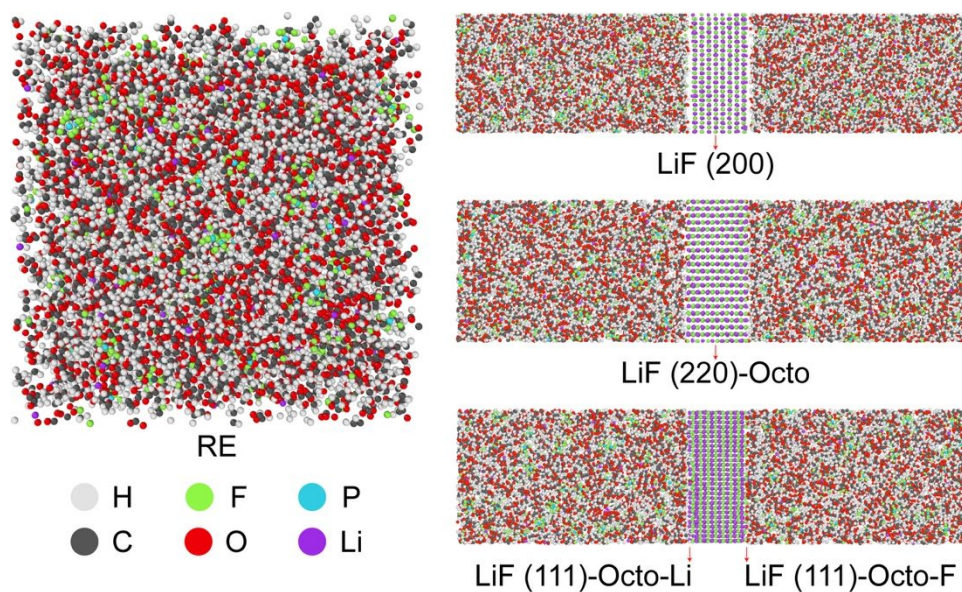


**Figure S7.** Representative snapshots of MD simulation for RE, LiF (200), LiF (220)-Octo, LiF (111)-Octo-Li, and LiF (111)-Octo-F analyses. The colour codes for the atoms of the electrolyte species are grey (H), green (F), blue (P), black (C), red (O), and purple (Li).

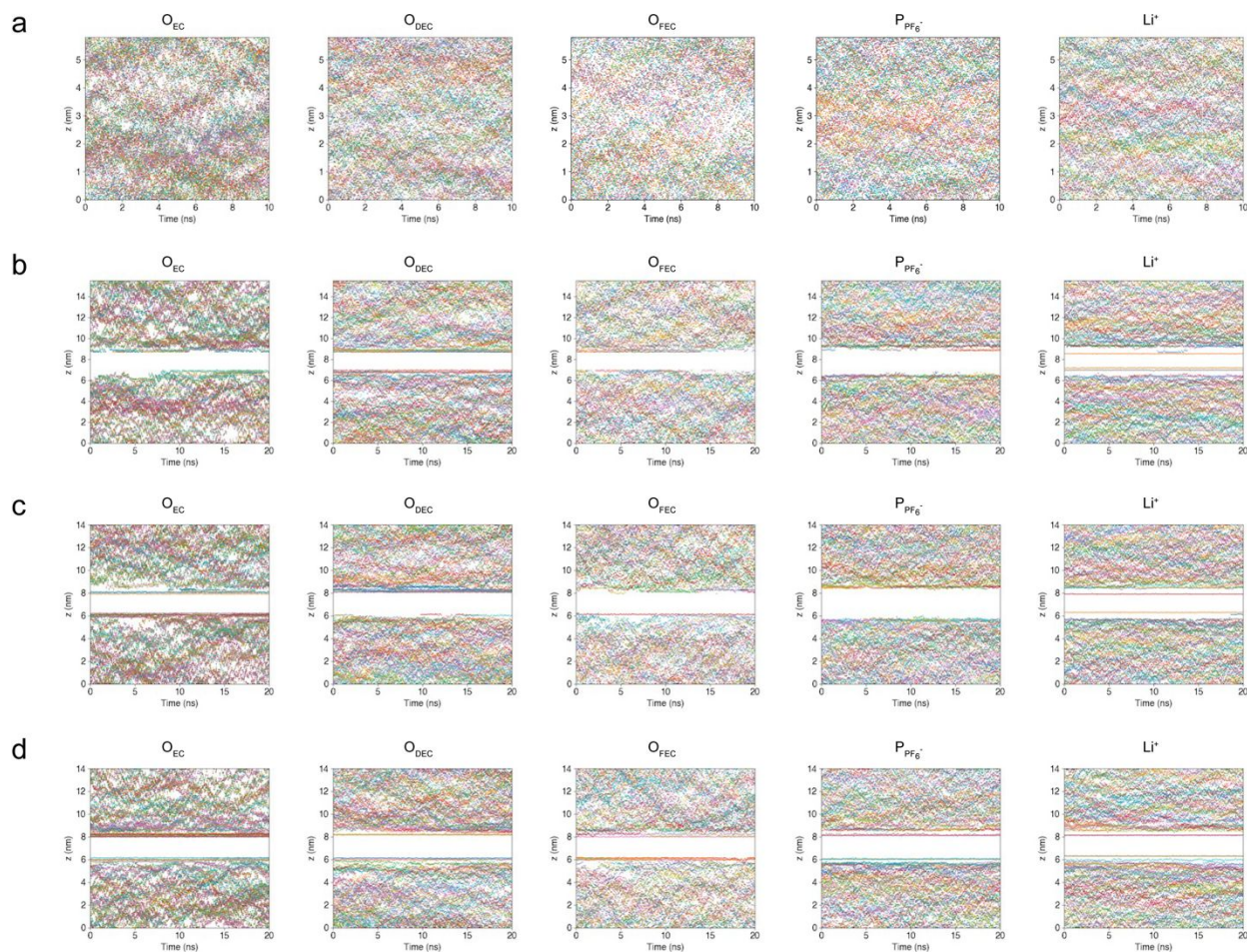


**Figure S8.** Trajectory profiles of electrolyte species for RE. (a,b,c,d)  $O_{EC}$ ,  $O_{DEC}$ ,  $O_{FEC}$ ,  $P_{PF_6^-}$ , and  $Li^+$  trajectories of RE (a), LiF (200) (b), LiF (220)-Octo (c), and LiF (111)-Octo-F & LiF (111)-Octo-Li (d) retrieved from MD simulation. Each coloured dot represents individual electrolyte species of EC, DEC, FEC,  $PF_6^-$ , and  $Li^+$  in MD simulation. The constant colour line profiles indicate surface adsorption and strong surface interaction of specified electrolyte species with corresponding LiF structures. The y-axis of the plots illustrates the z-axis (height in nm) in the simulation box, whereas the x-axis shows the conducted simulation time in ns.

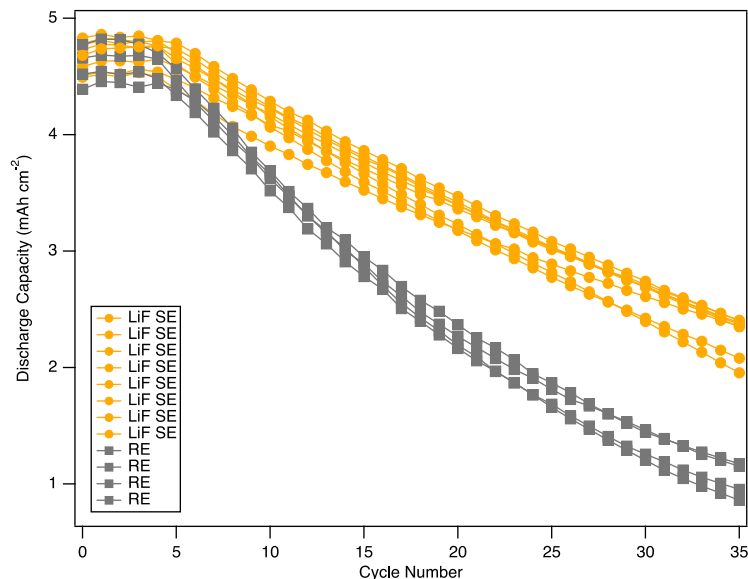


**Figure S9.** Anode-less cell cycling analysis. Cu|NMC811 anode-less cell cycling performances with RE and LiF SE. The Cu|NMC811 cells were charged up to 4.2 V vs. Li<sup>+</sup>/Li with a current density of 0.4 mA cm<sup>-2</sup>, and constant voltage charging was applied at 4.3 V vs. Li<sup>+</sup>/Li with a cut-off current of 0.04 mA cm<sup>-2</sup>. Then, the cells were galvanostatically discharged from 4.3 V to 3 V vs. Li<sup>+</sup>/Li with a current density of 0.8 mA cm<sup>-2</sup>.

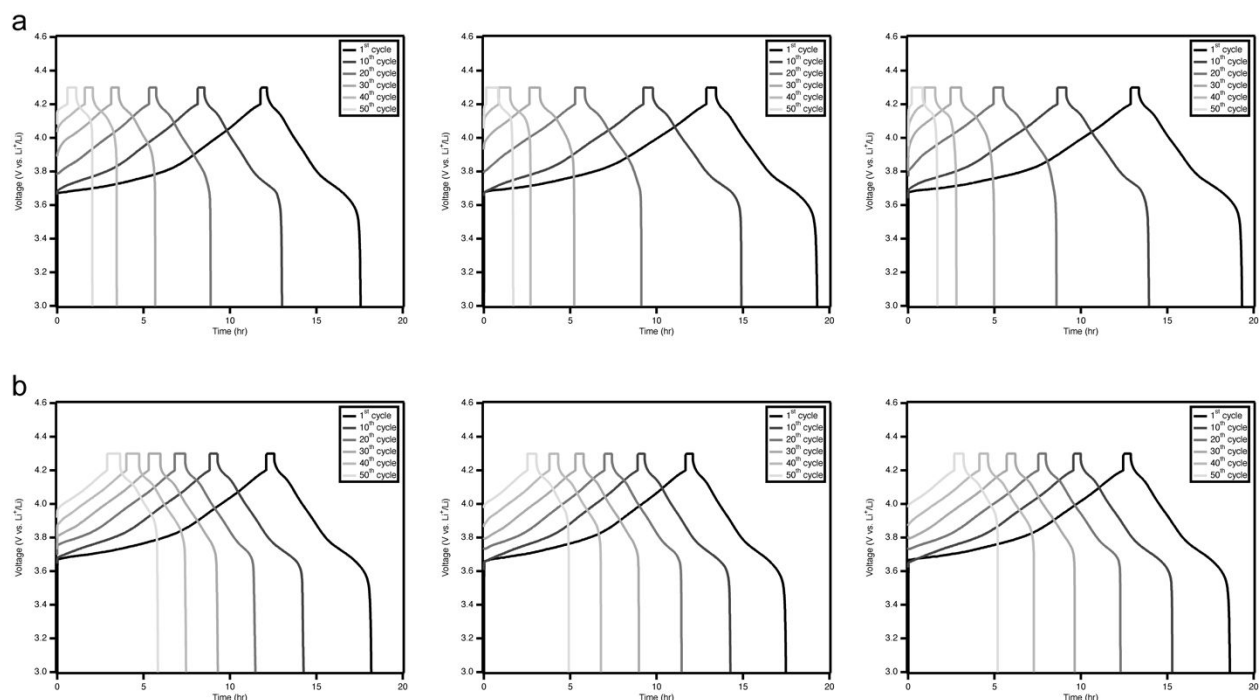


**Figure S10.** Voltage profiles of three identical anode-free Cu|NMC811 cells with RE and LiF SE. (a,b) The voltage profiles include 1<sup>st</sup>, 10<sup>th</sup>, 20<sup>th</sup>, 30<sup>th</sup>, 40<sup>th</sup>, and 50<sup>th</sup> cycles of the three identical anode-free Cu|NMC811 cell with RE (a) and LiF SE (b). The anode-free cells were charged at the constant current density of 0.4 mA cm<sup>-2</sup> up to 4.2 V vs. Li<sup>+</sup>/Li with the constant voltage charging at 4.3 V vs. Li<sup>+</sup>/Li using the cut-off current value of 0.04 mA cm<sup>-2</sup>. Then, the cells were galvanostatically discharged at the constant current density of 0.8 mA cm<sup>-2</sup> to 3 V vs. Li<sup>+</sup>/Li.

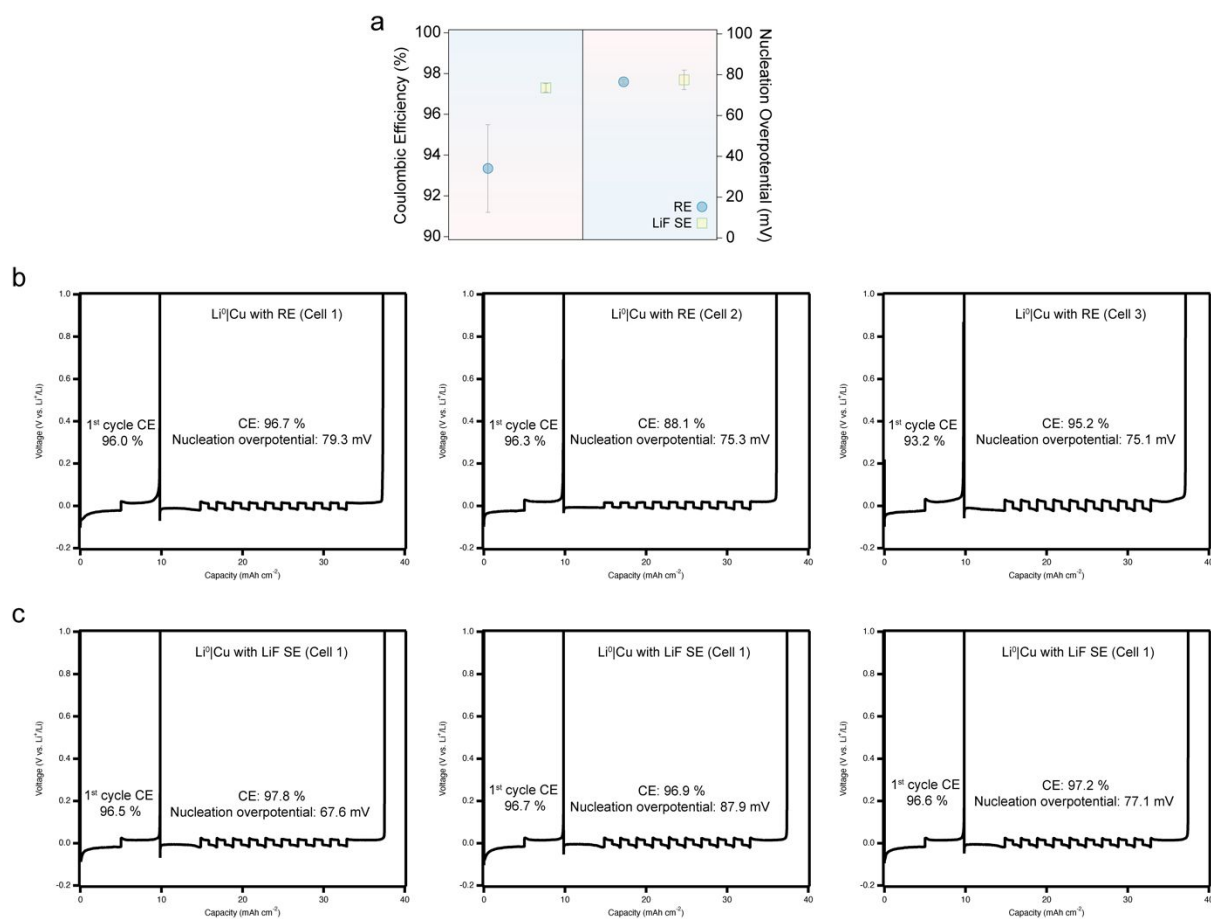


**Figure S11.**  $\text{Li}^0$  anode CE and nucleation overpotential analysis. (a) The average CE and nucleation overpotential values obtained from  $\text{Li}^0\text{Cu}$  cells with RE ( $93.35\% \pm 2.15\%$  and  $76.57\text{ mV} \pm 1.12\text{ mV}$  vs.  $\text{Li}^+/\text{Li}$ ) and LiF SE ( $97.30\% \pm 0.21\%$  and  $77.53\text{ mV} \pm 4.79\text{ mV}$  vs.  $\text{Li}^+/\text{Li}$ ). The current density of  $1\text{ mA cm}^{-2}$  and voltage cut-off at  $1\text{ V}$  vs.  $\text{Li}^+/\text{Li}$  were applied to cycle  $\text{Li}^0\text{Cu}$  cells. The blue and red background colours represent preferred and less desirable values for CE and Li nucleation overpotential values. (b) The voltage profiles of three identical  $\text{Li}^0\text{Cu}$  cells, Cell 1-3, with RE. (c) The voltage profiles of three identical  $\text{Li}^0\text{Cu}$  cells, Cell 1-3, with LiF SE. The first cycle CE from the activation cycle, measured CE, and nucleation overpotentials are shown in the inset of (b) and (c). Note that Cell 1-3 represent: Cell 1, which shows the highest CE of the five assessed cells, Cell 2, which shows the lowest CE, and Cell 3, which represents a CE that approximates the mean value from five cells, were used in the calculation. This selective averaging method ensures that the reported CEs reflect both the range and the typical performance of the half cells with RE and LiF SE, in which LiF SE demonstrates improved and more consistent CE results compared to RE.

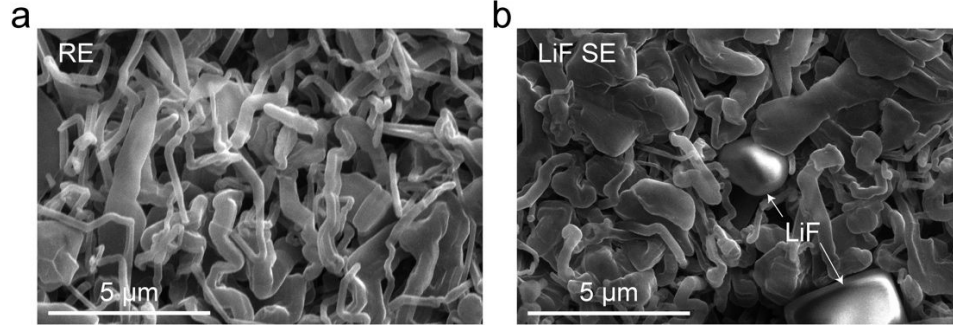


**Figure S12.** SEM images of electrodeposited  $\text{Li}^0$  with RE and LiF SE. (a,b) SEM images of  $\text{Li}^0$  electrodeposits on Cu from  $\text{Li}^0|\text{Cu}$  cells with RE (a) and LiF SE (b). Plating current density of  $1 \text{ mA cm}^{-2}$  and capacity of  $1 \text{ mAh cm}^{-2}$  were used to electrodeposit  $\text{Li}^0$  on Cu from  $\text{Li}^0|\text{Cu}$  cells.

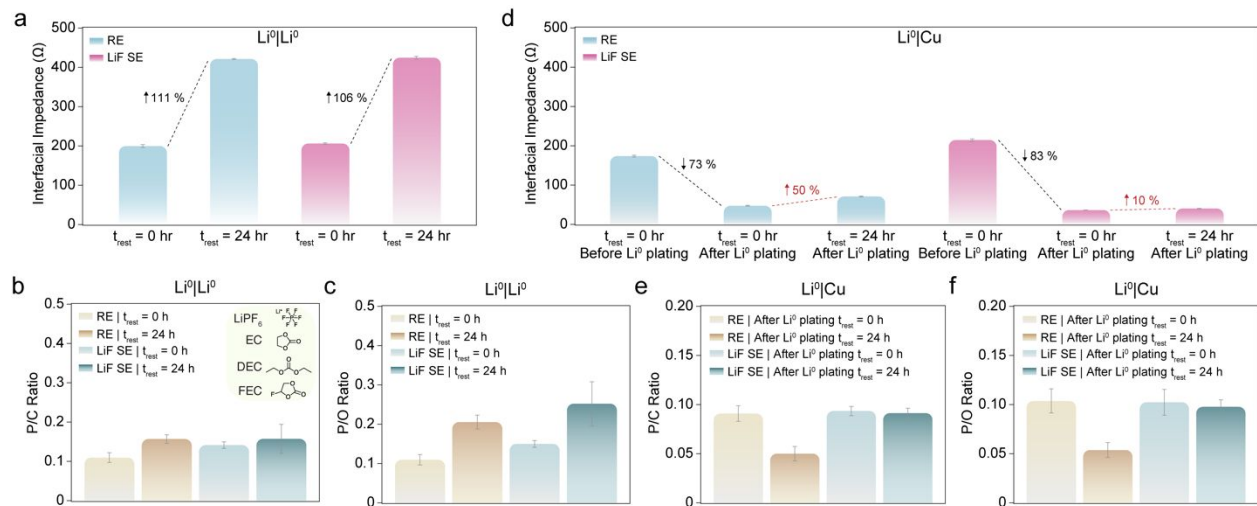


**Figure S13.** Interfacial impedance and interphase analysis on  $\text{Li}^0$  electrode. (a) Time-dependent interfacial impedance measurements from  $\text{Li}^0|\text{Li}^0$  cells with RE and LiF SE. The interfacial impedance was measured right after the cell assembly ( $t_{\text{rest}} = 0 \text{ hr}$ ) and after ageing the cells in an open circuit for a day ( $t_{\text{rest}} = 24 \text{ hr}$ ). Three identical cells were used for each measurement (RE:  $199.64 \Omega \pm 3.73 \Omega$  at  $t_{\text{rest}} = 0 \text{ hr}$  and  $421.24 \Omega \pm 1.33 \Omega$  at  $t_{\text{rest}} = 24 \text{ hr}$  & LiF SE:  $206.03 \Omega \pm 2.20 \Omega$  at  $t_{\text{rest}} = 0 \text{ hr}$  and  $424.47 \Omega \pm 3.64 \Omega$  at  $t_{\text{rest}} = 24 \text{ hr}$ ). The percent increase is indicated by the arrows with dotted lines. (b,c) XPS elemental ratios of P/C (b) and P/O (c) before ( $t_{\text{rest}} = 0 \text{ hr}$ ) and after ageing ( $t_{\text{rest}} = 24 \text{ hr}$ ) the  $\text{Li}^0|\text{Li}^0$  cells with RE and LiF SE. The inset in (b) illustrates the molecular structures of electrolyte species. (d) Interfacial impedance evolution of  $\text{Li}^0|\text{Cu}$  cells with RE and SE. The interfacial impedance was measured right after the  $\text{Li}^0|\text{Cu}$  cell assembly ( $t_{\text{rest}} = 0 \text{ hr}$  Before  $\text{Li}^0$  plating), after depositing  $1 \text{ mAh cm}^{-2}$   $\text{Li}^0$  on Cu at  $1 \text{ mA cm}^{-2}$  ( $t_{\text{rest}} = 0 \text{ hr}$  After  $\text{Li}^0$  plating), and after ageing the  $\text{Li}^0$  deposited  $\text{Li}^0|\text{Cu}$  cell in an open circuit for a day ( $t_{\text{rest}} = 24 \text{ hr}$  After  $\text{Li}^0$  plating). Three identical cells were used for each measurement (RE:  $173.74 \Omega \pm 2.37 \Omega$  at  $t_{\text{rest}} = 0 \text{ hr}$  Before  $\text{Li}^0$  plating,  $47.48 \Omega \pm 1.20 \Omega$  at  $t_{\text{rest}} = 0 \text{ hr}$  After  $\text{Li}^0$  plating, and  $71.07 \Omega \pm 1.08 \Omega$  at  $t_{\text{rest}} = 24 \text{ hr}$  After  $\text{Li}^0$  plating & LiF SE:  $214.54 \Omega \pm 3.18 \Omega$  at  $t_{\text{rest}} = 0 \text{ hr}$  Before  $\text{Li}^0$  plating,  $36.53 \Omega \pm 0.31 \Omega$  at  $t_{\text{rest}} = 0 \text{ hr}$  After  $\text{Li}^0$  plating, and  $40.34 \Omega \pm 0.71 \Omega$  at  $t_{\text{rest}} = 24 \text{ hr}$  After  $\text{Li}^0$  plating). The percent increase and decrease are indicated by the arrows with dotted lines. (e,f) XPS elemental ratios of P/C (e) and P/O (f) before ( $t_{\text{rest}} = 0 \text{ hr}$ ) and after ageing ( $t_{\text{rest}} = 24 \text{ hr}$ ) the electrodeposited  $\text{Li}^0$  from the  $\text{Li}^0|\text{Cu}$  cells with RE and LiF SE.

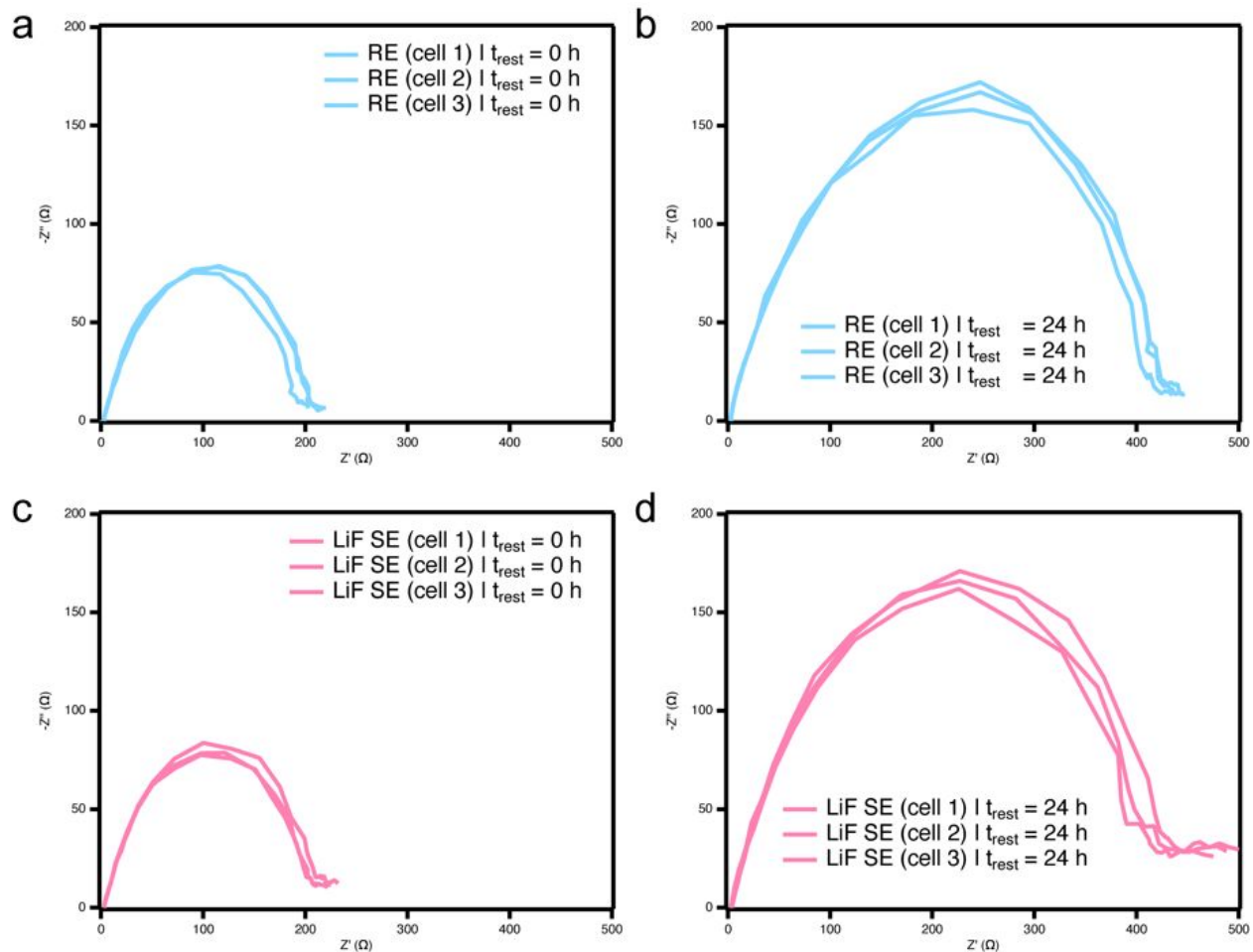


**Figure S14.** Nyquist plots of before and after ageing  $\text{Li}^0|\text{Li}^0$  cell 1~3 with RE and LiF SE. (a) Nyquist plots for measuring the interfacial impedance of  $\text{Li}^0|\text{Li}^0$  cell 1~3 with RE at  $t_{\text{rest}} = 0$  h (190.7  $\Omega$ , 202.6  $\Omega$ , and 205.7  $\Omega$ ). (b) Nyquist plots for measuring the interfacial impedance of  $\text{Li}^0|\text{Li}^0$  cell 1~3 with RE at  $t_{\text{rest}} = 24$  h (424.0  $\Omega$ , 421.4  $\Omega$ , and 418.3  $\Omega$ ). (c) Nyquist plots for measuring the interfacial impedance of  $\text{Li}^0|\text{Li}^0$  cell 1~3 with LiF SE at  $t_{\text{rest}} = 0$  h (203.2  $\Omega$ , 203.4  $\Omega$ , and 211.4  $\Omega$ ). (d) Nyquist plots for measuring the interfacial impedance of  $\text{Li}^0|\text{Li}^0$  cell 1~3 with LiF SE at  $t_{\text{rest}} = 24$  h (433.4  $\Omega$ , 419.6  $\Omega$ , and 420.5  $\Omega$ ).

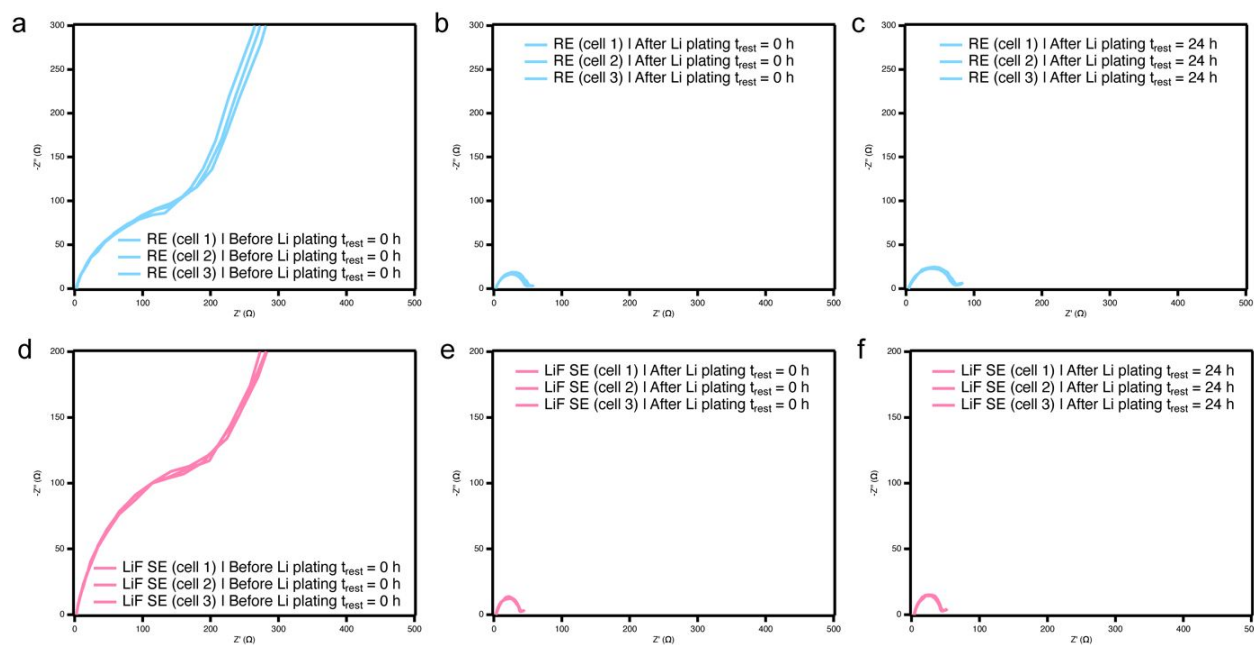


**Figure S15.** Nyquist plots  $\text{Li}^0|\text{Cu}$  cell 1~3 with RE and LiF SE. (a) Nyquist plots for measuring the interfacial impedance of  $\text{Li}^0|\text{Cu}$  cell 1~3 with RE at  $t_{\text{rest}} = 0$  h (177.7  $\Omega$ , 175.4  $\Omega$ , and 168.1  $\Omega$ ). (b) Nyquist plots for measuring the interfacial impedance of  $\text{Li}^0|\text{Cu}$  cell 1~3 after  $\text{Li}^0$  plating with RE at  $t_{\text{rest}} = 0$  h (46.9  $\Omega$ , 50.3  $\Omega$ , and 45.3  $\Omega$ ). (c) Nyquist plots for measuring the interfacial impedance of  $\text{Li}^0|\text{Cu}$  cell 1~3 after  $\text{Li}^0$  plating with RE at  $t_{\text{rest}} = 24$  h (70.9  $\Omega$ , 73.4  $\Omega$ , and 68.8  $\Omega$ ). (d) Nyquist plots for measuring the interfacial impedance of  $\text{Li}^0|\text{Cu}$  cell 1~3 with LiF SE at  $t_{\text{rest}} = 0$  h (207.9  $\Omega$ , 214.2  $\Omega$ , and 221.4  $\Omega$ ). (e) Nyquist plots for measuring the interfacial impedance of  $\text{Li}^0|\text{Cu}$  cell 1~3 after  $\text{Li}^0$  plating with LiF SE at  $t_{\text{rest}} = 0$  h (37.0  $\Omega$ , 35.8  $\Omega$ , and 36.8  $\Omega$ ). (f) Nyquist plots for measuring the interfacial impedance of  $\text{Li}^0|\text{Cu}$  cell 1~3 after  $\text{Li}^0$  plating with LiF SE at  $t_{\text{rest}} = 24$  h (42.0  $\Omega$ , 39.8  $\Omega$ , and 39.2  $\Omega$ ).

## SUPPORTING TABLES

Li <sup>0</sup>  Li <sup>0</sup> (t <sub>rest</sub> = 0 h)	C	O	P	P/C	P/O
RE (cell 1)	25.30	24.70	2.30	0.09	0.09
RE (cell 2)	24.00	23.60	3.20	0.13	0.14
RE (cell 3)	24.80	26.00	2.60	0.10	0.10
Mean	24.70	24.77	2.70	0.11	0.11
Std	0.66	1.20	0.46	0.02	0.02
Error	0.38	0.69	0.26	0.01	0.01

**Table S1.** XPS elemental ratios obtained from Li<sup>0</sup> electrode of Li<sup>0</sup>|Li<sup>0</sup> cell 1~3 with RE at t<sub>rest</sub> = 0 h.

Li <sup>0</sup>  Li <sup>0</sup> (t <sub>rest</sub> = 0 h)	C	O	P	P/C	P/O
LiF SE (cell 1)	25.20	21.10	3.30	0.13	0.16
LiF SE (cell 2)	23.50	24.10	3.20	0.14	0.13
LiF SE (cell 3)	23.50	23.00	3.70	0.16	0.16
Mean	24.07	22.73	3.40	0.14	0.15
Std	0.98	1.52	0.26	0.01	0.02
Error	0.57	0.88	0.15	0.01	0.01

**Table S2.** XPS elemental ratios obtained from Li<sup>0</sup> electrode of Li<sup>0</sup>|Li<sup>0</sup> cell 1~3 with LiF SE at t<sub>rest</sub> = 0 h.

Li <sup>0</sup>  Li <sup>0</sup> (t <sub>rest</sub> = 24 h)	C	O	P	P/C	P/O
RE (cell 1)	29.40	22.00	4.20	0.14	0.19
RE (cell 2)	28.00	20.80	5.00	0.18	0.24
RE (cell 3)	28.10	22.70	4.20	0.15	0.19
Mean	28.50	21.83	4.47	0.16	0.21
Std	0.78	0.96	0.46	0.02	0.03
Error	0.45	0.55	0.27	0.01	0.02

**Table S3.** XPS elemental ratios obtained from Li<sup>0</sup> electrode of Li<sup>0</sup>|Li<sup>0</sup> cell 1~3 with RE at t<sub>rest</sub> = 24 h.

Li <sup>0</sup>  Li <sup>0</sup> (t <sub>rest</sub> = 24 h)	C	O	P	P/C	P/O
LiF SE (cell 1)	28.10	20.80	4.30	0.15	0.21
LiF SE (cell 2)	36.60	18.80	3.50	0.10	0.19
LiF SE (cell 3)	26.90	16.50	6.00	0.22	0.36
Mean	30.53	18.70	4.60	0.16	0.25
Std	5.29	2.15	1.28	0.06	0.10
Error	3.05	1.24	0.74	0.04	0.06

**Table S4.** XPS elemental ratios obtained from Li<sup>0</sup> electrode of Li<sup>0</sup>|Li<sup>0</sup> cell 1~3 with LiF SE at t<sub>rest</sub> = 24 h.

Li <sup>0</sup>  Cu (After Li <sup>0</sup> plating t <sub>rest</sub> = 0 h)	C	O	P	P/C	P/O
RE (cell 1)	37.90	30.10	3.80	0.10	0.13
RE (cell 2)	37.00	35.70	3.60	0.10	0.10
RE (cell 3)	38.70	34.50	2.90	0.07	0.08
Mean	37.87	33.43	3.43	0.09	0.10
Std	0.85	2.95	0.47	0.01	0.02
Error	0.49	1.70	0.27	0.01	0.01

**Table S5.** XPS elemental ratios obtained from plated Li<sup>0</sup> on Cu of Li<sup>0</sup>|Cu cell 1~3 with RE at t<sub>rest</sub> = 0 h. The applied current density and plating capacity were 1 mA cm<sup>-2</sup> and 1 mAh cm<sup>-2</sup>.

Li <sup>0</sup>  Cu (After Li <sup>0</sup> plating t <sub>rest</sub> = 0 h)	C	O	P	P/C	P/O
LiF SE (cell 1)	31.30	39.40	3.20	0.10	0.08
LiF SE (cell 2)	38.30	33.20	3.30	0.09	0.10
LiF SE (cell 3)	39.10	28.50	3.60	0.09	0.13
Mean	36.23	33.70	3.37	0.09	0.10
Std	4.29	5.47	0.21	0.01	0.02
Error	2.48	3.16	0.12	0.00	0.01

**Table S6.** XPS elemental ratios obtained from plated Li<sup>0</sup> on Cu of Li<sup>0</sup>|Cu cell 1~3 with LiF SE at t<sub>rest</sub> = 0 h. The applied current density and plating capacity were 1 mA cm<sup>-2</sup> and 1 mAh cm<sup>-2</sup>.

Li <sup>0</sup>  Cu (After Li <sup>0</sup> plating t <sub>rest</sub> = 24 h)	C	O	P	P/C	P/O
RCE (cell 1)	42.60	40.90	2.40	0.06	0.06
RCE (cell 2)	44.50	40.80	2.60	0.06	0.06
RCE (cell 3)	45.20	41.20	1.60	0.04	0.04
Mean	44.10	40.97	2.20	0.05	0.05
Std	1.35	0.21	0.53	0.01	0.01
Error	0.78	0.12	0.31	0.01	0.01

**Table S7.** XPS elemental ratios obtained from plated Li<sup>0</sup> on Cu of Li<sup>0</sup>|Cu cell 1~3 with RCE at t<sub>rest</sub> = 24 h. The applied current density and plating capacity were 1 mA cm<sup>-2</sup> and 1 mAh cm<sup>-2</sup>.

Li <sup>0</sup>  Cu (After Li <sup>0</sup> plating t <sub>rest</sub> = 24 h)	C	O	P	P/C	P/O
LiF SCE (cell 1)	33.60	30.40	3.40	0.10	0.11
LiF SCE (cell 2)	36.70	35.10	3.10	0.08	0.09
LiF SCE (cell 3)	38.50	36.60	3.40	0.09	0.09
Mean	36.27	34.03	3.30	0.09	0.10
Std	2.48	3.23	0.17	0.01	0.01
Error	1.43	1.87	0.10	0.01	0.01

**Table S8.** XPS elemental ratios obtained from plated Li<sup>0</sup> on Cu of Li<sup>0</sup>|Cu cell 1~3 with LiF SCE at t<sub>rest</sub> = 24 h. The applied current density and plating capacity were 1 mA cm<sup>-2</sup> and 1 mAh cm<sup>-2</sup>.

## SUPPLEMENTARY REFERENCES

- (1) Enkovaara, J.; Rostgaard, C.; Mortensen, J. J.; Chen, J.; Dulak, M.; Ferrighi, L.; Gavnholt, J.; Glinsvad, C.; Haikola, V.; Hansen, H. A.; Kristoffersen, H. H.; Kuisma, M.; Larsen, A. H.; Lehtovaara, L.; Ljungberg, M.; Lopez-Acevedo, O.; Moses, P. G.; Ojanen, J.; Olsen, T.; Petzold, V.; Romero, N. A.; Stausholm-Møller, J.; Strange, M.; Tritsarlis, G. A.; Vanin, M.; Walter, M.; Hammer, B.; Häkkinen, H.; Madsen, G. K. H.; Nieminen, R. M.; Nørskov, J. K.; Puska, M.; Rantala, T. T.; Schiøtz, J.; Thygesen, K. S.; Jacobsen, K. W. Electronic Structure Calculations with GPAW: A Real-Space Implementation of the Projector Augmented-Wave Method. *J. Phys.: Condens. Matter* **2010**, *22*, 253202.
- (2) Hjorth Larsen, A.; Jørgen Mortensen, J.; Blomqvist, J.; Castelli, I. E.; Christensen, R.; Dulak, M.; Friis, J.; Groves, M. N.; Hammer, B.; Hargus, C.; Hermes, E. D.; Jennings, P. C.; Bjerre Jensen, P.; Kermode, J.; Kitchin, J. R.; Leonhard Kolsbjerg, E.; Kubal, J.; Kaasbjerg, K.; Lysgaard, S.; Bergmann Maronsson, J.; Maxson, T.; Olsen, T.; Pastewka, L.; Peterson, A.; Rostgaard, C.; Schiøtz, J.; Schütt, O.; Strange, M.; Thygesen, K. S.; Vegge, T.; Vilhelmsen, L.; Walter, M.; Zeng, Z.; Jacobsen, K. W. The Atomic Simulation Environment - A Python Library for Working with Atoms. *J. Phys.: Condens. Matter* **2017**, *29*, 273002.
- (3) Perdew, J. P.; Burke, K.; Ernzerhof, M. Generalized Gradient Approximation Made Simple. *Phys Rev Lett.* **1996**, *77*, 3865–3868.
- (4) Blochl, P. E. Projector Augmented Wave Method. *Phys Rev B.* **1994**, *50*, 17953.
- (5) Mortensen, J. J.; Hansen, L. B.; Jacobsen, K. W. Real-Space Grid Implementation of the Projector Augmented Wave Method. *Phys Rev B Condens Matter Mater Phys.* **2005**, *71*, 035109.
- (6) Bengtsson, L. Dipole Correction for Surface Supercell Calculations. *Phys Rev B.* **1999**, *59*, 12301.
- (7) Henkelman, G.; Jón, H. Improved Tangent Estimate in the Nudged Elastic Band Method for Finding Minimum Energy Paths and Saddle Points. *J Chem Phys.* **2000**, *113*, 9978–9985.
- (8) Henkelman, G.; Uberuaga, B. P.; Jón, H. A Climbing Image Nudged Elastic Band Method for Finding Saddle Points and Minimum Energy Paths. *J Chem Phys.* **2000**, *113*, 9901–9904.
- (9) Thompson, A. P.; Aktulga, H. M.; Berger, R.; Bolintineanu, D. S.; Brown, W. M.; Crozier, P. S.; in 't Veld, P. J.; Kohlmeyer, A.; Moore, S. G.; Nguyen, T. D.; Shan, R.; Stevens, M. J.; Tranchida, J.; Trott, C.; Plimpton, S. J. LAMMPS - a Flexible Simulation Tool for Particle-Based Materials Modeling at the Atomic, Meso, and Continuum Scales. *Comput Phys Commun.* **2022**, *271*.
- (10) Kaminski, G. A.; Friesner, R. A.; Tirado-Rives, J.; Jorgensen, W. L. Evaluation and Reparametrization of the OPLS-AA Force Field for Proteins via Comparison with Accurate Quantum Chemical Calculations on Peptides. *J. Phys. Chem. B* **2001**, *105*, 6474–6487.
- (11) Kim, M. S.; Zhang, Z.; Rudnicki, P. E.; Yu, Z.; Wang, J.; Wang, H.; Oyakhire, S. T.; Chen, Y.; Kim, S. C.; Zhang, W.; Boyle, D. T.; Kong, X.; Xu, R.; Huang, Z.; Huang, W.; Bent, S. F.; Wang, L. W.; Qin, J.; Bao, Z.; Cui, Y. Suspension Electrolyte with Modified Li<sup>+</sup> Solvation Environment for Lithium Metal Batteries. *Nat Mater.* **2022**, *21*, 445–454.

- (12) Essmann, U.; Perera, L.; Berkowitz, M. L.; Darden, T.; Lee, H.; Pedersen, L. G. A Smooth Particle Mesh Ewald Method. *J Chem Phys.* **1995**, *103*, 8577–8593.
- (13) Martinez, L.; Andrade, R.; Birgin, E. G.; Martínez, J. M. PACKMOL: A Package for Building Initial Configurations for Molecular Dynamics Simulations. *J Comput Chem.* **2009**, *30*, 2157–2164.
- (14) Michaud-Agrawal, N.; Denning, E. J.; Woolf, T. B.; Beckstein, O. MDAAnalysis: A Toolkit for the Analysis of Molecular Dynamics Simulations. *J Comput Chem.* **2011**, *32*, 2319–2327.
- (15) Stukowski, A. Visualization and Analysis of Atomistic Simulation Data with OVITO-the Open Visualization Tool. *Model Simul Mat Sci Eng.* **2010**, *18*, 015012.
- (16) Kim, S. C.; Kong, X.; Vilá, R. A.; Huang, W.; Chen, Y.; Boyle, D. T.; Yu, Z.; Wang, H.; Bao, Z.; Qin, J.; Cui, Y. Potentiometric Measurement to Probe Solvation Energy and Its Correlation to Lithium Battery Cyclability. *J Am Chem Soc.* **2021**, *143*, 10301–10308.
- (17) Adams, B. D.; Zheng, J.; Ren, X.; Xu, W.; Zhang, J. G. Accurate Determination of Coulombic Efficiency for Lithium Metal Anodes and Lithium Metal Batteries. *Adv Energy Mater.* **2018**, *8*, 1702097.
- (18) Kim, M. S.; Zhang, Z.; Wang, J.; Oyakhire, S. T.; Kim, S. C.; Yu, Z.; Chen, Y.; Boyle, D. T.; Ye, Y.; Huang, Z.; Zhang, W.; Xu, R.; Sayavong, P.; Bent, S. F.; Qin, J.; Bao, Z.; Cui, Y. Revealing the Multifunctions of Li<sub>3</sub>N in the Suspension Electrolyte for Lithium Metal Batteries. *ACS Nano.* **2023**, *17*, 3168–3180.
- (19) Kim, M. S.; Lee, S. H.; Kim, M.-S.; Ryu, J.-H.; Lee, K.-R.; Archer, L. A.; Cho, W. II. Enabling Reversible Redox Reactions in Electrochemical Cells Using Protected LiAl Intermetallics as Lithium Metal Anodes. *Sci Adv.* **2019**, *5*, eaax5587.
- (20) Kim, M. S.; Ryu, J. H.; Deepika; Lim, Y. R.; Nah, I. W.; Lee, K. R.; Archer, L. A.; Cho, W. II. Langmuir–Blodgett Artificial Solid-Electrolyte Interphases for Practical Lithium Metal Batteries. *Nat Energy.* **2018**, *3*, 889–898.
- (21) Zhang, Z.; Li, Y.; Xu, R.; Zhou, W.; Li, Y.; Oyakhire, S. T.; Wu, Y.; Xu, J.; Wang, H.; Yu, Z.; Boyle, D. T.; Huang, W.; Ye, Y.; Chen, H.; Wan, J.; Bao, Z.; Chiu, W.; Cui, Y. Capturing the Swelling of Solid-Electrolyte Interphase in Lithium Metal Batteries. *Science.* **2022**, *375*, 66–70.
- (22) Huang, W.; Wang, H.; Boyle, D. T.; Li, Y.; Cui, Y. Resolving Nanoscopic and Mesoscopic Heterogeneity of Fluorinated Species in Battery Solid-Electrolyte Interphases by Cryogenic Electron Microscopy. *ACS Energy Lett.* **2020**, *5*, 1128–1135.
- (23) Zachman, M. J.; Tu, Z.; Choudhury, S.; Archer, L. A.; Kourkoutis, L. F. Cryo-STEM Mapping of Solid–Liquid Interfaces and Dendrites in Lithium-Metal Batteries. *Nature.* **2018**, *560*, 345–349.
- (24) Li, Y.; Li, Y.; Pei, A.; Yan, K.; Sun, Y.; Wu, C. L.; Joubert, L. M.; Chin, R.; Koh, A. L.; Yu, Y.; Perrino, J.; Butz, B.; Chu, S.; Cui, Y. Atomic Structure of Sensitive Battery Materials and Interfaces Revealed by Cryo–Electron Microscopy. *Science.* **2017**, *358*, 506–510.
- (25) Tan, Y. H.; Lu, G. X.; Zheng, J. H.; Zhou, F.; Chen, M.; Ma, T.; Lu, L. L.; Song, Y. H.; Guan, Y.; Wang, J.; Liang, Z.; Xu, W. S.; Zhang, Y.; Tao, X.; Yao, H. Bin. Lithium Fluoride in Electrolyte for Stable and Safe Lithium-Metal Batteries. *Adv. Mater.* **2021**, *33*, 2102134.

- (26) Jurng, S.; Brown, Z. L.; Kim, J.; Lucht, B. L. Effect of Electrolyte on the Nanostructure of the Solid Electrolyte Interphase (SEI) and Performance of Lithium Metal Anodes. *Energy Environ Sci.* **2018**, *11*, 2600–2608.
- (27) Boyle, D. T.; Huang, W.; Wang, H.; Li, Y.; Chen, H.; Yu, Z.; Zhang, W.; Bao, Z.; Cui, Y. Corrosion of Lithium Metal Anodes during Calendar Ageing and Its Microscopic Origins. *Nat Energy.* **2021**, *6*, 487–494.
- (28) Brown, Z. L.; Jurng, S.; Nguyen, C. C.; Lucht, B. L. Effect of Fluoroethylene Carbonate Electrolytes on the Nanostructure of the Solid Electrolyte Interphase and Performance of Lithium Metal Anodes. *ACS Appl Energy Mater.* **2018**, *1*, 3057–3062.
- (29) SutingWeng; Zhang, X.; Yang, G.; Zhang, S.; Ma, B.; Liu, Q.; Liu, Y.; Peng, C.; Chen, H.; Yu, H.; Fan, X.; Cheng, T.; Chen, L.; Li, Y.; Wang, Z.; Wang, X. Temperature-Dependent Interphase Formation and Li<sup>+</sup> Transport in Lithium Metal Batteries. *Nat Commun.* **2023**, *14*, 4474.
- (30) Jagger, B.; Pasta, M. Solid Electrolyte Interphases in Lithium Metal Batteries. *Joule.* **2023**, *7*, 2228–2244.
- (31) Chen, Z.; Wang, B.; Li, Y.; Bai, F.; Zhou, Y.; Li, C.; Li, T. Stable Solvent-Derived Inorganic-Rich Solid Electrolyte Interphase (SEI) for High-Voltage Lithium-Metal Batteries. *ACS Appl Mater Interfaces.* **2022**, *14*, 28014–28020.
- (32) Han, B.; Li, X.; Bai, S.; Zou, Y.; Lu, B.; Zhang, M.; Ma, X.; Chang, Z.; Meng, Y. S.; Gu, M. Conformal Three-Dimensional Interphase of Li Metal Anode Revealed by Low-Dose Cryoelectron Microscopy. *Matter.* **2021**, *4*, 3741–3752.
- (33) Hobold, G. M.; Wang, C.; Steinberg, K.; Li, Y.; Gallant, B. M. High Lithium Oxide Prevalence in the Lithium Solid–Electrolyte Interphase for High Coulombic Efficiency. *Nat Energy.* **2024**, *9*, 580–591.
- (34) Zhang, K.; Wu, F.; Wang, X.; Zheng, L.; Yang, X.; Zhao, H.; Sun, Y.; Zhao, W.; Bai, Y.; Wu, C. An Ion-Dipole-Reinforced Polyether Electrolyte with Ion-Solvation Cages Enabling High–Voltage-Tolerant and Ion-Conductive Solid-State Lithium Metal Batteries. *Adv Funct Mater.* **2022**, *32*, 2107764.
- (35) Sun, C.; Li, R.; Weng, S.; Zhu, C.; Chen, L.; Jiang, S.; Li, L.; Xiao, X.; Liu, C.; Chen, L.; Deng, T.; Wang, X.; Fan, X. Reduction-Tolerance Electrolyte Design for High-Energy Lithium Batteries. *Angew. Chem. Int. Ed.* **2024**, *63*, e202400761.
- (36) Liu, Y.; Tao, X.; Wang, Y.; Jiang, C.; Ma, C.; Sheng, O.; Lu, G.; Wen Lou, X. Self-Assembled Monolayers Direct a LiF-Rich Interphase toward Long-Life Lithium Metal Batteries. *Science.* **2022**, *375*, 739–745.
- (37) Tan, J.; Matz, J.; Dong, P.; Shen, J.; Ye, M. A Growing Appreciation for the Role of LiF in the Solid Electrolyte Interphase. *Adv Energy Mater.* **2021**, *11*, 2100046.
- (38) Wu, H.; Jia, H.; Wang, C.; Zhang, J. G.; Xu, W. Recent Progress in Understanding Solid Electrolyte Interphase on Lithium Metal Anodes. *Adv Energy Mater.* **2021**, *11*, 2003092.
- (39) Xia, Y.; Zhou, P.; Kong, X.; Tian, J.; Zhang, W.; Yan, S.; Hou, W. hui; Zhou, H. Y.; Dong, H.; Chen, X.; Wang, P.; Xu, Z.; Wan, L.; Wang, B.; Liu, K. Designing an Asymmetric Ether-like Lithium Salt to Enable Fast-Cycling High-Energy Lithium Metal Batteries. *Nat Energy.* **2023**, *8*, 934–945.
- (40) Tasaki, K.; Goldberg, A.; Lian, J.-J.; Walker, M.; Timmons, A.; Harris, S. J. Solubility of Lithium Salts Formed on the Lithium-Ion Battery Negative Electrode Surface in Organic Solvents. *J Electrochem Soc.* **2009**, *156*, A1019.

- (41) Tasaki, K.; Harris, S. J. Computational Study on the Solubility of Lithium Salts Formed on Lithium Ion Battery Negative Electrode in Organic Solvents. *J. Phys. Chem. C* **2010**, *114*, 8076–8083.
- (42) Wu, J.; Ihsan-Ul-Haq, M.; Chen, Y.; Kim, J. K. Understanding Solid Electrolyte Interphases: Advanced Characterization Techniques and Theoretical Simulations. *Nano Energy*. **2021**, *89*, 106489.
- (43) Tran, R.; Xu, Z.; Radhakrishnan, B.; Winston, D.; Sun, W.; Persson, K. A.; Ong, S. P. Data Descriptor: Surface Energies of Elemental Crystals. *Sci Data*. **2016**, *3*, 160080.
- (44) Tasker, P. W. The Stability of Ionic Crystal Surfaces. *Phys. C: Solid State Phys.* **1979**, *12*, 4977.
- (45) Rubbo, M.; Bruno, M.; Prencipe, M. Thermodynamic Study of Reconstructed Crystal Surfaces. The Octopolar (111) Face of LiF Crystals. *Surf Sci.* **2015**, *632*, 180–184.
- (46) Kirby, B. J.; Jungwirth, P. Charge Scaling Manifesto: A Way of Reconciling the Inherently Macroscopic and Microscopic Natures of Molecular Simulations. *J Phys Chem Lett.* **2019**, *10*, 7531–7536.
- (47) Zhao, Q.; Stalin, S.; Archer, L. A. Stabilizing Metal Battery Anodes through the Design of Solid Electrolyte Interphases. *Joule*. **2021**, *5*, 1119–1142.
- (48) Lu, Y.; Tu, Z.; Archer, L. A. Stable Lithium Electrodeposition in Liquid and Nanoporous Solid Electrolytes. *Nat Mater.* **2014**, *13*, 961–969.
- (49) Ozhabes, Y.; Gunceler, D.; Arias, T. A. Stability and Surface Diffusion at Lithium-Electrolyte Interphases with Connections to Dendrite Suppression. **2015**, 1–7.
- (50) Cheng, X. B.; Zhao, M. Q.; Chen, C.; Pentecost, A.; Maleski, K.; Mathis, T.; Zhang, X. Q.; Zhang, Q.; Jiang, J.; Gogotsi, Y. Nanodiamonds Suppress the Growth of Lithium Dendrites. *Nat Commun.* **2017**, *8*, 336.
- (51) Zhang, Z.; Cui, Y.; Vila, R.; Li, Y.; Zhang, W.; Zhou, W.; Chiu, W.; Cui, Y. Cryogenic Electron Microscopy for Energy Materials. *Acc Chem Res.* **2021**, *54*, 3505–3517.
- (52) Wan, H.; Xu, J.; Wang, C. Designing Electrolytes and Interphases for High-Energy Lithium Batteries. *Nat Rev Chem.* **2024**, *8*, 30–44.
- (53) Chen, J.; Li, Q.; Pollard, T. P.; Fan, X.; Borodin, O.; Wang, C. Electrolyte Design for Li Metal-Free Li Batteries. *Mater. Today* **2020**, *39*, 118–126.
- (54) Fan, X.; Ji, X.; Han, F.; Yue, J.; Chen, J.; Chen, L.; Deng, T.; Jiang, J.; Wang, C. Fluorinated Solid Electrolyte Interphase Enables Highly Reversible Solid-State Li Metal Battery. *Sci Adv.* **2018**, eaau9245.
- (55) Sayavong, P.; Zhang, W.; Oyakhire, S. T.; Boyle, D. T.; Chen, Y.; Kim, S. C.; Vilá, R. A.; Holmes, S. E.; Kim, M. S.; Bent, S. F.; Bao, Z.; Cui, Y. Dissolution of the Solid Electrolyte Interphase and Its Effects on Lithium Metal Anode Cyclability. *J Am Chem Soc.* **2023**, *145*, 12342–12350.
- (56) Aducci, H.; Chass, G. A.; Passerini, S.; Tian, K. V.; Chen, G. Lithium Batteries and the Solid Electrolyte Interphase (SEI)—Progress and Outlook. *Adv Energy Mater.* **2023**, *13*, 2203307.
- (57) Zhang, E.; Mecklenburg, M.; Yuan, X.; Wang, C.; Liu, B.; Li, Y. Expanding the Cryogenic Electron Microscopy Toolbox to Reveal Diverse Classes of Battery Solid Electrolyte Interphase. *iScience.* **2022**, *25*, 105689.
- (58) Lu, X.; Cheng, Y.; Li, M.; Zou, Y.; Zhen, C.; Wu, D.; Wei, X.; Li, X.; Yang, X.; Gu, M. A Stable Polymer-Based Solid-State Lithium Metal Battery and Its Interfacial

- Characteristics Revealed by Cryogenic Transmission Electron Microscopy. *Adv Funct Mater.* **2023**, *33*.
- (59) Jabbari, V.; Yurkiv, V.; Rasul, M. G.; Phakatkar, A. H.; Mashayek, F.; Shahbazian-Yassar, R. In Situ Formation of Stable Solid Electrolyte Interphase with High Ionic Conductivity for Long Lifespan All-Solid-State Lithium Metal Batteries. *Energy Storage Mater.* **2023**, *57*, 1–13.
- (60) Gao, Y.; Yan, Z.; Gray, J. L.; He, X.; Wang, D.; Chen, T.; Huang, Q.; Li, Y. C.; Wang, H.; Kim, S. H.; Mallouk, T. E.; Wang, D. Polymer–Inorganic Solid–Electrolyte Interphase for Stable Lithium Metal Batteries under Lean Electrolyte Conditions. *Nat Mater.* **2019**, *18*, 384–389.
- (61) Sheng, O.; Zheng, J.; Ju, Z.; Jin, C.; Wang, Y.; Chen, M.; Nai, J.; Liu, T.; Zhang, W.; Liu, Y.; Tao, X. In Situ Construction of a LiF-Enriched Interface for Stable All-Solid-State Batteries and Its Origin Revealed by Cryo-TEM. *Adv. Mater.* **2020**, *32*.
- (62) Xia, Y.; Zhou, P.; Kong, X.; Tian, J.; Zhang, W.; Yan, S.; Hou, W. hui; Zhou, H. Y.; Dong, H.; Chen, X.; Wang, P.; Xu, Z.; Wan, L.; Wang, B.; Liu, K. Designing an Asymmetric Ether-like Lithium Salt to Enable Fast-Cycling High-Energy Lithium Metal Batteries. *Nat Energy.* **2023**, *8*, 934–945.
- (63) Jones, J.; Anouti, M.; Caillon-Caravanier, M.; Willmann, P.; Lemordant, D. Thermodynamic of LiF Dissolution in Alkylcarbonates and Some of Their Mixtures with Water. *Fluid Phase Equilib.* **2009**, *285*, 62–68.
- (64) Amanchukwu, C. V.; Yu, Z.; Kong, X.; Qin, J.; Cui, Y.; Bao, Z. A New Class of Ionically Conducting Fluorinated Ether Electrolytes with High Electrochemical Stability. *J Am Chem Soc.* **2020**, *142*, 7393–7403.
- (65) Duffy, J. J.; Panalytical, M.; Hill, A. J. Suspension Stability; Why Particle Size, Zeta Potential and Rheology Are Important. **2012**, *20*.
- (66) Pate, K.; Safier, P. Chemical Metrology Methods for CMP Quality. In *Advances in Chemical Mechanical Planarization (CMP)*; Elsevier, 2021; pp 355–383.
- (67) Chen, X.; Yao, N.; Zeng, B. S.; Zhang, Q. Ion–Solvent Chemistry in Lithium Battery Electrolytes: From Mono-Solvent to Multi-Solvent Complexes. *Fundam. Res.* **2021**, *1*, 393–398.
- (68) Xiao, J.; Li, Q.; Bi, Y.; Cai, M.; Dunn, B.; Glossmann, T.; Liu, J.; Osaka, T.; Sugiura, R.; Wu, B.; Yang, J.; Zhang, J. G.; Whittingham, M. S. Understanding and Applying Coulombic Efficiency in Lithium Metal Batteries. *Nat Energy.* **2020**, *5*, 561–568.
- (69) Li, Y.; Huang, W.; Li, Y.; Pei, A.; Boyle, D. T.; Cui, Y. Correlating Structure and Function of Battery Interphases at Atomic Resolution Using Cryoelectron Microscopy. *Joule.* **2018**, *2*, 2167–2177.
- (70) Biswal, P.; Stalin, S.; Kludze, A.; Choudhury, S.; Archer, L. A. Nucleation and Early Stage Growth of Li Electrodeposits. *Nano Lett.* **2019**, *19*, 8191–8200.
- (71) Pei, A.; Zheng, G.; Shi, F.; Li, Y.; Cui, Y. Nanoscale Nucleation and Growth of Electrodeposited Lithium Metal. *Nano Lett.* **2017**, *17*, 1132–1139.
- (72) Yan, K.; Lu, Z.; Lee, H. W.; Xiong, F.; Hsu, P. C.; Li, Y.; Zhao, J.; Chu, S.; Cui, Y. Selective Deposition and Stable Encapsulation of Lithium through Heterogeneous Seeded Growth. *Nat Energy.* **2016**, *1*, 16010.
- (73) Yamada, Y.; Wang, J.; Ko, S.; Watanabe, E.; Yamada, A. Advances and Issues in Developing Salt-Concentrated Battery Electrolytes. *Nat Energy.* **2019**, *4*, 269–280.

- (74) Wang, Z.; Qi, F.; Yin, L.; Shi, Y.; Sun, C.; An, B.; Cheng, H. M.; Li, F. An Anion-Tuned Solid Electrolyte Interphase with Fast Ion Transfer Kinetics for Stable Lithium Anodes. *Adv Energy Mater.* **2020**, *10*.
- (75) Li, Y.; Liu, Q.; Wu, S.; Geng, L.; Popovic, J.; Li, Y.; Chen, Z.; Wang, H.; Wang, Y.; Dai, T.; Yang, Y.; Sun, H.; Lu, Y.; Zhang, L.; Tang, Y.; Xiao, R.; Li, H.; Chen, L.; Maier, J.; Huang, J.; Hu, Y. S. Unraveling the Reaction Mystery of Li and Na with Dry Air. *J Am Chem Soc.* **2023**, *145*, 10576–10583.
- (76) Lee, J.; Kim, M. S.; Cui, Y.; Zhang, W.; Shuchi, S. B.; Holmes, S. E.; Lee, J. H.; Serrao, C.; Kim, S. C.; Holoubek, J.; Sayavong, P.; Cai, A.; Choi, I. R.; Cui, Y. Reactive Suspension Electrolytes for Lithium Metal Batteries. *ACS Energy Lett.* **2025**, *10*, 4252–4259.